POLYCRYSTALLINE SILICON THIN FILM PROCESSING ON GLASS SUBSTRATES FOR PHOTOVOLTAIC APPLICATIONS

A THESIS SUBMITTED TO
THE GRADUATE SCHOOL OF NATURAL AND APPLIED SCIENCES
OF
MIDDLE EAST TECHNICAL UNIVERSITY

BY

MEHMET KARAMAN

IN PARTIAL FULFILLMENT OF THE REQUIREMENTS
FOR
THE DEGREE OF DOCTOR OF PHILOSOPHY
IN
MICRO AND NANOTECHNOLOGY

AUGUST 2016

Approval of the Thesis:

POLYCRYSTALLINE SILICON THIN FILM PROCESSING ON GLASS AND PHOTOVOLTAIC APPLICATIONS

submitted by **MEHMET KARAMAN** in partial fulfillment of the requirements for the degree of **Doctor of Philosophy in Micro and Nanotechnology Department, Middle East Technical University** by,

Prof. Dr. Gülbin Dural Ünver
Dean, Graduate School of **Natural and Applied Sciences**

Assoc. Prof. Dr. Burcu Akata Kurç
Head of Department, **Micro and Nanotechnology Dept., METU**

Prof. Dr. Raşit Turan
Supervisor, **Physics Dept., METU**

Assoc. Prof. Dr. Özge Tüzün Özmen
Co-Supervisor, **Physics. Dept., Düzce University**

Examining Committee Members:

Prof. Dr. Mehmet Parlak
Physics Dept., METU

Prof. Dr. Raşit Turan
Physics Dept., METU

Prof. Dr. Ferhunde Atay
Physics Dept., Osmangazi University

Assoc. Prof. Dr. Yunus Eren Kalay
Metallurgical and Materials Engineering Dept., METU

Assoc. Prof. Dr. Kadir Ertürk
Physics Dept., Namık Kemal University

Date: *18.08.2016*

I hereby declare that all information in this document has been obtained and presented in accordance with academic rules and ethical conduct. I also declare that, as required by these rules and conduct, I have fully cited and referenced all material and results that are not original to this work.

Name, Lastname: Mehmet KARAMAN

Signature :

ABSTRACT

POLYSILICON THIN FILM PROCESSING ON GLASS AND PHOTOVOLTAIC APPLICATIONS

Karaman, Mehmet
Ph.D., Micro and Nanotechnology
Supervisor: Prof. Dr. Raşit Turan
Co-Supervisor: Assoc. Dr. Özge Tüzün Özmen

August 2016, 154 pages

In this PhD study, crystallization of amorphous silicon on glass and its photovoltaic applications have been investigated. The crystallization of amorphous silicon (a-Si) was studied in two parts; Metal Induced Crystallization (MIC) and Laser Induced Crystallization (LIC). MIC method was first implemented by gold nanoparticle (AuNP) fabricated by dewetting technique by which gold thin films deposited on aluminium doped zinc oxide (AZO) coated glass were annealed for nanoparticle formation. A-Si was then deposited by e-beam evaporation onto metal nanoparticles. Silicon films were annealed for crystallization at different temperatures between 500 oC and 600 oC. It was observed that inclusion of AuNPs provide the crystallization at lower temperatures with higher rates. Raman and XRD results showed that the crystallization starts at temperatures as low as 500 ^{o}C and an annealing at 600 ^{o}C for a short process time provides sufficiently good crystallinity. Then, MIC process was studied by Aluminium Induced Crystallization (AIC) of a-Si. Firstly, AIC study was

started with the silicon nitride (SiN_x) buffer layer optimization by depositing different types of SiNx films with varied NH3/SiH4 content during the PECVD film deposition. Furthermore, the effect of buffer layer content on final poly-Si properties was investigated by this way. AIC process was started with Al film evaporation onto SiNx and AZO layers. Then a-Si deposition was carried out by e-beam evaporation. The crystallization, in other words the layer exchange of Al and Si, was provided by furnace annealing at 500 ^{o}C. Based on Raman, EBSD, XRD results, the best buffer layer was chosen in terms of Si crystallinity and grain size for the further AIC experiments. The next AIC experiments were followed by basic characterizations. The crystallization of AIC process at different temperatures and durations was monitored by optical microscopy (OM) and the activation energy of the process was calculated. The Al content of the poly-Si layer was detected by Secondary Ion Mass Spectroscopy (SIMS). The effect of AlO_x membrane on the kinetics of crystallization was monitored through optical microscopy by changing the formation conditions of AlO_x. Then solid phase epitaxy (SPE) experiments were carried out. Raman and SEM analysis showed well-established SPE layer. To investigate the improvement of the final AIC poly-Si layer quality, some modifications on the process was introduced. The effect of Al annealing in a vacuum environment on the AIC kinetics and final poly-Si layer properties was investigated. The layer exchange process was monitored by optical microscopy and it was observed that Al annealing reduces the crystallization rate. XPS measurements showed that annealing of Al creates more stable and denser AlOx layer compared to Al layer with no annealing. EBSD results indicate that Al annealing notably increases the grain size of Al layer and also improves the grain structure of final poly-Si layer surface. Another improvement on the AIC poly-Si layer quality is seen by comparing the different a-Si deposition methods of E-beam evaporation and PECVD. Two techniques are compared for their effect on the overall AIC kinetics as well as the properties of the final poly-crystalline (poly-Si) silicon film. Raman and FTIR spectroscopy results indicate that the PECVD grown a-Si films has higher intermediate-range order, which is enhanced for increased hydrogen dilution during deposition. EBSD analysis showed that increasing intermediate-range order of the a-Si suppresses the rate of AIC, leading larger poly-Si grain size.

In the second part of this work, laser assisted crystallization was carried out. Three layered stack of $SiO_xN_y/SiO_x/SiN_x$ was deposited by PECVD onto borosilicate glass as the buffer layer. 10 µm of intrinsic and 10 nm of p and n-type a-Si:H (doping layer) was deposited by PECVD. The crystallization was carried out by 808 nm continuous wave line laser. Moderately doped absorber layer was obtained during laser crystallization by intermixing of doping layer and intrinsic layer. After crystallization the homojunction solar cells were obtained by spin-on dopant coating with following laser doping and the mesa cells were constructed. Two different laser doping velocities of 1 and 5 mm/s were applied. For comparison some of the cells were hydrogen passivated. SunsVoc measurement was accomplished and up to 579 mV of V_{oc} was measured. EQE and solar simulator analysis were carried out both for substrate and superstrate conditions. EQE measurements show that H_2 passivation decreases the emitter diffusion length (short wavelenths) due to the increase in surface recombination whereas the absorber diffusion length increases.

Keywords: Amorphous Silicon, Metal Induced Crystallization, Aluminum Induced Crystallization, Gold Induced Crystallization, Lazer Crystallization, Laser Doping

ÖZ

FOTOVOLTAİK UYGULAMALAR İÇİN CAM ALTTAŞ ÜZERİNE POLİKRİSTAL SİLİSYUM İNCE FİLMLERİN URETİMİ

Karaman, Mehmet
Doktora, Mikro ve Nanoteknoloji
Tez Yöneticisi : Prof. Dr. Raşit Turan
Ortak Tez Yöneticisi: Doç. Dr. Özge Tüzün Özmen

Ağustos 2016, 154 sayfa

Bu tez çalışmasında, amorf silisyumun cam üzerinde kristalizasyonu ve fotovoltaik uygulamaları araştırılmıştır. Amorf silisyum (a-Si) kristalizasyonu iki bölümde incelenmiştir; Metal İndüklemeli Kristalizasyon (MIC) ve Lazer İndüklemeli Kristalizson (LIC). MIC yöntemi ilk olarak alüminyum katkılı çinko oksit (AZO) kaplı cam üzerine üretilen altın ince filmlerin tavlanarak altın nanoparçacık (AuNP) oluşturulmasıyla uygulanmıştır.Sonrasında metal naoparçacıkların üzerine elektron demeti buharlaştırma yöntemi ile a-Si buharlaştırılmıştır. Silisyum ince filmler kristalizasyon için 500 ^{o}C ve 600 ^{o}C arasında tavlanmıştır. Düşük sıcaklıklarda AuNP ile yüksek oranda kristalizasyon sağlanması gözlemlenmiştir. Raman ve XRD sonuçları kristalizasyonun 500 ^{o}C gibi düşük sıcaklıkta başladığını ve 600 ^{o}C de tavlamanın kısa sürede yeterli kristalizasyon sağladığını göstermiştir. Sonra ise, MIC işlemi a-Si'un uAlüminyum İndüklemeli Kristalizasyon (AIC) ile çalışılmıştır. İlk olarak, AIC çalışması PECVD film üretiminde değişken NH_3/SiH_4 oranları kullanılarak farklı türde üretilen SiN_x ara tabaka optimizasyonu ile başlamıştır. Üstelik bu şekilde farklı ara tabakaların üretilen poly-Si filmlere olan etkisi araştırılmıştır. AIC işlemi SiN_x ve AZO tabakalar üzerine Al buharlaştırılmasıyla başlatılmıştır. Sonra elektron demeti ile a-Si buharlaştırılmıştır. Kristalizasyon, başka deyişle Al ve Si

tabakalarının yer değiştirmesi, 500 ^{o}C de tavlama ile sağlanmışır. Raman, EBSD ve XRD sonuçlarına dayanarak sonraki AIC deneyleri için en iyi ara tabaka Si kristalizasyonu ve damar boyutlarına göre seçilmiştir. Bundan sonraki AIC deneylerine temel karakterizasyonlar ile devam edilmiştir. Farklı sıcaklık ve sürelerdeki AIC krsitalizasyonu optik mikroskop (OM) ile gözlemlenmiş ve kristalizasyonun aktivasyon enerjisi hesaplanmıştır. Poly-Si tabakanın Al içeriği İkincil İyon Kütlesi Spectroskopisi (SIMS) ile tespit edilmiştir. AlO_x zar tabakanın kristalizasyon kinetiğine olan etkisi zar tabakanın üretim koşullarını değiştirerek optik mikroskop ile gözlenmiştir. Sonrasında ise Katı Faz Epitaksi (SPE) deneyleri yapılmıştır. Raman ve SEM analizleri SPE tabakaların bir şekilde elde edildiğini göstermiştir. AIC poly-Si tabakanın kalitesini arttırmak için üretime bir takım modifikasyonlar eklenmiştir. Vakum içerinde Al tavlamanın, AIC kinetiğine ve poly-Si tabaka özelliklerine etkisi araştırılmıştır. Tabakaların yer değiştirmesi optik mikroskop ile izlenmiş ve Al tavlamanın kristalizasyon hızını düşürdüğü gözlenmiştir. XPS ölçümleri, Al tabakanın tavlanmasının daha sabit ve yoğun yapılı AlO_x zar oluşturduğunu göstermiştir. Bir diğer AIC poly-Si tabaka kalitesinin iyileştirilmesi ise elektron demeti buharlaştırma ve PECVD gibi farklı a-Si üretim metotlarının karşılaştırılmasıyla gözlemlenmiştir. İki tekniğin etkisi, AIC kinetiğinin yanı sıra üretilen poly-Si film özelliklerine göre karşılaştırılmıştır. Raman ve FTIR spektroskopisi sonuçları PECVD ile üretilen a-Si filmlerde orta mesafe düzeninin üretim süresince yüksek hidrojen seyreltmesiyle daha çok arttığını göstermiştir. EBSD analizleri, a-Si orta mesafe düzeninin arttırılmasının AIC hızını bastırdığı, dolayısıyla daha büyük poly-Si damar boyutları oluşturduğunu göstermiştir.

Bu çalışmanın ikinci bölümünde lazer destekli kristalizasyon uygulanmıştır. Borosilikat cam üzerine PECVD ile üç katmanlı $SiO_xN_y/SiO_x/SiN_x$ ara tabakası üretilmiştir.10 µm katkısız ve 10 nm p ve n-tipi a-Si:H (katkılama tabakası) PECVD ile üretilmiştir. Kristalizasyon 808 nm sabit dalga çizgi lazer ile yapılmıştır. Lazer kristalizasyonu boyunca katkısız ve katkılama tabakalarının birbirine karışmasıyla az katkılı emici tabaka elde edilmiştir. Kristalizasyon sonrasında spin kaplama yapılmış ve lazer ile katkılama yapılarak homo eklem mesa güneş hücreleri oluşturulmuştur. 1 ve 5 mm/s olmak üzere iki farklı lazer katkılama hızları uygulanmıştır. Karşılaştırma yapılabilmesi açısından bazı hücrelere hidrojen pasivasyonu uygulanmıştır. Suns V_{oc}

analizleri yapılmış ve 579 mV V_{oc} ölçülmüştür. EQE ve güneş simülatörü ölçümleri hem alttaş hem de üsttaş koşullarında yapılmıştır. EQE ölçümleri hidrojen pasivasyonunun yüzey rekombinasyonunu arttırdığı için yayıcı difüzyonu mesafesini (düşük dalga boyları) azalttığını göstermiştir buna karşılık emici difüzyonu mesafesi artmıştır.

Anahtar kelimeler: Amorf Silisyum, Metal İndüklemeli Kristalizasyon, Alüminyum İndüklemeli Kristalizasyon, Altın İndüklemeli Kristalizasyon, Lazer Kristalizasyon, Lazer Katkılama

To those who believe

the world will be a better place

ACKNOWLEDGEMENTS

First of all, I would like to express my sincerest gratitude to my supervisor Prof. Dr. Raşit Turan for providing me with great encouragement, inspiration, and support since I came to Ankara. I consider myself to be highly privileged to be one of his PhD graduate candidates and to be given the opportunity to be a member of GÜNAM family. His gentle and precise guidance all along has helped me and enabled me to study effectively. I attribute the level of my PhD degree to his encouragement and effort and without him this thesis would not have been completed or written. One simply could not wish for a greater supervisor.

It is a pleasure to offer my sincere thanks to all the other people who have contributed to my long journey.

My warm thanks also belong to Dr. Aydın Tankut for his encouragement and tolerance throughout my research. He has been a great mentor and a guide. He is not only a colleague but also a modest friend with whom I can speak about anything. I especially would like to thank him for the enlightening conversations we had on music which helped increase my motivation to work on my thesis.

I am highly grateful to Assoc. Prof. Dr. Özge Tüzün Özmen for having given me the opportunity to have her as my co-advisor during my research. I have learnt so many things from her. She generously offered her professional support and sincerity and warmth as a friend since we met. I am also grateful to her for including me in her Tübitak 1001 project having a project number of 112T084.

I wish to express my thanks to Prof. Dr. Mehmet Parlak and Assoc. Prof. Dr. Y. Eren Kalay for participating in my thesis committee. I was given the opportunity to consult them and benefit from their insightful comments. I also thank Prof. Dr. Ferhunde Atay for kindly participating in my thesis defence evaluation.

I am also deeply grateful to Assoc. Prof. Dr. Alpan Bek for enabling me to participate in his Tübitak 1003 project having a project number of 115M061.

I would like to thank Assoc. Prof. Dr. Kadir Ertürk for evaluating my thesis. He has motivated me highly since the beginning of my PhD study and guided me in my e-beam processing study. Furthermore, not only as a colleague but also as a kind friend, I had great time with him during his study at METU.

I sincerely appreciate the help of Assoc. Prof. Dr. Mustafa Kulakçı during my study at METU. He has kindly guided me with his patience and immense knowledge.

My sincere thanks also goes to Assist. Prof. Dr. Selçuk Yerci for being helpful and sharing his knowledge.

I would like to thank the staff of Atılım University physics group; Prof. Dr. Ramazan Aydın, Prof. Dr. Hüseyin Oymak, Assoc. Prof. Dr. Yasemin Saraç Oymak, Assist Prof. Dr. Filiz Korkmaz, Assist Prof. Dr. Mehmet Işık, Halil İbrahim Aydemir for the stimulating discussions and for all the fun we had for 2.5 years.

Besides, I am thankful to METU Central Labs management; Prof. Dr. Macit Özenbaş, Assoc. Prof. Dr. Burcu Akata Kurç. I would also like to thank Sedat Canlı, İlker Yıldız, Merve Kaplan and Dr. Özlen Ferruh Erdem for the analysis of the samples.

I am profoundly grateful to PVcomB and EEIS staff from Hellholtz Zentrum (HZB) Berlin. Dr. Stefan Gall provided me with comprehensive guidance during my research at HZB and I am deeply thankful to him. Furthermore, it is impossible to forget how supportive and friendly my colleagues Tim Frijnts and Sven Kühnapfel were. I am also truly grateful for their patience.

I would like to express my sincere thanks to my colleagues in GÜNAM: Olgu Demircioğlu and Zeynep Demircioğlu, for their kind friendships and assistance since the beginning of my life in Ankara; Especially, Zeynep Demircioğlu, for her patience during the formatting of my Msc. and Phd. Theses; Seda Kayra Güllü and Hasan Hüseyin Güllü, for their kind friendship; Salar Habibpur Sedani, for having joyful times together and also for his support in my study; Dr. Engin Özkol, for his sincere friendship and sharing his office with me. Moreover, I would like to thank him for his help during PECVD processes; Hisham Nasser, for being a wonderful friend and helping me with my study. Besides, I am grateful for his ellipsometry measurements.

I would like to thank Fırat Es, who is my earliest colleague in GÜNAM, for supporting my studies; Mustafa Ünal for sharing his knowledge in AFM measurements, Yasin Ergunt for his kindness and friendly discussions, Tahir Çolakoğlu for sharing his knowledge, Kurtuluş Abak, Bilgecan Yıldız Karakul, Nazan Kara, Emine Hande Çiftpınar, Yusuf Kasap, Gülsen Baytemir, Dr. Serim İlday, Serra Altınoluk, Ergi Dönerçark, Mete Günöven, Özden Başar Balbaşı, Merve Pınar Kabukcuoğlu, Idris Candan, Dr. Mücahit Yılmaz, Makbule Terlemezoğlu, Emel Semiz, Gamze Kökbudak, İsmail Kabaçelik, Arezoo Hosseini, and Pantea Auarang, for being my friends.

I am grateful to GÜNAM technicians; Yücel Eke, Nevzat Görmez, Tayfun Yıldız, Dursun Erdoğan for technical support and also to Harun Tanık, Tuncay Güngör and Buket Gökbakan for their support in administrative issues in GÜNAM.

As an amateur musician, I am extremely grateful to my friends with whom I play together: Esatcan Apak, Cem Lider, Onur Yürüten, Mehmet Kutluay, Emre Genç, Altuğ Öztürk, Ekin Özgönül, Oğuz Kerem Şengöz. Together we have formed the most rocking local “Progressive Rock” bands which have provided strong motivation for me to work harder.

I am deeply grateful to the sailors and fishermen in Palamutbükü, which is my hometown, and Knidos. They have always motivated me with their passion for life. I am especially grateful to Tahsin Uzun with whom I had long phone conversations when I felt stressed.

I am endlessly grateful to my love, Selin for her continuous support. During my Phd study, she has done her best to motivate me. She stood beside me even when I had to work for long hours and could not spend time with her. I would like to say that I am the luckiest man to be married to Selin.

Last but not the least, I am deeply grateful to my lovely family, my mother and my father in particular, for their understanding, endless support and encouragement during my continuous learning process. I could not have completed this thesis without their existence.

TABLE OF CONTENTS

CHAPTERS

LIST OF TABLES

TABLES

LIST OF FIGURES

FIGURES

NOMENCLATURE

a-Si	Amorphous silicon
a-Si:H	Hydrogenated amorphous silicon
Al:ZnO	Aluminum Doped Zinc Oxide
AuNPs	Gold nanoparticles
c-Si	Crystalline silicon
MIC	Metal Induced Crystallization
AIC	Aluminum Induced Crystallization
LIC	Laser Induced Crystallization
PECVD	Plasma Enhanced Chemical Vapor Deposition
J_{sc}	Short circuit current density
V_{oc}	Open circuit voltage
EBSD	Electron Back Scattering Dffraction
AFM	Atomic Force Microscopy
SEM	Scanning Electron Microscope
TEM	Transmission Electron Microscopy
SiN_x	Silicon Nitride

CHAPTER 1

INTRODUCTION

1.1 Introduction

The rising population of the world increases the carbondioxide amount in the atmosphere. The fossil fuels result in greenhouse gases which affects the biologic life resources like clean water, food. Especially the petrol addictive life style destroys the environment gradually and the creature life is under threat. In addition, the rising population increases the energy demand as the energy resources are running out with an uncontrolled way. The new clean resources are needed for a sustainable healthy life on the earth. According to the scenario of International Energy Agency (IEA) the energy consumption will grow by one third in 2040 [1]. In this perspective, the energy production road map must shift to renewable energy rather than fossil fuels. Among the renewable energy sources like solar power, wind power, wave power, biomass, hydro power, and geothermal, solar energy is the most applicable one on the earth due to the abundance of the source which is the sun. As a result of this, conversion of light into electricity (photoconversion) can be used in many fields like buildings, vehicles, clothes, vegetation and especially in isolated places. Another advantages of using solar energy is that it is environment-friendly and silicon based ones contain non-toxic material. The solar panel prices are far from being expensive like the prices in 90s. In Figure 1, the global cumulative installed PV capacity is given with respect to the region contributions.

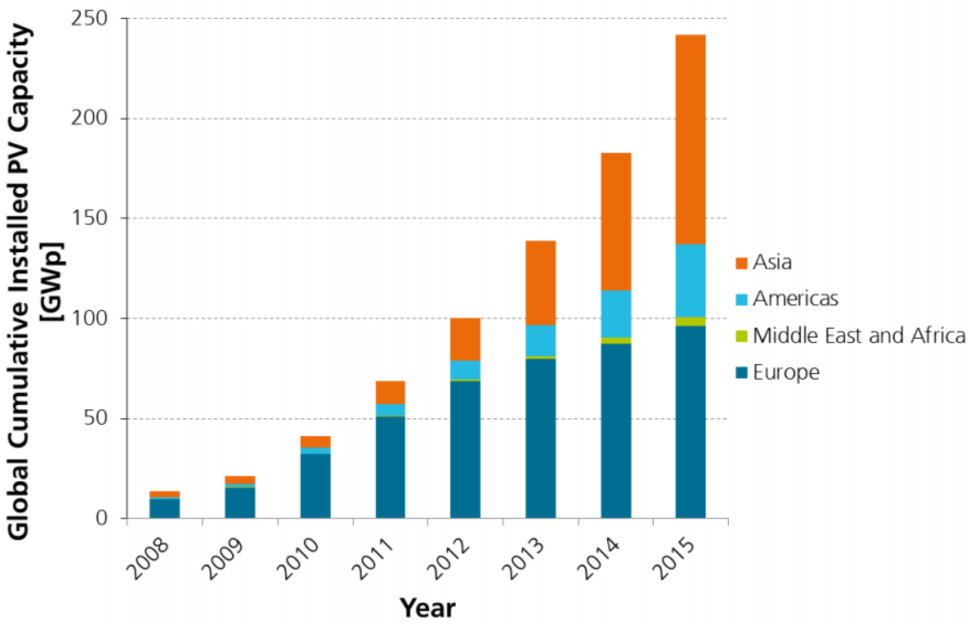

Figure 1: Global Solar panel installation of regions until 2015 [2]

As stated in Figure 1, a notable rise in solar panel installation begins at the end of 2000s. Europe seems to be the leader in PV installation. However in 2015, Asia catches up with Europe in total PV installations worldwide. Furthermore, America also gives significant contribution to the total amount. This picture also indicates that there is a great interest in solar electricity in terms of clean energy production and the price drop of wafer based technologies correspondingly affects the other silicon based PV technologies. Historically, the story of photovoltaic conversion started with the discovery photovoltaic effect and the operation of solar cell by French physicist Edmond Becquerel in 1839 [3]. Then in 1888, Russian physicist Aleksandr Stoletov constructed the first cell based on the outer photoelectric effect discovered by Heinrich Hertz [4]. In 1905 Albert Einstein introduced a new quantum theory on light by which he explained the photoelectric effect and win a nobel prize in 1921 [5]. The first silicon photosensitive device was patented by Russel Ohl in 1941 [6] and the first silicon solar cell with 6 % efficiency was announced by Bell Labs in 1954 [7]. In the second half of the last century there has been significant developments on silicon solar cell technology and today more than 25 % efficiency was achieved by Panasonic company with the monocrystalline silicon based heterojunction technology [8]. Besides, around

21 % efficiency was introduced by Trina Solar for the multicrystalline silicon based technology [9].

There are different types of solar cell technologies, however most of the market is dominated by silicon wafer based technology. In addition, multicrystalline and monocrystalline based solar cells have been studied for many years and technological limits are nearly approached. Besides, the decline of the wafer prices are not enough because wafer based technology has quite production adversity which inhibits further decrease of prices. However, in general there is a much more commercialized rate of PV industry with respect to the beginning of 2000s. Amorphous silicon thin film approach is an alternative way to low-cost technology. However due to limited efficiency values and light induced degradation effects, amorphous silicon studies show a decline in the last 5 years and some of the manufacturers left the amorphous silicon thin film market [10,11]. In this sense photovoltaic industry aims to head towards new technologies. Thin film crystalline approach is a promising alternative to bulk silicon due to its lower material consumption, i.e. low-cost production, with high conversion efficiency. High quality, low cost and large-area applications of poly-Si thin film constitutes an alternative material to crystalline silicon. In this approach the idea is combining the crystalline silicon properties with easy and low-cost production of thin film. In addition, poly-Si thin films are not subject to light-induced degradation effects [10].

In this work we have carried out extensive studies on several aspects of thin film crystalline Si for PV applications. Metal induced crystallization (MIC) and laser induced crystallization (LIC) approaches were studied. MIC technique was realized by Au and Al induced crystallization. Especially, the deep investigations on Aluminium induced crystallization (AIC) in terms of process kinetics, Al structure, different Si deposition methods are the core of the thesis. The solar cells were constructed by the laser assisted process. LIC was used for thin film crystalline fabrication and junction formation was accomplished by laser doping (LD).

This thesis is organized as 7 chapters. In Chapter 1, we give an overview on solar energy conversion technologies and our motivation behind this work.

In Chapter 2, a short historical background and the importance of polycrystalline silicon in industry is discussed. The structural properties of polycrystalline silicon is given with the thin film polycrystalline silicon (poly-Si). Then the thin film poly-Si fabrication methods with photovoltaic applications are presented with literature survey

In Chapter 3, MIC is handled first with Au induced crystallization. The effect of AuNPs on crystallization of amorphous silicon is given. Then, standard AIC process is carried out from buffer layer optimization to final poly-Si fabrication. AIC kinetics is studied with basic characterization techniques and finally some SPE experiments are given.

In Chapter 4, the AIC process is investigated extensively by annealing the Al layer in vacuum environment. The structural properties of Al is identified and the effects on poly-Si layer is observed.

In Chapter 5, the effects of different Si deposition techniques of e-beam and PECVD on the AIC process is researched and compared in terms of process kinetics and structural differences. Moreover, taking the properties of initial amorphous silicon into account, the final poly-Si properties are discussed.

In Chapter 6, laser assisted process of Si is presented. The crystallization of amorphous silicon and the following doping of poly-Si layers are both carried out by CW diode laser. The thin film poly-Si solar cells are constructed and basic characterization results are given.

In Chapter 7, all of the major outcomes are summarized in an order as given throughout the thesis

CHAPTER 2

POLYCRYSTALLINE SILICON THIN FILMS

2.1. A Brief Background of Polycrystalline Silicon for Photovoltaic Applications

Silicon has an important role in semiconductor technology. It has been used for integrated circuits (IC) for more than four decades. Up to now, by the increasing demand on electronic products, silicon IC technologies dominated the market with the development of new technologies. Especially, the rapid increase in the use ICs was a result of development of complementary metal-oxide semiconductor (CMOS) ICs, which enable building of high density memories on a single silicon chip. Gateway for the fabrication of the dense CMOS chips was the use of polycrystalline silicon as the gate electrode material. The use of polycrystalline silicon reduces the parasitic capacitance by allowing formation of a self aligned structure and also because of its compatibility with high temperature it permits the fabrication of more complex structure. In addition to IC based applications polycrystalline silicon can be used for thin film transistos (TFTs) for switching pixels of liquid crystal displays (LCDs) and mechanical elements of microelectromechanical systems (MEMS) [11].

More than 80% of polysilicon was used by the semiconductor industry before 2000, however more than a decade, there is a great attention for polycrystalline silicon and now, it is mostly used for manufacturing PV cells [12]. Polycrystalline (multicrystalline) silicon is the prominent feedstock in the crystalline silicon based photovoltaic technology since the fabrication cost of polycrystalline silicon is lower and simpler to make than monocrystalline silicon. 60–80% of polycrystalline silicon was used by the solar industry between 2008 and 2014 [13]. The percentage of global production of multicrystalline, monocrystalline and thin film PV productions during the 35 years period is given in Figure 2. It is clear in Figure 2 how the production of multicrystalline PV has grown in years in comparison with monocrystalline and thin film technologies.

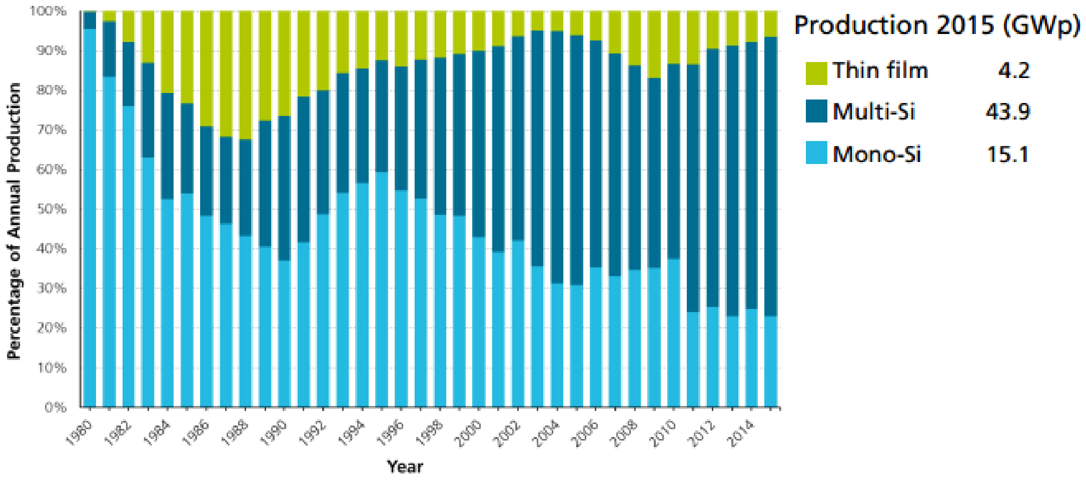

Figure 2: The percentage of global production of PV technologies [1].

Beside the growing wafer based PV technology, the cost of crystalline silicon wafer production is still high. The wafer thickness has been reduced from 500 µm to around 180 µm, which is much above the necessary light absorption. Only a few µm is enough for the absorption of the light, and the rest of the wafer is unnecessary. Making thinner wafers also brings a difficulty such as easy cracking of wafers which results in complicated processes. Furthermore, making thinner wafers will increase the process cost of the technology. However, since thicker material means high cost, the trend must be to use less material for the declination of PV prices. In this manner, thin-film approaches aim to reach low cost by starting with a low-cost material system where a thin layer of semiconductor is deposited on a low-cost substrate. It is then of a great interest to fabricate, especially, crystalline thin films on a cheap substrates like glass. This concept is called polysilicon thin film on glass.

2.2. Properties of Polycrytalline silicon thin films

Bulk polycrystalline silicon consists of different crystalline regions separated by boundaries. Every individual crystalline region is called grain and boundaries are called grain boundaries. Every grain has its own crystal orientation. In Figure 3 the difference between mono and polycrystalline silicon wafers can be easily seen. The size of the grains differ from a few nm up to several cm. The properties of boundaries have crucial effect on the properties of polycrystalline material. Especially the boundaries are the barriers for carrier transport as they create recombination centers.

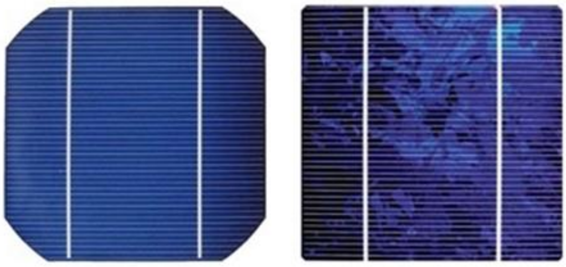

Figure 3: Monocrystalline (left) and polycrystalline (right) silicon solar cells [14]

The grain boundaries are the edges of the crystalline regions that contain disordered atom chains and incomplete bondings. These defects and dangling bonds in grain boundaries form trapping states for carriers. Dangling bonds and defects form deep energy states within the bandgap of polysilicon material [13]. These energy states behave as recombination centers near the midgap for the free carriers in conduction and valence bands. Like in a-Si, the strained bonds constitute the tail states near conduction and valence band edges as shown in Figure 4.

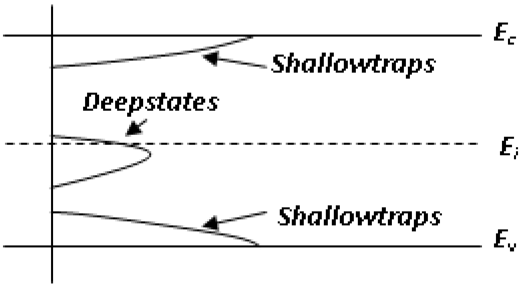

Figure 4: The effect of dangling bonds and defects

Another problem of polysilicon thin film is doping. Like free carriers, dopant atoms are also trapped at the grain boundaries. The dopant materials segregate in the boundaries. The substitutional dopant atoms choose energetically favourable places and they segregate at the boundaries and they lose their electrical properties [17]. These carriers in the boundaries create extra charge which constitutes potential barriers for carrier movement [18]. As a result, the trapped charges at the grain boundaries are compensated by oppositely charged depletion regions around the boundaries. The opposite charge in the depletion region causes curvature in the energy bands which creates potential barriers. The movement of the carriers between the grains is inhibited by the potential barriers [18,19].

Solving the Poisson's equation can explain the carrier transport and electronic structure in grain boundaries;

$$\frac{d^2V}{dx^2} = \frac{qN}{\varepsilon} \tag{1}$$

Here, N is the dopant concentration at the grain boundaries, q is the charge, ε is the permittivity. From equation (1) the barrier height can be defined in terms of dopant concentration N and the depletion region width x_d as;

$$V_B = \frac{qN}{2\varepsilon} x_d^2 \tag{2}$$

Potential barriers are significantly dominated by the substitutional dopant concentration, trap density and energy. At low dopant concentrations total number of carriers NL per unit area in a grain of length L is less than the number of traps $N_T$per unit area at the grain boundary. Almost all the free carriers of substitutional dopant atoms are trapped at the grain boundaries if the energy levels of trap states are adequately deep. Besides this, very few carriers are free. In this case, the depletion regions extend through the grains and the potential barrier qV_B is small which is represented in Figure 5 for a p-type polycrystalline silicon. As a result of the small barrier, the carriers can move between the grains.

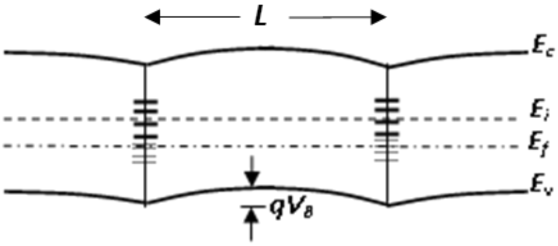

Figure 5: Grain boundary modelling of polycrystalline silicon with low dopant concentration

In the case of completely depleted grains, the depletion region of the corresponding grain boundary broadens to a distance of $L/2$ on both sides of the boundary. According to this situation, the barrier height can be defined as;

$$V_B = \frac{qN}{2\varepsilon}\left(\frac{L}{2}\right)^2 = \frac{qNL^2}{8\varepsilon} \tag{3}$$

As the dopant concentration is increased, the number of trapped carriers are increased at the boundaries which creates higher potential barrier (Figure 6). This impedes the carrier transport between the grains.

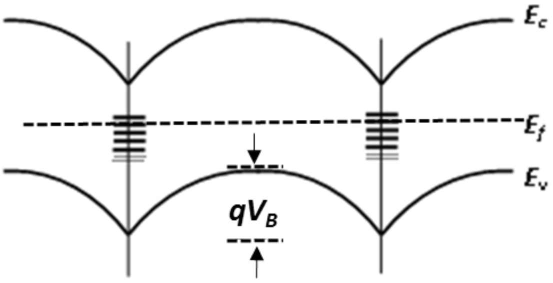

Figure 6: Grain boundary modelling of polycrystalline silicon with high dopant concentration

In addition to the dopant concentration amount, the number of trap states have crucial importance for the potential profile at the interface. Trap states are usually completely filled and neutralized, at very high dopant concentration or relatively low trap state concentration. Since the available states are filled, extra carriers are not trapped by the grain boundaries anymore (Figure 7). The extra carriers, which are not trapped, constitute neutral regions within the grains.

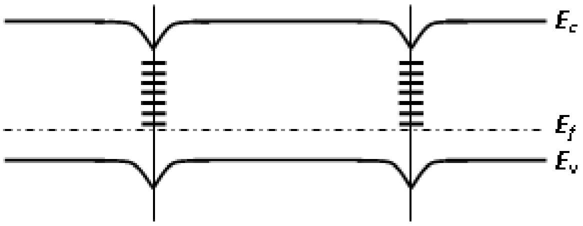

Figure 7: Modelling of polycrystalline silicon with completely filled trap states at the grain boundary

In Figure 7, it can be seen that when the available sites are completely filled the potential barrier is lowered. When the dopant concentration exceeds a critical value [19] of $N^* = N_T/L$ the trapped carrier per unit area is constant as N_T at the boundary. The depletion region width is lowered according to the formula;

$$x_d = \frac{N_T}{2N} \tag{4}$$

Using equation (2) the barrier height can be defined as;

$$V_B = \frac{qN}{2\varepsilon}\left(\frac{N_T}{2N}\right)^2 = \frac{qN_T^2}{8\varepsilon N} \tag{5}$$

The carrier transport between the grains is easier since the barrier is lowered. As a result, when the dopant atoms are introduced to polycrystalline silicon, the potential barrier around the grain boundaries first increases, reaches a maximum and finally decreases.

In polycrystalline silicon (polysilicon) thin film case the grain sizes are much lower than the bulk polycrystalline material and this limits the carrier transport with respect to the bulk polcrystalline silicon. Since the material is thin film the substrate like glass, alumina, stainless steel must be used to hold the polycrystalline silicon film. In Figure 8 the schematic of polysilicon thin film on glass is given including grains and grain boundaries.

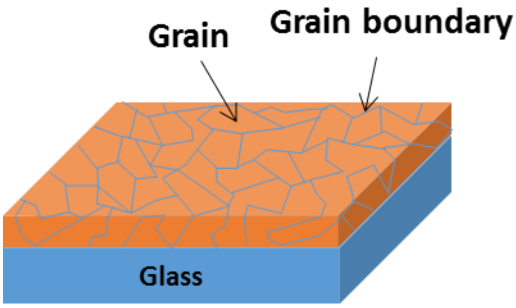

Figure 8: Polysilicon thin film on glass

Generally polysilicon thin films have thickness of 0.5-10 μm which constitutes a high surface/volume ratio. Then the surface becomes an important parameter for carrier transport. The surface contains many dangling bonds, which creates recombination and scattering centers for carriers. In addition to surface effects, the grain boundaries are also the obstacles as recombination centers for carriers.

The different scattering mechanisms like impurity and phonon scattering dominates the carrier mobility in a material. In the case of thin film polycrystalline materials, additionally, the possible scattering mechanism is specular reflection which is an elastic scattering. The carriers' velocity component perpendicular to the surface is only reversed after scattering and there is no change in momentum. This leads to no contribution to conductivity and diffuse reflection where the velocity changes with respect to the incident one and the scattering is random. The change in the energy of the carrier affects the conductivity

In solar cell applications, minority carrier transport is significantly important to achieve high efficiency values. However, due to the trapped majority carriers at the grain boundaries, the minority carriers recombine with them. This makes the lifetime τ_{eff} of minority carriers low when compared to the crystalline structures. The minority carrier lifetime can be expressed as [13]:

$$\tau_{eff} = \frac{2d\ \exp(-\frac{qV_B}{KT})}{3\sigma v D_T(E_{fn} - E_{fp})} \tag{6}$$

V_B is the height of the potential barrier, D_T is the interface trap density and $E_{fn},\ E_{fp}$ are the quasi-Fermi levels. It states that both the barrier height and grain size have an important effect of the carrier life time.

2.3. Types of Silicon Thin Film Production Methods

2.3.1. Solid Phase Crystallization (SPC)

SPC technique is the most widespread method for producing polycrystalline silicon (poly-Si) thin films [20]. Besides, it is a direct deposition approach for poly-Si production. Simply, amorphous silicon (a-Si) is deposited by any technique like Plasma Enhanced Chemical Vapor Deposition (PECVD), Hot Wire Chemical Vapor Deposition (HWCVD), Sputtering, Electron beam (e-beam) evaporation on a substrate and following thermal annealing results in poly-Si thin film. Generally speaking, SPC is mostly associated with crystalline silicon on glass concept. Thermal annealing induces nucleation sites and further annealing expands the sites into grains with grain boundaries (GBs) between them. The temperature and annealing duration can change the resulting material properties. Increase in temperature or time can further support the grain growth. High temperature results in smaller grain size than low temperature does however the full crystallization is reached faster. In contrast, insufficient temperature cannot promote a crystallization within a reasonable time. The typical annealing temperature is between 550 °C and 750 °C but the most common annealing temperature is 600 °C [21]. Poly-Si films produced by SPC can be undoped, as well as lightly doped and heavily doped in-situ by PECVD and effusion cells or ex-situ by spin-on technique. The doping control is significant for solar cell applications to maintain the carrier separation and photoconversion. The typical film thickness is between 1 μm and 3 μm. SPC produces films with small grains at about 1-2 μm which means many GBs that consist of defect and the imperfect crystalline structure contains twins and dislocations. Since poly-Si films have small grain sizes that can be comparable with diffusion length of carriers the carrier lifetime is low [22]. Another property of SPC material is that it shows a preferred orientation of <111> which has been attributed to the anisotropic rate of crystallization [23,24]. Serious works on poly-Si solar cell was carried out in 2000s and 8-9 % efficiency was achieved by Basore in 2004 [25] and after this, CSG Solar achieved a record of 10.5 % efficiency for poly-Si thin film solar cell on glass which was fabricated by SPC technique [26]. The greatest advantage of SPC method is that it is simple and cost effective. However, long annealing durations (20-36 h) and small grain sizes are the drawbacks of this technique [27]. Small grain sizes increases the volume of GBs which means that the defects and recombinations also increases. This situation decreases the film quality and can be improved by well optimized hydrogenation [28,29].

2.3.2. Liquid Phase Crystallization (LPC)

2.2.2.1 Laser Induced Crystallization (LIC)

Laser processing is used for solar cell applications for a decade in many aspects, like grooving, drilling, mesa etching, local doping, scribing [30,31]. For silicon thin films, laser beam was used for crystallization of amorphous silicon layers deposited on glass or metal foil. In contrast to direct deposition approach like SPC, LIC is based on the lateral seed layer approach which totally decouples initial nucleation from the actual growth of the active layer. Also seed layers can be fabricated for epitaxial growth. First a seed layer is formed by LIC of amorphous silicon and then in the second phase, an epitaxial deposition process is applied, that is a deposition process that reproduces the underlying crystal structure. The seed layer has a good crystallographic quality, however, to be used as an active layer in a solar cell it may be either too thin or too highly doped, or both. Laser crystallization induces crystallization by using laser light pulses to melt the silicon locally which is called liquid phase crystallization (LPC). As only a small volume of silicon is liquid for only a very short time, the substrate itself remains at relatively low temperatures. Poly-Si films with high electronic quality with high homogeneity can be achieved over large areas, even on glass substrates. LIC of a-Si is mostly used by the electronics industry to obtain thin film transistors (TFTs) for flat panel displays. The standard technique LIC of silicon is excimer laser annealing (ELA), in which a thin amorphous Si layer is crystallized by repeated pulses of a wide excimer laser beam. However this technique results in a material with a relatively small grain size (< 1 μm). Relatively small grain sizes are appropriate for TFTs but not for solar cells due to the limited efficiency by the density of GBs [32,33]. In addition, the excimer laser is not suitable for epitaxial thickening or annealing of silicon films as the laser penetration is very limited in silicon because of short wavelength (< 350 nm). An advanced technique on laser crystallization can be given by phase modulated excimer laser annealing (PMELA) which yields high quality micron sized single crystals [34]. New techniques were investigated by means of obtaining poly-Si layers with better structural quality and larger grains. Another laser crystallization technique is the sequential lateral solidification (SLS) which is a promising process [35,36]. The idea is to form grains as seeds for further lateral crystallization. Local melting and crystallization is spatially and temporally displaced from the previous crystallization event. It was observed that the laser pulse frequency, power and a-Si thickness have great effect on the final width of grains. The lower the film thickness, the laser power or the pulse frequency, the higher the quenching rate is [37]. A high quenching refers to fast crystallization and small grains. Grain sizes in the range of 2-4 μm was achieved by SLS process [38] and it is possible to reach values up to 7 mm under specific conditions [39]. So far the most notable efficiency values for poly-Si thin film solar cells prepared by diode laser crystallization has an efficiency of 8.4 % [40] which is well below SPC record of 11.7 % with Voc of 585 mV [41]. Another laser approach is continuous wave (CW) diode laser and in this perspective, in 90s, some detailed studies by Toet et al. were handled [42,43]. Here CW laser (514.5 nm wavelength) with a 1 μm spot size was used to form crystallised spots 5–10 μm apart. Also, Shimokawa et al. announced CW laser recrystallised solar cell with a 6.52 % efficiency which was produced by CVD method onto alumina substrate [44]. The crystallization was done at 400–450 ◦C in a nitrogen ambient and double stack buffer layer (Si_3N_4/SiO_x) was used to protect the film from the possible contaminants that can diffuse from glass substrate to silicon layer. 400 nm of poly-Si film with high mobility (690 cm^2/Vs) was obtained by 512 nm CW laser in 2004 [45]. It was observed that the cracking in the film limits the crystal size and by using the stripe adjustment some of the cracking problems were solved with up to 4 mm of grain size. Later on, this technique was improved by using pulsed UV and infrared CW laser and <111> preferential orientation was achieved by recrystallization of μc-Si films on glass [46]. Method of obtaining larger grains of up to tens of μm was taken into consideration as the lateral growth of grains. CW diode laser approach (λ = 940 nm, intensity 24.7 kW/cm^2) was applied with a diamond like carbon photo-absorbing layer coated onto the surface of the silicon film to improve the heat transfer to the silicon layer. Laser crystallization can be used for SPE approach in which laser crystallized regions behave as seed layers for the post deposited and annealed a-Si. SPE process enables the standard SPC temperature of 600 ^oC to be lowered. The activation energy during the SPC process was calculated for nucleation as 3.62 eV and for lateral growth as 2.64 eV. Thus it was concluded that SPC temperatures can be lowered for further crystal growth. In recent years line shaped CW diode laser is mostly the preferred technique in solar cell applications. The line shaped laser also enables larger area crystallization. In this perspective absorber grain sizes up to centimetre and solar cell efficiency of 12.1 % are achieved on a 5x5 cm^2 glass substrate [47].

2.2.2.2. Zone Melting Crystallization (ZMC)

Zone melting crystallization is also another liquid phase approach where Si material is melted by the heat of halogen lamps. In this method a microcrystalline silicon layer is deposited on a substrate and focused light of halogen lamp is scanned over the surface of the sample. The melted microcrystalline silicon is recrystallized which is called zone melting recrystallization (ZMR). ZMR was first introduced by Leitz in 1950 [48] and in 60s it was researched for growth of low melting point semiconductors [49]. In 80s, interest on ZMR increased in terms of silicon material when silicon on insulator (SOI) film concept became of interest. In 1990s the PV applications of ZMR were published by Mitsubishi [50] and Fraunhofer ISE [51]. In 2000s extensive studies on ZMR of silicon was conducted [52,53]. Basically light of halogen lamp is focused on silicon surface by the elliptical reflectors. The zone, where the light is focused, becomes locally molten around 1413 ^{o}C and during the scanning the molten region quickly solidifies as a crystal just after the focal beam line. The crystallized regions act as seed layers for the further growth and it is possible to obtain grain sizes of several milimeters in width and several centimeters in length by ZMR technique [54]. The experiments showed that percentage of <100> orientation depends on the scanning velocity and thickness of the film [55]. The beam and scanning parameters has a significant role on the properties of resultant poly-Si material. To obtain reasonable efficiency values, low dopant level may be necessary for absorber layer. Since the substrate is exposed to high temperature, this technique is not suitable for glass substrate having low softening point. Most of the experiments were done on foreign substrates like graphite, ceramic, SiC. The intermediate layer on the substrates has an important role on the material properties. ZMR on samples without the intermediate layer did not yield large-grained silicon layers [56]. Conversion efficiencies of 11 % and 8.3% were obtained on both graphite and SiC substrates [57, 58].

2.2.2.3. Electron-Beam Crystallization

Electron beam crystallization (EBC) has the same process approach like zone melting crystallization. Instead of using focused lamp source, electron beam is used to melt the silicon material. Electron beam is released from a heated tungsten filament and focused into a line using electrodes.

In 1968, John C. introduced EBC of amorphous silicon [59]. Amorphous silicon was deposited onto glass microscope slides by evaporation and sputtering. The crystallization was supplied by electron beam scanning and electron beam bombardment. Since the thickness of the film was a few hundred angstrom the sufficient crystallization was not achieved for photovoltaic applications. In 2011, EBC was demonstrated on a-Si films on glass substrates using SiC as a buffer layer. 4.7 % efficiency with 545 mV of V_{oc} was achieved by heterojunction solar cell by electron beam crystallized absorber layer. Films were pre-heated at 700 ^{o}C before crystallization and grains up to 1x10 mm^2 was achieved by EBC.

2.2.3. Metal Induced Crystallization (MIC)

Although SPC has several advantages, such as cost effective, simple, etc., the major drawbacks of this technique are quite long crystallization annealing time (20-40 h) and small grain size of 1-2 μm. It is also possible to use SPC poly-Si film as a seed layer as long as large grained (> 10 μm) material can be produced. On the other hand, crystallization temperature and duration can be lowered by the addition of certain metals such as Al, Ni, Au, Ag, Pd etc., which also promotes larger grains [60]. These techniques are commonly referred to a metal induced crystallization (MIC). In this MIC, metals lead to lower thermal annealing temperature below eutectic temperatures of the Si/metal systems for the crystallization of a-Si. The process starts with the intermixing of metal and semiconductor. This can happen even at room temperature [61]. The metal atoms induce an instability in the bonding character of semiconductor and weakens the Si bonds to promote Si nucleation. Without the effect of metal this instability can hardly occur at temperatures below 550 ^{o}C. The physical origin of this instability is due to the ability of metal to screen coulomb interaction by its mobile electrons [62]. Some metals like Ni, Pd are compound forming metals and others like Al, Ag, Au constitutes eutectic metal-silicon system. All MIC processes are based on the difference in chemical potentials (amorphous-crystalline) which provides a driving force for dissociation and nucleation [63]. Like Ni, compound-forming metals result in crystallization after the formation of the most stable Si rich silicide phase [64]. For example in the Ni case, the crystallization happens by a $NiSi_2$ silicide phase moving through the a-Si and not by the metal itself. The chemical potential of Ni and Si is different at the a-Si/$NiSi_2$ interface compared to the poly-Si/$NiSi_2$ interface. As a result, Ni atoms will diffuse through the $NiSi_2$ toward the a-Si/$NiSi_2$ interface while Si atoms diffuse toward the poly-Si/$NiSi_2$ interface [64]. It is hard to remove the remaining $NiSi_2$ phase and it will be incorporated in the active part of the solar cell. As such, MIC with compound-forming metals is not suitable for solar cell applications. Eutectic metal-silicon forming systems are much more desirable due to the limited solubility of the metal in the growing c-Si layer, wherein the metal will be rejected from the silicon. However, not all eutectic forming metals are suitable for solar cell applications. The crystallization with eutectic systems occur in three steps; (1) dissociation of silicon atoms into the metal, (2) diffusion of silicon atoms through the metal layer, (3) nucleation of silicon atoms and coalescence of available nuclei and silicon atoms. For example Au, and Ag forms deep level defects in the band gap of silicon which are detrimental for poly-Si electrical quality [63]. In this manner Al is the suitable eutectic forming metal due to the associated defect level, 60 mV below the conduction band which leads to a p-type doping of around $3x10^{18}$ cm^{-3} [65].

CHAPTER 3

METAL INDUCED CYSTALLIZATION

In this thesis, MIC is realized through Au and dominantly Al induced crystallization (AIC) techniques. Au was used as nanoparticles (AuNPs) obtained after annealing of very thin Au layer on Al:ZnO (AZO). In this manner, less metal contamination in final poly-Si layer was aimed by this technique. AIC technique was extensively studied. In this chapter effects of buffer layer on AIC process and basic characterizations of final poly-Si films formed by AIC are given dominantly.

3.1. Gold Induced Cystallization

Gold is one of the eutectic metal-silicon forming metal which has a low eutectic temperature in contact with silicon (363 ^{o}C) with respect to Al-Si eutectic temperature of 577 ^{o}C. In 1980s, reaction between Au, Al, Pd, Pt and amorphous silicon was studied and it was found that the crystallization of Si by Al and Au is possible much below at 250 ^{o}C [66]. the characteristic of Si/Au bilayers were observed and electron spectroscopy studies showed that although no definite compounds were formed at room temperature, some intermixing takes place, giving Si a metallic nature [67], [68]. It was shown that Au/a-Si system has a metastable phase like Au_3Si which is formed at low temperatures [69] and the existence of Au silicides were confirmed by Green and Baure before [70]. In Figure 9 the Au-Si phase diagram is given.

Gold induced crystallization of a-Si results are used by the permission of Elsevier publishing with licence number of 3921330547990.

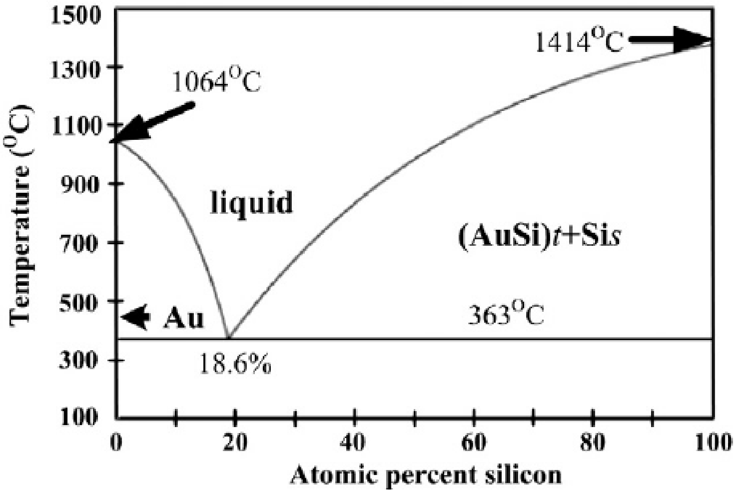

Figure 9: Au-Si equilibrium phase diagram [71].

It has been known that metals like Ag, Ni, Au create deep level defects and recombination centers [63]. This truth is limited by metal diffusion and solubility and is related with the metal amount deposited on the a-Si and the annealing temperature.

3.1.1. Crystallization of a-Si by gold nanoparticles (NPs)

In this part of the thesis the Au induced crystallization of e-beam evaporated amorphous silicon (a-Si) was investigated. Au nanoparticles (NPs) instead of a continuous thin film was used as NPs was expected to generate less metal contamination than conventional metal film. Since Au can be de-wetted by annealing it is easy to shape Au film into NP. In contrast, Al and Ni cannot be easily de-wetted to NP homogenously by annealing a thin film. Generally, Al and Ni NPs are synthesized by chemical methods which require complicated process steps.

3.1.1.1. Sample Preparation

As a substrate, AF 32 Schott glasses with a thickness of 1.1 mm were used. 400 nm of AZO (Al doped ZnO) was coated by sputtering technique. The AZO sputtering target has 2 % Al. Here, AZO film also provides good conductivity for SEM analysis of Au

NPs. For nanoparticle formation, 5 and 15 nm Au films were deposited onto AZO film by e-beam method and then the samples were annealed at 500 ^oC in a classical furnace under N_2 atmosphere. Au NPs were imaged by Scanning Electron Microscopy (SEM). Figure 10 shows the SEM images of NPs formed by 5 nm and 15 of Au films.

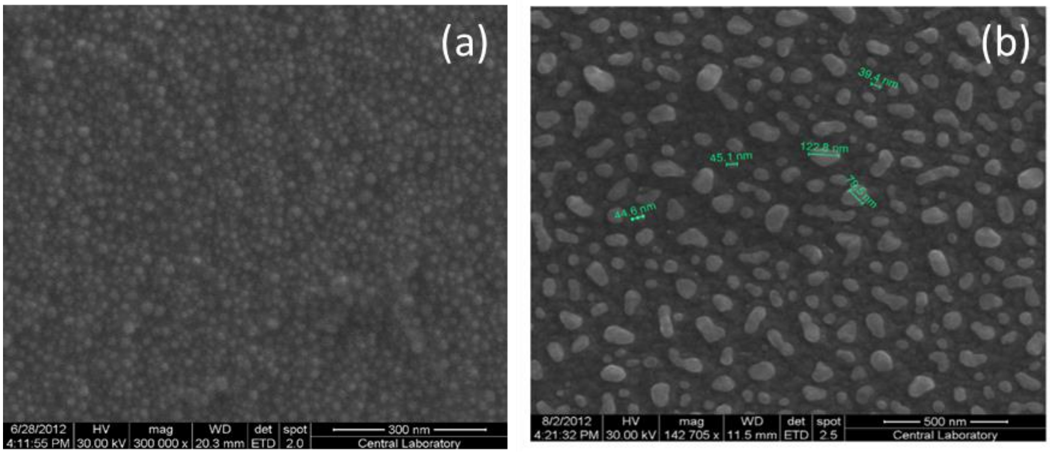

Figure 10: SEM image of AuNPs on AZO film after 1h of annealing at 500 ^oC by 5 nm Au film (a) and 15 nm Au film.

SEM images of NPs indicate that the best NP formation was achieved with 1 h annealing of 15 nm Au film at 500 ^oC. 5 nm annealed film results very small and agglomerated NPs whereas 15 nm annealed film creates widely spaced, larger particles with NP distribution changing between 50 nm and 150 nm. NPs formed with 15 nm annealed film is used for the silicon crystallization experiments. After NP formation, 1 μm thickness of amorphous silicon (a-Si) was deposited by e-beam with a deposition rate of 1 Å/s. During the silicon deposition the substrate temperature (T_s) was kept at 200 ^oC and the pressure of the vacuum chamber was 5 $x10^{-7}$ Torr. The samples were annealed between 500 ^oC and 600 ^oC in N_2 atmosphere for crystallization process. The fabrication process is shown in Figure 11.

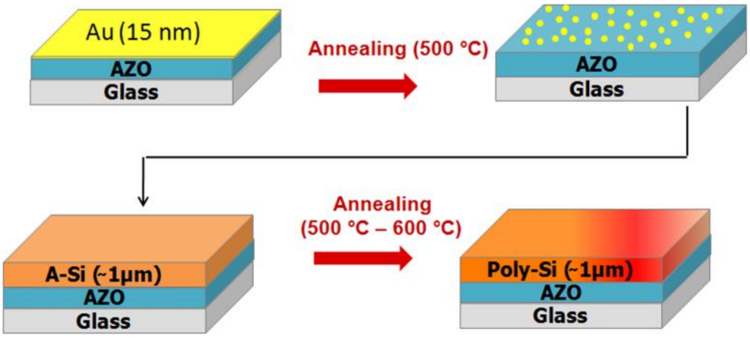

Figure 11: Fabrication process of Au induced a-Si crystallization

3.1.1.2. Results

As mentioned before, conventional SPC process requires more than 20 h of annealing at 600 °C for poly-Si formation [72]. Moreover, the crystallization at lower temperatures expands the annealing duration. Here AuNPs catalyzes the crystallization process and lower the crystallization duration and temperature. In Figure 12 the Raman measurements of the samples with AuNPs that were annealed at 500 °C, 550 °C and 600 °C for 12 h are given. It can be easily inferred from this figure that the amorphous structure is maintained for the sample annealed at 500 °C.

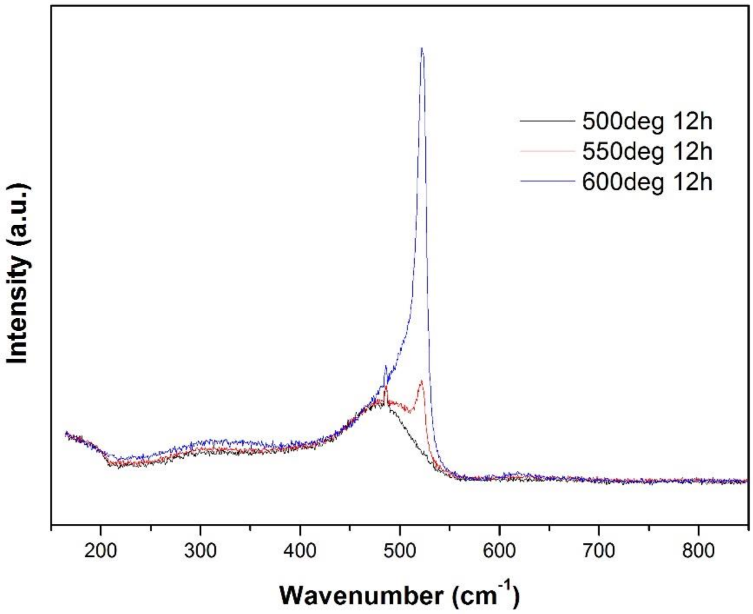

Figure 12: Raman measurements of samples annealed for 12 h at 500 ^{o}C, 550 ^{o}C and 600 ^{o}C.

The small peak at 520 cm^{-1} shows that crystallization starts with 550 ^{o}C annealing after 12 h. However, 500 ^{o}C annealed sample is still in amorphous phase. The tiny peak at the top of the amorphous profile is due to some leakage of light from environment during the measurement. The Raman peak of 600 ^{o}C annealed sample shows large amount of crystallization. As expected, higher the temperature the more crystallization. However, normally SPC process results in less or no crystallization at 600 ^{o}C for 12 h with respect to AuNPs induced crystallization.

The crystallization was also analyzed by X-ray diffraction (XRD) measurements, which also shows the possible grain orientations. Unless the surface is scanned, only small portion of the sample is investigated since Raman analysis is limited by the spot size of the laser. On the other hand, XRD measurement is not restricted by a small probe size, X ray is emitted to a larger surface. In Figure 13 the XRD measurement of each sample is given.

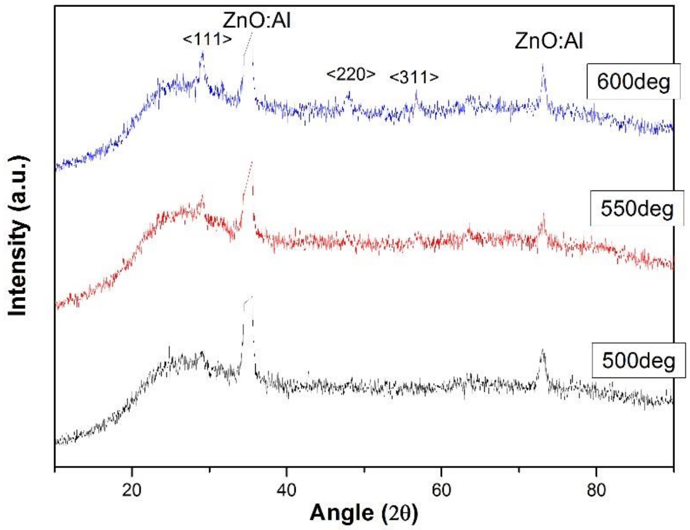

Figure 13: XRD measurements of samples with annealed for 12 h at 500 °C, 550 °C and 600 °C.

In Figure 13, the crystalline silicon orientations of <111>, <220> and <311> are detected for the sample annealed at 600 °C, weakly appears at 550 °C and barely visible at 500 °C. Among these orientations, <111> peak dominates since it has the lowest free energy [73] and the approximate grain size was analyzed by the Scherrer equation given below [74]. The notable peaks at 2θ angles around 35 and 74 are coming from the AZO interlayer.

$$D = \frac{K.\lambda}{\beta.cos\theta} \tag{7}$$

Where D is the average grain size, K is the Scherrer's constant, λ is the X-ray wavelength (1.542 Å), β is the full width at half maximum (FWHM) of the peak and θ is the Bragg angle. The calculated average grain size from <111> peak for the sample annealed at 600 °C for 12 h is 15.6 nm. The XRD results show that the crystallization starts at temperatures as low as 500 °C and reaches a high fraction at 600 °C. In order to find out if the crystallization can occur in a shorter time interval, the same experiments were performed for an annealing time of 2 h at 600 °C. For comparison samples both having AuNps and without AuNPs were annealed. The Raman results of the samples having AuNPs annealed at 600 °C for 2 h and those without AuNPs annealed at 600 °C for 12 h are given in Figure 14.

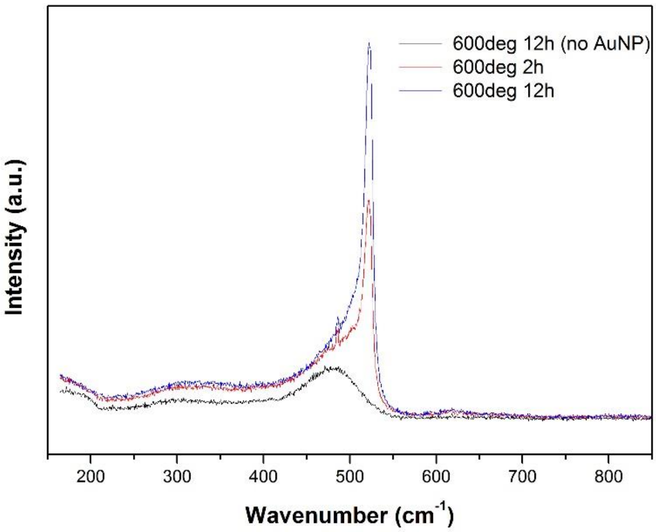

Figure 14: Raman measurements of the samples with and without AuNPs annealed at 600 °C

Figure 14 shows that, AuNPs induced crystallization within 2 h, however the sample without AuNPs has no crystallization even after 12 h annealing. Short annealing time of 2 h is attractive when compared to classical SPC method. It is clear that as the annealing time increases, the crystalline amount increases. Also, the annealing for 2 h is still giving acceptable crystallinity with respect to 12 h annealing in terms of AuNPs induced crystallization. The crystalline amount $(X_c)$was calculated by deconvolution of Raman spectra. The deconvolution was used with three different peak components of crystalline, intermediate and amorphous phases which corresponds to 520 cm^{-1}, 510 cm^{-1} and 480 cm^{-1} respectively. X_c was calculated by using non-linear fitting method and Gaussian distribution according to [75]:

$$X_c = \frac{(I_c + I_i)}{(I_c + I_i + I_a)} \tag{8}$$

Where I_c, I_i and I_a are the normalized intensities of the crystalline, intermediate and amorphous peaks. The calculated crystalline amounts are presented in Table 1.

Table 1: Crystallinity amounts of AuNPs induced samples with respect to different annealing temperature and time

Annealing Temperature	Annealing Time (h)	CrystallintyAmounts (%)
500	12	amorphous
550	12	25
600	2	66
600	12	73

The calculated crystalline amounts confirm the Raman results in Figures 14 and 12. The crystallinity increases both by time and temperature. Furthermore, there is no notable difference between 2 h and 12 h of annealing at 600 ^{o}C which indicates that metal NPs have great effect on crystallinity.

One can think about Al diffusion from AZO into silicon during annealing, as stated in Figure 14, 12 h of annealing is applied both for the samples having AuNPs and without AuNPs. Sample without AuNPs shows no crystallization which remarks that there is no aluminium induced crystallization (AIC). Furthermore, AIC process necessitates Si dissolution in an Al matrix which is not the case here. During the growth, some of metal atoms are expected to be dissolved in the crystal matrix. This cause a serious source of contamination which may degrade the electrical properties of resultant poly-Si film. This problem can be reduced by a post processing using technique like metal gettering. However, here only the effect of AuNP on crystallization was studied. Alternatively, using less Au nanoparticles would generate less contamination. It is then of interest to determine the minimum Au thin film thickness that would generate the optimum nanoparticle size and distribution.

3.2. Aluminium Induced Crystallization (AIC)

MIC has the advantage of low temperature crystallization, however, metal contamination is the drawback of this technique. When the metal is incorporated into the Si matrix the electronic properties of silicon is changed by the metal atoms. Some portion of the metal atoms resides in the active sites of Si matrix. In some cases the metals create defect states. In this sense, Al is the most suitable one as it acts as an acceptor dopant in Si and diffuses relatively slowly in Si. Crystallization by Al is called Aluminium Induced Crystallization (AIC). As a result of AIC of amorphous silicon highly p doped (p^+) poly-Si layer is formed. AIC method has been used to crystallize amorphous silicon layers on substrates like glass [76] and ceramic [77]. Briefly, AIC (also called Al induced layer exchange or ALILE) of a-Si is based on the overall layer exchange of adjacent Si and Al films and transformation of amorphous to polycrystalline Si during thermal annealing [78,79]. In 1977, Majni and Ottaviani investigated Si-wafer/Al/a-Si stack where Al and Si layers were deposited by e-beam evaporation onto <100> Si wafer [80]. After annealing at 530 ^{o}C for 12 h the layer exchange of Si and Al was observed. Also, the epitaxial growth of Si on wafer was observed and the process was called solid phase epitaxy (SPE). About two years later the same authors discovered that a barrier layer at the Al and Si interface has an important role on diffusion control during the layer exchange and resulting epitaxially grown Si layer is dominated by the initial Al thickness [81]. In 1981 Tsaur et al. used this technique and constructed solar cell on n-type monocrystalline wafer and obtained efficieny of 10.4 % [82]. In 1998 Nast et al. demonstrated the layer exchange process on glass and obtained uniform poly-Si films on glass [80]. Each of the Al and Si layers are deposited onto glass by e-beam evaporation, PECVD or sputtering. The Al/Si stack is annealed between 450-550 °C for durations of 30 min to 20 h. In this layer exchange process the crucial point is the formation of AlO_x (a few nm) membrane between Al and Si layer. The AlO_x layer, has an important role as it is fixed between the Al and Si layers, controls the diffusion [83] The typical AlO_x layer is formed by after the deposition of Al layer the film is exposed to air (for 2 h, 24 h, 1 week…). During the annealing, the dissolved Si atoms diffuse through the Al layer. When a certain concentration of Si in the Al grains of the Al sublayer is exceeded the Si nucleation takes place.

3.2.1. Aluminium-Silicon interaction

AIC process simply occurs when a-Si is in contact with Al under the temperature below the Al-Si eutectic temperature (577^{o}C). This process is called aluminium induced layer exchange (ALILE). The driving force behind the crystallization of a-Si is the Gibbs free energy difference between amorphous and crystalline phases. Since crystalline phase is more stable than amorphous phase Gibbs free energy is reduced by the transformation of amorphous to crystalline silicon. The covalent Si-Si bond has a relatively strong bonding of 2 eV/bond. The standard solid phase crystallization (SPC) process of a-Si about 3-4 eV which is relatively high [84]. This is the reason of having long crystallization durations of SPC [85]. However, when silicon is in contact with aluminum the metal atoms behave as catalyst and lowers the crystallization temperature and duration. Thus, this process has a lower activation energy which is also stated by Gall et al. as 1.8-1.9 eV [86]. Before diffusion of Si atoms into Al layer the Si bonds are dissociated by the metal atoms. This dissociation mechanism of amorphous silicon has two models: (1) Tu’s interstitial model [87] and (2) Hiraki’s screening model [62]. In model (1) It is accepted that the initial intermixing of Al and Si atoms takes place at the interface. The Si-Si bonding nature is changed by the jump of Al atoms into Si and forming metal interstitials in the silicon side. Si-Si covalent bonds no longer remain in the original localized state due to the interstitial defects. The bonding structure shifts to a non-covalent bonding structure which is weaker than covalent bonding. As a result of bond weakening the dissociated Si atoms diffuse into the Al layer. In model (2) rather than jumping of Al atom into Si, the weakening of Si-Si bonding at the interface is due to the ability of the metal to screen the Coulomb interaction by its free electron. Screening effect causes a transition of non-metal to metal-like bonding of Si material within a few monolayers at the interface [88]. A uniform electron gas is formed in this region and also valence electrons of Si in this region are not associated with specific atoms anymore. The atomic motion in the electron gas of a metallic-like compound is more mobile than the motion in the bulk counterpart of semiconductor where covalent bonding takes place.

Hiraki’s model was supported by the analysis of monolayer by monolayer growth of Au on Si surface. The necessity of the existence of a critical layer thickness (4 monolayers) was understood in order to start a reaction between Si and metal [62,88].

If the critical thickness is not achieved the metal acts as a non-metal and even if the crystallization temperature is around 800 ^{o}C the metal shows no reaction with the silicon. The instability of the covalent Si-Si bonding is broken if the metal layer is deposited at least at the thickness of critical value. The same situation was observed with Al by Radnoczi et al. as 3 or more monolayers is necessary for the screening effect [89].

Once the dissociation of amorphous silicon is provided, the Si atoms start to diffuse into Al layer [90]. In Figure 15 Al-Si equilibrium phase diagram is given. This system shows that 1.5 % Si atoms can dissolve in Al up to eutectic temperature of 577 ^{o}C [91]. After dissociation of Si the Al is subjected to Si supersaturation during the crystallization.

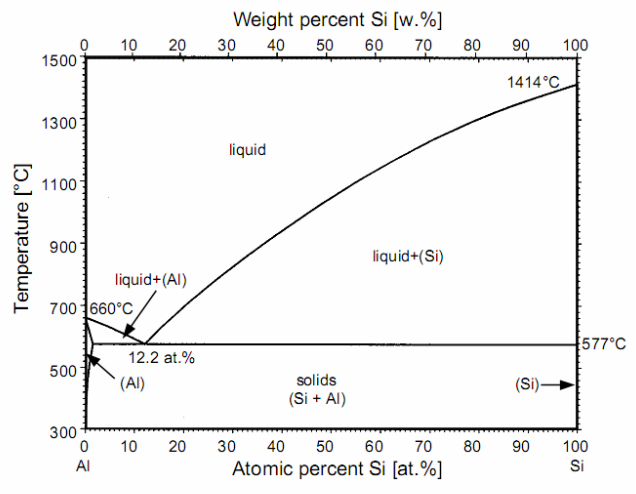

Figure 15: Al-Si equilibrium phase diagram [92]

This supersaturation is maintained by the difference in Gibbs free energies of amorphous and crystalline phases. In general the change of Gibbs free energy (ΔG) is evaluated;

$$\Delta G = \Delta H - T\Delta S \tag{9}$$

Where ΔH and ΔS are the enthalpy and entropy changes respectively. T is the system temperature. In AIC case, change in Gibbs free energy can be expressed with the difference in Gibbs free energies of amorphous and crystalline phases as;

$$\Delta G = G^{a-Si} - G^{c-Si} = H^{e} - T\,S^{e} \tag{10}$$

Where H^{e} and S^{e} are the molar excess enthalpy and entropy on the transition from a-Si to c-Si. This excess Gibbs free energy is related to the activity [93];

$$\Delta G = RTlna \tag{11}$$

Where R is the gas constant and T is the temperature. Here, activity is related to the supersaturation of Al with Si solute which can be calculated for a specific temperature if the molar excess enthalpy and entropy are known. The molar excess enthalpy and entropy of a-Si in relation to c-Si are determined before as 11.9 kJ/mol [94] and 1.66 J/(mol K) [95]. In the light of these values, for example, the activity "a" of a-Si relative to c-Si can be calculated as 6 for 475 ^{o}C. According to equation (10) G^{a-Si} and G^{c-Si} are the chemical potential of Si in Al when in contact with amorphous and crystalline silicon respectively. Both the a-Si/Al and c-Si/Al phases are in thermal equilibrium and chemical potentials of each phases are equal in individual systems.

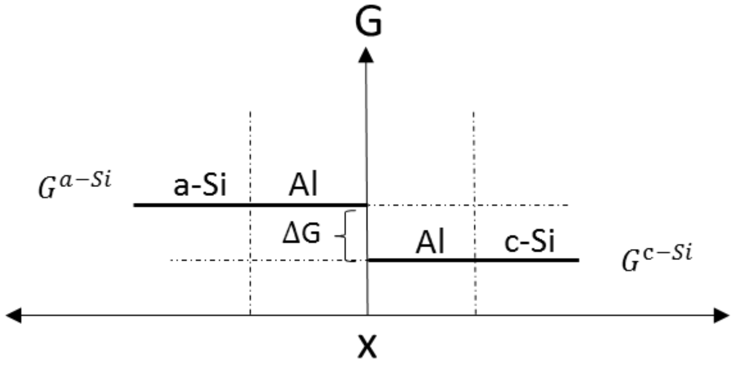

Figure 16: Schematic of Gibbs free energies of a-Si/Al and c-Si/Al systems [83]

Figure 16 shows the Gibbs free energy level difference between a-Si/Al and c-Si/Al systems. The two systems are not in equilibrium. The excess amount of chemical potential, ΔG, is the driving force of crystallization. The whole system will equate the chemical potentials to create a stable structure. The Si diffuses from a-Si/Al interface to Al/c-Si interface. The chemical potential is in relation with the dissolved Si concentration in the solvent (Al). Up to Si solubility limit of Al, in other words before being saturated, near the Al-Si interface the solution is assumed as ideal-dilute Al-Si solution and the chemical potential of a dissolved component is [96]:

$$G_i = G^* + RTlnX_i \tag{12}$$

Where G_i is the standard Gibbs free energy (chemical potential) and X_i is the relative concentration of the solute. Simply the system can be defined as:

$$G^* + RTlnX_{Al/cSi} + \Delta G = G^* + RTlnX_{Al/aSi} \tag{13}$$

$$\Delta G = RTlnX_{Al/aSi} - RTlnX_{Al/cSi} \tag{14}$$

Where $X_{Al/aSi}$ and $X_{Al/cSi}$ denotes the Si concentrations in Al when in contact with a-Si and c-Si. If equation (13) is combined with (11) it can be defined as:

$$a * X_{Al/cSi} = X_{Al/aSi} \tag{15}$$

When the system is saturated, in other words when Al reaches the maximum Si solubility in accordance with a specific temperature the nucleation starts as indicated in the Al-Si phase diagram. Within the Al, the silicon crystals are released as a result of supersaturation and the growth of silicon grain starts. During the growth, the Gibbs free energy of Si solute is increased by the diffusion of Si atoms into the Al solution. This chemical potential is lowered as a result of extraction of the Si from the solution by the crystalline Si phase and the Si atom joins the growing nuclei or grain. During the layer exchange, silicon crystals grow until each grain comes in contact with other grains if there is an adequate amount of Si and Al.

A Si nucleus is formed within the Al layer at the Al/a-Si interface after a short annealing time. The Si nuclei become grains and grain growth occurs laterally due to the confinement by the AlO_x layer and the substrate until the Al is replaced by the growing Si grains. Si nuclei grow into the Al layer up to touch the adjacent Si grain. The steps at different annealing durations of ALILE process are shown with the Focused Ion Beam (FIB) images in Figure 17.

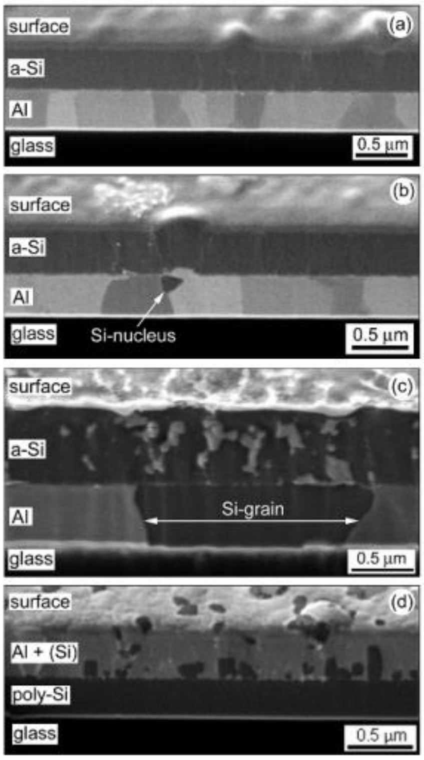

Figure 17: FIB images of ALILE process. (a) before annealing, (b) after annealing at 500°C for 5min, (c) annealing at 500°C 10min annealing; (d) 60min annealing at 500°C as a result of glass/poly-Si/Al+Si [83].

As seen in Figure 17, an Al+Si residual layer is formed on the top of the structure at the end of the exchange process. Al part is segregated on top with secondary Si islands due to the Al repulsion by the growing silicon nucleates. In order to use the formed poly-Si layer the residual layer must be removed. It can be removed by selective etching or direct polishing. The most notable properties of AIC poly-Si films are having continuous, nearly 100 % crystalline fraction and large grain sizes more than 10 μm. Since AIC poly-Si layers are highly doped (~$3x10^{18}$ cm^{-3}), they are not suitable for using as absorber layers in solar cell configuration. Epitaxial thickening is necessary on AIC poly-Si films as absorber layer for longer carrier lifetime.

The easiest way of understanding the crystallization is doing Raman spectroscopy characterization. In Figure 18 the normalized Raman analysis of AIC poly-Si film and reference crystalline silicon wafer (c-Si) is given.

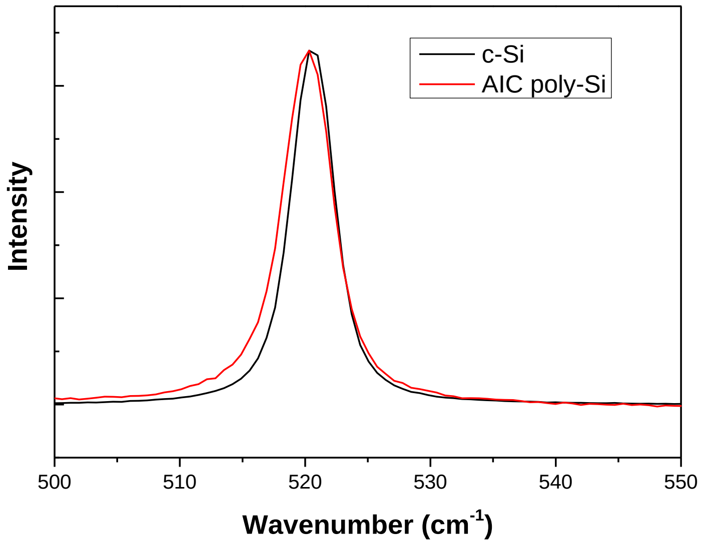

Figure 18: Raman spectroscopy of monocrystalline silicon and AIC poly-Si

As seen in Figure 18 the AIC poly-Si film has comparable crystalline characteristic with the reference monocrystalline silicon. This sample was produced at GÜNAM laboratories with Al thickness of 180 nm and a-Si thickness of 360 nm. Prior to a-Si deposition the Al film was exposed to air in clean room conditions for AlO_x formation. After annealing at 475 ^{o}C for 8 h the residual layer was removed directly by mechanical polishing.

3.2.2. Buffer layer optimization and AIC poly-Si formation

In this part of the thesis, polycrystalline silicon (poly-Si) thin films were fabricated by using Aluminium Induced Crystallization (AIC) of amorphous silicon (a-Si) on SiN_x- or AZO- (Al-doped ZnO) coated glasses. Initially the buffer layer between the glass and Si was optimized. Although, both SiN_x and Al-doped ZnO (AZO) layers were used as the buffer layer, the studies were dominantly concentrated on SiN_x layer. Generally, SiN_x and AZO buffer layers are used for Silicon based thin film studies [97,98]]. Different types of SiN_x layers were deposited by varying the deposition conditions. AIC poly-Si films were processed on the SiN_x and AZO layers. The effect of the different buffer layers on the poly-Si films were investigated by means of electrical and dominantly structural analysis. In other words, the standard AIC process was established.

3.2.2.1. Sample Preparation

The buffer layer between the glass and silicon film is expected to influence the final material quality. Buffer layers mostly aims blocking the diffusion of contaminations (O, B, Na, K, Al, Fe, etc.) from the substrate into silicon film during thermal processes. Also buffer layer improves the adhesion between the substrate and the film. Accordingly, the morphology and content of the buffer layer can affect the electrical and structural properties of films. The effect of buffer layer on the diffusion of the contaminants from the glass was experienced before in GÜNAM labs which is confirmed by Secondary Ion Mass Spectroscopy (SIMS) shown in Figure 19.

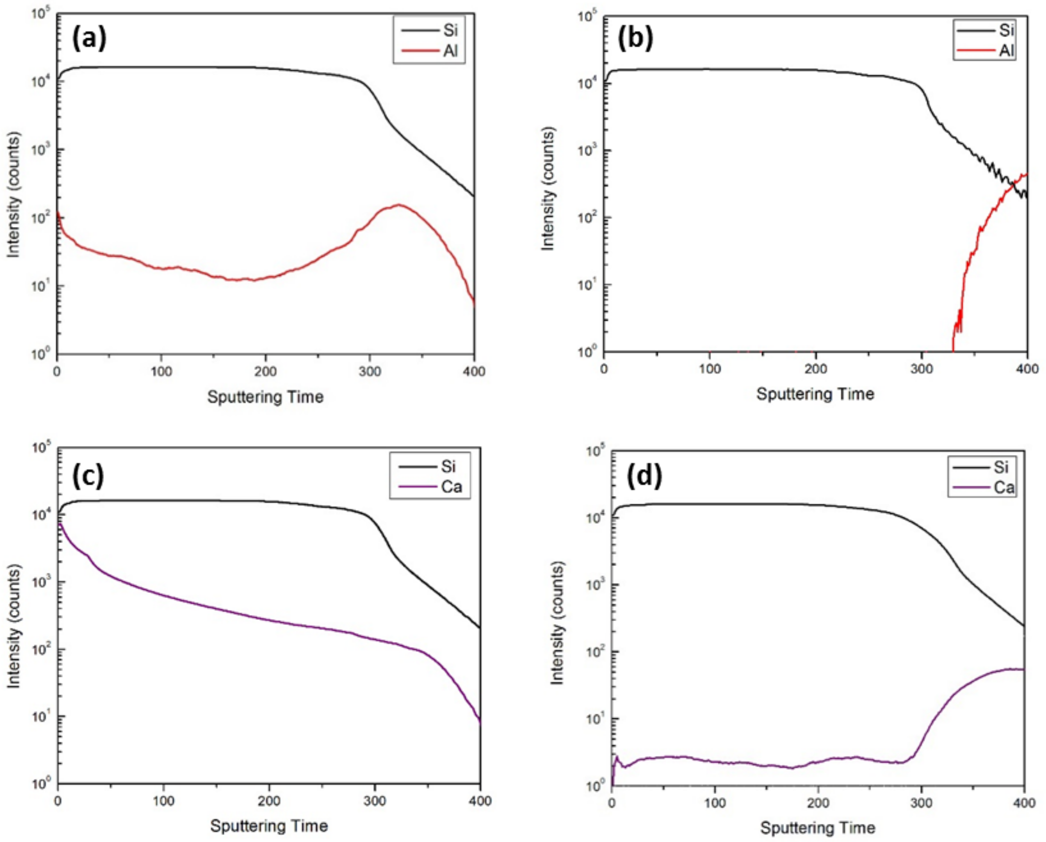

Figure 19: SIMS measurements of Si thin film on glass without (a, c) and with (b, d) SiN_x buffer layer [99].

Al and Ca detection was carried out on Si thin films after annealing having SiN_x buffer layer (Figure 19b and 19d) and without buffer layer (Figure 19a and 19c). The intensity of SIMS results show that the Al and Ca diffusion is nearly stopped when there is a buffer layer.

Schott AF ECO 32 Glass with a thickness value of 1.1 mm was used as a substrate which resists high temperatures up to ~750 °C. This type of glass was also used for all of the further AIC experiments presented in this work. First, the glasses were cleaned in ultrasonic bath with acetone, isopropanol and distilled water for 10 min in each step. Then the glasses were dipped into 10 % HF (Hydro fluoric acid) solution for 15 sec and then cleaned with distilled water. Silicon nitride (SiN_x) deposition was carried out by Plasma Enhanced Chemical Vapor Deposition (PECVD) system which was designed and manufactured by Vaksis Ltd. The SiN_x film was deposited by decomposition of ammonia (NH_3) and Silane (SiH_4) precursor gases. During the SiN_x deposition the gas pressure inside the chamber was kept at $1.3x10^2$ Pa, and the substrate temperature (T_s) was 200 °C. NH_3 and SiH_4 gases with different NH_3/SiH_4 ratio were used to obtain different combinations of SiN_x buffer layer. The deposition conditions of SiN_x layers are given in Table 2.

Table 2: PECVD deposition conditions of SiN_x layers

	NH_3	*SiH_4*	*NH_3/SiH_4*	*Power(W)*	*Thickness(nm)*
a	150	150	10	100	85
b	200	100	20	100	134
c	100	200	5	100	107
d	50	250	2	100	110
e	50	250	2	200	114

Here, NH_3 is pure while SiH_4 is used as 10 % in H_2. For this reason the real NH_3/SiH_4 ratio of the mixtures are given in Table 2. The properties of SiN_x layers were examined in terms of refractive index. The refractive indexes of the samples were investigated by ellipsometer. The ellipsometer results are given in Figure 20.

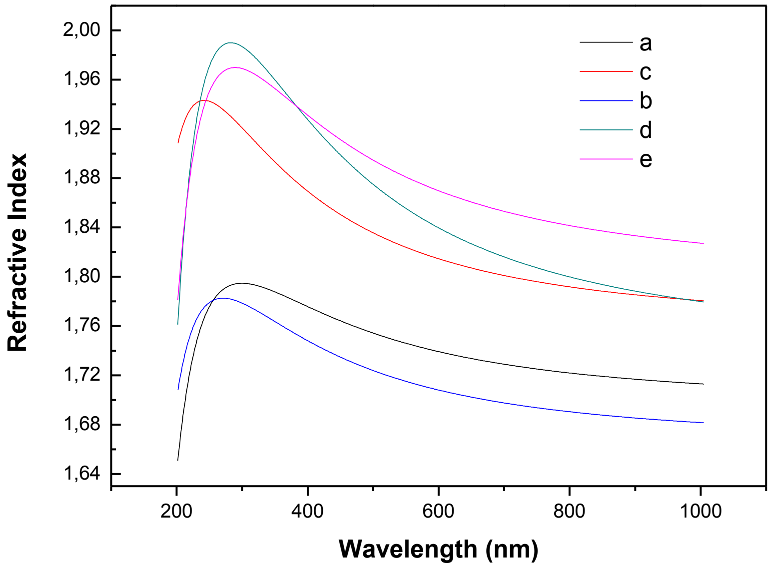

Figure 20: Refractive index results of deposited SiN_x layers with different NH_3/SiH_4 fraction

The ellipsometer results show that refractive index increases as NH_3/SiH_4 amount is decreased. Normally, for a good SiN_x layer, the refractive index is accepted around 2 [100]. Sample “d” seems to be having the highest refractive index. Samples "d" and “e” have the same amount of gas mixtures however “e” has the deposition power two times sample “d”. According to these results sample “d” seems to be the best one for the further AIC experiments. The effects of buffer layer on AIC poly-Si film properties were investigated by using different SiN_x layers. Because of this, one more SiN_x layer having the highest NH_3/SiH_4 amount which is sample “f”. In Table 3, the SiN_x layers will be used in the AIC poly-Si formation are given.

Table 3: SiN_x layers used in AIC poly-Si formation

Sample name	*NH_3 (sccm)*	*SiH_4 (sccm)*	*NH_3/SiH_4*	*Power (W)*
b	200	100	20	100
d	50	250	2	100
e	50	250	2	200
f	250	5	50	100

Since “a” and “b” have not very different refractive index only “b” was chosen. “f” has the highest amount of NH_3/SiH_4. “d” and “e” has the only difference in deposition power.

For this study only one type of AZO layer was deposited. The AZO layer was deposited by sputtering system. The AZO target, which contains 2 % Al, was used while Argon gas pressure was kept at 0.40 Pa during the sputtering process. Moreover, RF power and substrate temperature were 600 W and 150 °C, respectively, for AZO sputtering.

After the buffer layer formation, Al deposition (180 nm) was followed which was carried out using thermal evaporation method. During Al evaporation, the deposition rate was about 3 nm/s, and pressure was kept between $8x10^{-4}$ and $1x10^{-3}$ Pa. Prior to a-Si deposition the samples were exposed to ambient air in clean room conditions for 1 week to form native Aluminium oxide (AlO_x). As discussed before, AlO_x layer provides a controllable layer exchange of Al and Si. After the formation of AlO_x layer, 360 nm of a-Si was deposited by electron beam (e-beam) evaporation system manufactured by Vaksis Ltd. The deposition of a-Si was performed by evaporation of ultra pure (99.9999 %) silicon chunks. The processes were accomplished by 8.5 kV fixed e-beam voltage and 60-70 mA current emission. During the process the pressure was kept between 8×10^{-7} and 1.3×10^{-4} Pa while the deposition rate and substrate temperature were 10 Å/s and 200℃, respectively. E-beam system allows a good homogeneity of the layers thanks to rotating holder. The deposition systems have in-situ thickness measurement facility by quartz thickness monitor. In addition, for convenience, after deposition of Al and a-Si film, thicknesses of the films were measured with Dektak profiler. After a-Si deposition the samples were annealed in a classical tube furnace (PROTHERM Ltd.) at 500℃ for 5 h under nitrogen (N_2) flow to crystallize the a-Si by the layers exchange process, which forms the continuous polysilicon (poly-Si) thin films. The high resistances around the middle of the quartz tube provide a stable temperature profile through the furnace. Finally, the "glass/SiN_x/poly-Si/(Al+Si)" structure was obtained after thermal annealing. In order to characterize the resulting crystalline silicon layer, the residual Al+Si layer formed on top of the Si film should be removed. This residual layer was removed by mechanical polishing with colloidal silica to obtain smooth surface. The schematic of AIC poly-Si formation is shown in Figure 21.

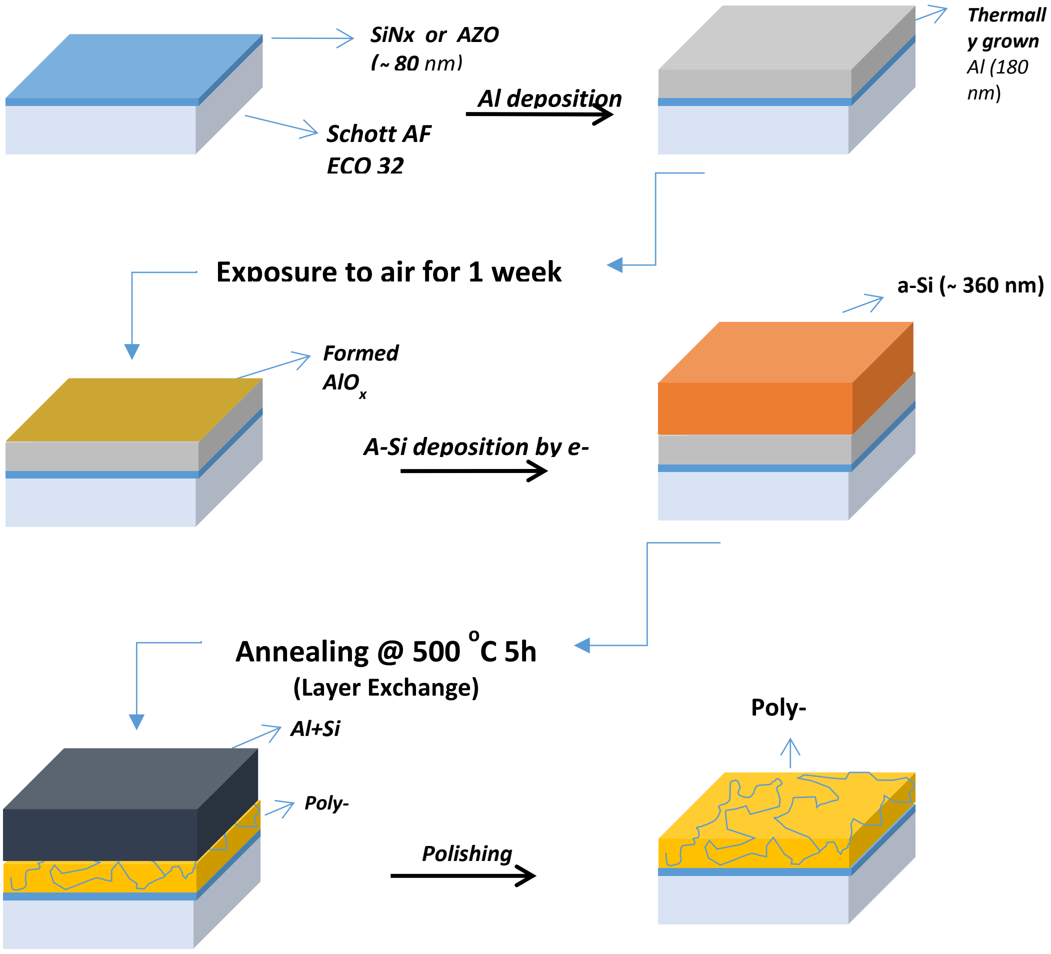

Figure 21: AIC poly-Si formation steps on SiN_x or AZO buffer layer

The crystallinity of the continuous AIC poly-Si layers were analysed by Raman spectroscopy which is Horiba 800 JobinYvon system supported with Olympus microanalysis system, which has a charge coupled device camera with a resolution of 1.0 cm^{-1}. Data acquisition of Raman spectroscopy was done by 632.8 nm wavelength He-Ne laser. The crystal orientations and crystallite size of the samples were analyzed by X-ray Diffraction (XRD) measurement. X-ray diffractometer was Rigaku Mini Flex with monochromatic CuKα 1 incident beam (λ=0.154056 nm) operated at 30 kV and 15 mA. XRD scanning was carried out between 10° and 90° 2θ values with a step of 0.02°. The grain size and crystalline orientation maps of poly-Si films were investigated by EBSD measurements. Quanta 400F Field Emission Scanning Electron Microscopy (SEM) was used for EBSD measurements. The surface of the selected SiNx layers were investigated by AFM with tapping mode on 10x10 μm^2 area. The accuracy of the orientation determination from the Kikuchi patterns is about 0.5°. The measured orientation imaging map has the size of 45×45 μm^2 for sample “d” and “f”. The orientation map was measured with a mapping step of 0.5 μm. The electrical properties were performed by four point probe system (Jandel RM3-AR) for sheet resistance analysis and Keithley 2400 sourcemeter for current-voltage (*I*-*V*) analysis.

3.2.2.2. Raman Results

Raman spectroscopy is a crucial technique for the characterization of poly-Si thin films which is also fast and sensitive method. The bond structure of silicon atoms can be monitored as a result of absorption and emission spectra by a laser beam. Accordingly, Raman spectroscopy is used for monitoring the crystal quality by giving information about bond peaks, full width at half maximum (FWHM), crystalline fraction and stress of the films. In this study, Raman spectroscopy was used to analyze the poly-Si film in terms of crystallinity and stress as a function of buffer layer content. The result of Raman measurements of poly-Si films grown on different buffer layer on glass substrate are shown in Figure 22.

Some of the results in AIC of a-Si are used by the permission of John Wiley and Sons Publishing with licence number of 3924720283855.

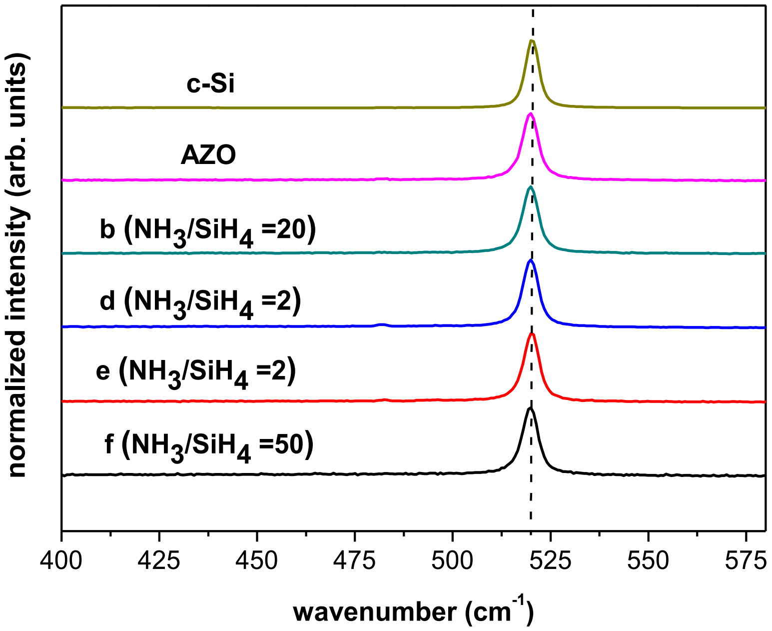

Figure 22: The Raman analysis of reference c-Si and poly-Si films produced by AIC technique on different SiNx and AZO coated glass

In Figure 22, also the Raman analysis of reference c-Si is given with AIC poly-Si films produced on AZO and different SiN_x coated glass. The spectra were normalized with respect to the LO/TO line of c-Si at 521 cm^{-1}. The Raman results in Figure 22 have very sharp and symmetric peaks at 521 cm^{-1}. The Raman peak at 480 cm^{-1}, which is the signature of a-Si, is not observed. Moreover, peak positions is close to that of c-Si (521 cm^{-1}), it means that all films with different buffer layer are under negligible stress.

Another indicator for the crystalline properties is the full width at half maximum (FWHM) which is found by calculating the Raman peak width which corresponds to the half of the peak intensity. FWHM values give information about the crystallization quality for poly-Si films. In this sense, the lowest FWHM value points the best crystallinity. In Table 4, the FWHM values of c-Si as a reference and the samples are given.

Table 4: FWHM values of the poly-Si layers and c-Si as a reference

Sample	***FWHM***
b	4.83
d	4.75
e	4.75
f	4.81
AZO	4.84
c-Si	4.16

As seen in Table 4, FWHM values of the samples are between 4.75 cm^{-1} and 4.84 cm^{-1} for different buffer layer used samples, which are not very far from the reference c-Si value (4.16 cm^{-1}). These results show that samples have high fraction of crystallinity. Every individual SiN_x based sample contains structurally different SiN_x layer due to different NH_3/SiH_4 fraction amount. There is a small difference between the samples in terms of FWHM values which indicates the crystallization. The difference of FWHM for poly-Si films compared by that of c-Si can be due to the grain boundaries of poly-Si films which contain high density of interface states. The presence of grain boundaries decreases the long range order of crystalline structure, which results in broadening of Raman peaks. Moreover, samples “d” and “e” with the same NH_3/SiH_4 ratio as 2 have very close FWHM values. Besides, samples “d” and “e” contain the lowest fraction of NH_3/SiH_4 in the SiN_x layer when compared by that of the other buffer layer content used poly-Si films. This can be due to the higher Si content in the buffer layer by using lower NH_3/SiH_4 ratio (=2). At the same time, the Raman analysis indicates that the AZO based sample has the FWHM value relatively close to the FWHM value of SiN_x based samples. However, the FWHM values do not indicate a notable difference in crystallinity. Raman results show that the crystallinity has no dependency on the buffer layer content and crystallization was achieved for all poly-Si films fabricated by AIC technique on glass substrates, which were coated by different buffer layer contents.

3.2.2.3. X-Ray Diffraction Measurements

Another analysis on AIC poly-Si films is X-Ray diffraction (XRD) measurement and the different orientations, crystallite sizes were examined by X-ray diffraction (XRD) measurement. In order to obtain the texture of poly-Si films, crystallographic orientation factors (Θ_{hkl}) were normalized with respect to different diffraction peak intensities obtained on a randomly oriented polysilicon powder which was taken as reference. The preferential orientation Θ_{hkl} (%) is defined for 3 spectral peaks by using [101,102]:

$$\Theta_{hkl} = 100\ x\ \frac{I_{hkl}/I_{0hkl}}{(\sum_{hkl} I_{hkl}/I_{0hkl})}\ (\%) \tag{16}$$

where $\mathrm{I_{hkl}}$ and $\mathrm{I_{0hkl}}$ indicate the diffracted intensities in the Θ-2Θ spectra of the poly-Si film and Si reference powder for each <hkl> orientation respectively. The XRD peak intensity for poly-Si was normalized by $[1\text{-exp}(-2\mu t/\sin\Theta)]$ to take the calculations through finite film thickness. In this normalization definition, μ, t and Θ are the X-ray absorption coefficient (143.1 cm^{-1}), film thickness and X-ray incident angle, respectively. The preferential orientation factor of poly-Si films, which was obtained after annealing at 500 ^{o}C for 5 hours and mechanical polishing, is given in Figure 23.

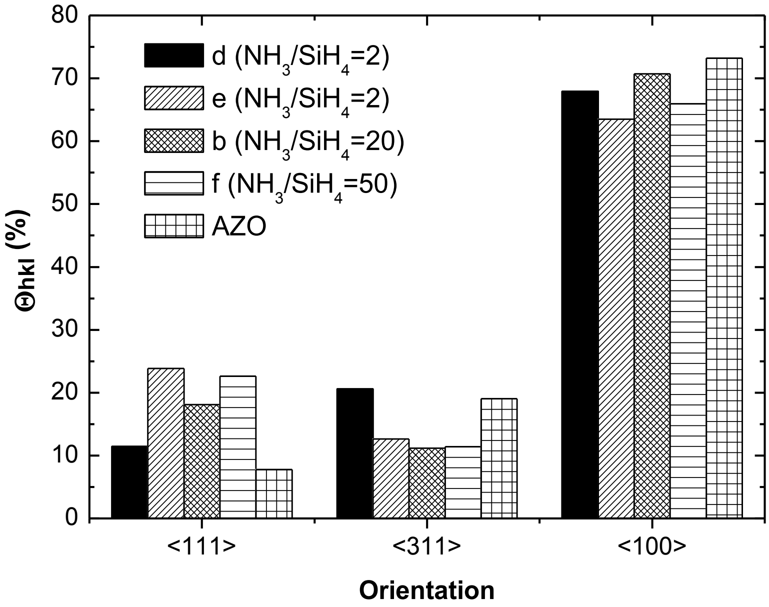

Figure 23: The calculated preferential orientation factor of poly-Si films by XRD measurements.

The normalization was applied for three peaks of <111>, From Figure 23, it is clear that the orientations of <111>, <100> and <311> are visible for all of the samples as independent of buffer layer content.

The crystalligraphic orientation calculations show that the orientation distributions of <111>, <311> and <100> have small differences for each sample fabricated by using different buffer layer content. It can be understood that the preferred orientation is <100> and it is found that 60-70 % of the surface indicates <100> orientation for all cases. It is possible to determine the crystallite size of poly-Si films by using X-ray diffraction analysis [103]. The average crystallite size of the samples can be calculated by using Scherrer’s equation [104]:

$$D = \frac{0.9\lambda}{\beta \cos\theta} \tag{17}$$

Here, D is the average crystallite size, λ (=1.54059 Å) is the wavelength of the used X-ray, β is the full width at half maximum (FWHM) value of the measured peak in radians and *Θ* is the diffraction angle. The calculated average crystallite sizes are given in Table 5.

Table 5: The average crystallite sizes of poly-Si samples calculated by Scherrer's equation

Sample	***Crystallite Size (nm)***
b	37.12
d	48.48
e	33.77
f	32.29
AZO	36.75

The results in Table 5 show that sample ”d” has the largest crystallite size which has the lowest fraction of NH_3/SiH_4 (=2) in SiN_x layer.

The crystallite size results shows that, among the SiN_x based samples, increase in the NH_3/SiH_4 fraction decreases the crystallite size, which means, increasing the SiH_4 content in SiN_x deposition creates larger crystallite size. Si clusters can be formed by The silicon atoms in SiN_x, and, since SiH_4 contains Si atoms, the amount of SiH_4 content can change the size of clusters. The increase of SiH_4 expands the silicon clusters and induces Si amorphous nanoparticles in SiN_x layer [105]. Nanoparticles can be induced by the further increase of SiH_4. When Si crystallites gets in touch with SiN_x layer during the layer exchange of Al and Si, the Si clusters and nanoparticles in SiN_x can promote the Si crystallization beside the AIC of amorphous silicon. Larger Si clusters and nanoparticles may form larger crystallite sizes. 48.48 nm of crystallite size, which is the largest one in Table 5, is achieved by sample “d” which contains the highest amount of SiH_4 during the SiN_x deposition as described in Table 3. On the other hand, although the sample “e” has the same amount of NH_3/SiH_4 in SiN_x layer as sample “d”, sample “e” has smaller crystallite size. This can be due to the difference of RF power values during PECVD deposition of SiN_x film for samples “d” and “e” as depicted in Table 3. Two times more RF power (200W) was used for the SiN_x

deposition of sample “e” while RF power is only 100W for the SiN_x deposition of sample “d”. Doubling the power changes the dissociation of SiH_4 and NH_3. At lower RF power Si-H bonds would be preferentially broken relative to the N-H bonds due to bond energies of 81kcal/mole and 120 kcal/mole for Si-H and N-H bonds, respectively [106]. This results in higher silicon content in SiN_x layer. For this reason, although sample “e” has the same NH_3/SiH_4 fraction like sample “d”, the crystallite size of silicon is affected by the RF deposition power of SiN_x. RF power increment decreases the Si content in the SiN_x layer which causes smaller Si clusters and nanoparticles size. Since the crystallinity of Si layer can be promoted by the silicon clusters and nanoparticles located on top of SiN_x layer, the smaller clusters and nanoparticles makes the Si crystallization weaker than that of larger clusters and nanoparticles. As a result the crystallite sizes of 48.48 nm and 33.77 nm are obtained for sample “d” and sample “e” respectively. Meanwhile, AZO based sample has the crystallite size as much as SiN_x based samples. The XRD results show that the buffer layer content has no effect on the preferred orientation of poly-Si films resulting <100> for all samples while the crystallite size shows differences depending on the content of buffer layer and the RF power of PECVD deposition system.

3.2.2.4. Grain Size and Surface Analysis

In order to see the effect of SiN_x surface roughness on poly-Si properties, the surface roughness of SiN_x coated glass was investigated by Atomic Force Microscopy (AFM). Especially, in thin film analysis the substrate surface roughness/texture has great impact on the film properties. It has been known that, a reduced surface roughness leads to less Si nucleation centers during the AIC of amorphous silicon process [107]. This finding is a significant result since the numbers of nucleation sites specify the average grain size of the film. To observe this statement, AFM analysis was performed for on SiN_x buffer layer deposited by “d” and “f” conditions which have the lowest and the highest NH_3/SiH_4 fraction, respectively. AFM images of these two samples are given in Figures 24a and 24b, respectively. It can be seen that, film formed on “d” condition used SiN_x has a smoother surface than that of

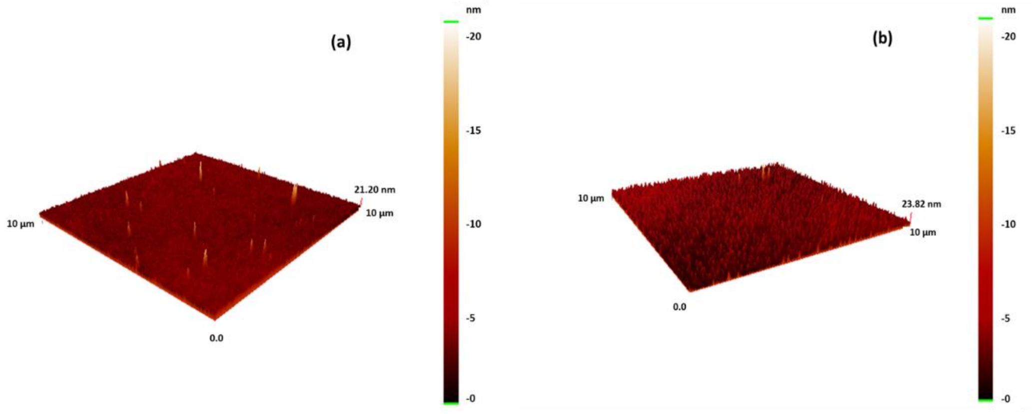

Figure 24: AFM images of poly-Si films on SiN_x buffer layer deposited by (a) “d” and (b) “f” conditions.

“f” condition used SiN_x film. The root mean square (RMS), which was deduced from AFM analysis of “d” condition used film is 0.74 nm while this is 1.32 for the poly-Si film on “e” condition used SiN_x. It can be concluded that rougher surface was obtained by using “f” condition for SiN_x deposition which has the highest NH_3/SiH_4 fraction when compared by lowest NH_3/SiH_4 fraction used SiN_x layer labelled as “d”.

Electron Back Scattering Diffraction (EBSD) analysis was performed on the final poly-Si layers. EBSD enables the crystalline mapping of surface by using the diffraction of backscattered electrons. The grain size has a significant role on the carrier transport in the poly-Si films and, therefore, the photovoltaic performances. Since sample “d” has the largest and sample “f” has the smallest crystallite size, the EBSD measurement was performed on these two samples. Also, as obtained from Raman analysis, sample “d” has the lowest FWHM and sample “f” has the largest FWHM value. In other words, the EBSD analysis of samples having the largest and smallest NH_3/SiH_4 fraction during the deposition of the SiN_x layers are compared. Figure 25 shows the crystalline orientation mapping image for sample “d” and sample “f” in which the investigated areas are $45 \times 45\ \mu m^2$ for the both samples.

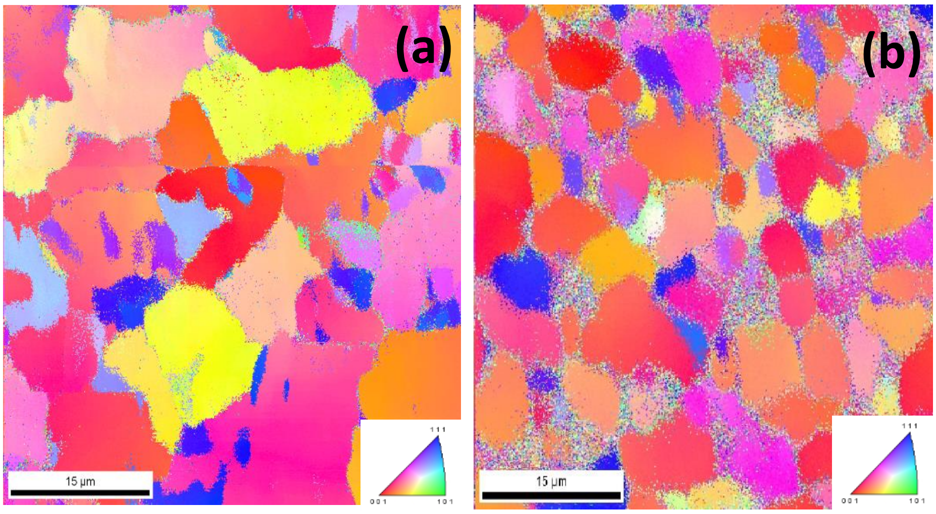

Figure 25: EBSD analysis of samples (a) “d” and (b) “f”.

The inverse pole figure on the right bottom of the EBSD maps give information about the grain orientations according to the colour. Graded red colour indicates silicon grains with an orientation that differs less than 15^o from the <100> parallel to the surface, while the blue and green colours correspond to an orientation deviation of less than 15^o from the <111> and <101>, respectively. EBSD surface mapping also enables understanding the grain size. In Figure 25, according to the pole figure, orientations around <100> seems to be dominant among the other orientations. Furthermore <111> orientation is very rare. XRD analysis showed that the preferred orientation is close to <100> and besides, the same result can be deduced by EBSD analysis. The average grain size up to 20-25 µm was achieved by using the "d" conditions to form the SiN_x buffer layer on glass substrate. However sample “f” has smaller average grain size. Since silicon is in contact with SiN_x layer the cluster structure in SiN_x has effect on the grain size as well as crystallite size. Sample “d” has the highest Si content (NH_3/SiH_4=2) whereas sample “f” has the smallest Si (NH_3/SiH_4=50) in SiN_x layer. The increased amount of Si content provides larger clusters instead of scattered and isolated Si atoms in SiN_x layer. As a result, the large Si grain sizes are achieved due to regular crystallization enhancement by large silicon clusters of SiN_x. Also, the roughness of the SiNx layers deduced by AFM measurement confirm the EBSD results. Crystallization on rough surface increases the number of possible nucleation sites compared to a smooth surface which leads to smaller grain sizes.

3.2.2.5. Electrical Analysis

Beside the structural analysis, electrical measurement was applied for the poly-Si films for the AZO based sample and SiN_x based samples of “d” and “f”. The resistivity analysis was done by four point probe (FPP) technique which is conventional, easy and non-destructive way of obtaining the resistivity of the films [108]. After measuring the sheet resistance of the samples the resistivity values were calculated in accordance with the corresponding poly-Si film thickness. In Table 6 the resistivity of the three samples are given.

Table 6: The sheet resistance and resistivity values of poly-Si films

Sample	$R_\square$ (kΩ/sqr)	ρ (Ωcm)
d	4.06	0.101
f	4.16	0.104
AZO	0.33	0.008

As discussed before, Al incorporation in AIC poly-Si films results in p-type doping with around 3×10^{18} cm^{-3} concentration [65]. The substitutional doping of silicon with aluminium creates shallow acceptor in silicon [109]. Table 6 shows that, SiN_x based samples have resistivity values around 0.1 Ωcm which states a low resistivity value when compared with commercial silicon wafers (1-10 Ωcm). On the other hand AZO based sample has a very low resistivity. The reason maybe the electrical measurement through the AZO layer since the poly-Si film is very thin with respect to the probe distances. It can be understood that, for the SiN_x based samples, different buffer layer content has no notable effect on the electrical properties of the poly-Si film.

Here, formation and characterization of poly-Si thin films, fabricated by Aluminium Induced Crystallization (AIC) of a-Si on different buffer layers was investigated. The poly-Si films were obtained by the layer exchange of Al and Si layers through AlO_x membrane after annealing at 500 °C for 5 h. The effects of buffer layers were studied in terms of structural and electrical quality. The Raman analysis showed that the fully crystallization was achieved for all samples independent of the buffer layer content. In the light of above investigations, stable poly-Si films were obtained both on AZO and SiN_x interlayers. However for the further AIC process SiN_x deposition with “d” conditions will be used as the buffer layer.

3.2.3. AIC Kinetics and Temperature studies

In this part, the AIC process is investigated comprehensively by additional tools like Secondary Ion Mass Spectroscopy (SIMS) and microscopy analysis. The influence of annealing temperature has been studied, both for nucleation and growth rate during AIC, and annealing temperatures between 400-550^{o}C are commonly practiced [110]. In addition to temperature, several parameters are known to effect the crystallization kinetics, including Al bulk oxygen content [111], thickness and structure of the AlO_x membrane at the Si/Al interface [112,113] and the Al grain structure [114]. Due to this wide range of parameters the specifics of the AIC process have shown variations among the different research groups’ works (an excellent discussion of which by Gall can be found in [110]). Here, study on the AIC kinetics of e-beam deposited a-Si films is reported as carried out in GÜNAM Laboratories. The influence of process parameters on the final poly-Si grain structure is also discussed.

3.2.3.1. Sample Preparation

The main stages of the AIC experiments are same as discussed before which is outlined in Figure 21. All of the a-Si/Al/SiN_x layer stacks used in this study were grown in the same respective deposition runs, in order to minimize any experimental variation. As the substrate, 1.1mm-thick Schott AF ECO 32 glass was used. This type of glass has a well matching thermal expansion coefficient (3.2 x 10-6 K^{-1}) to that of silicon (2.5 x

10^{-6} K^{-1}), low surface roughness (<1 nm RMS), and high luminous transmittance (83.2% at 1.1 mm with an optional 91.9% at 0.5 mm) that could be beneficial for potential superstrate configured for solar cell applications. Further, due to its relatively high transformation temperature (717^{o}C), it permits processing temperatures around 600^{o}C. Prior to deposition, the glass substrate was cleaned by a series of ultrasonic cleaning (acetone, isopropanol, DI water; 10 min. each) and a final 15 sec. dip in 10% HF solution. The substrates were then coated with 80nm thick silicon nitride (SiN_x:H) film with "d" conditions given in Sec.3.2.1, which served as a buffer layer against the diffusion of any possible contamination from the glass in the subsequent processing steps. Following the buffer layer deposition, a 180nm thick Al layer was deposited by thermal evaporation at processing pressures typically between 5 to 9 x 10^{-6} Torr at a rate of 3 nm/sec. The deposited Al film was then kept in atmosphere in clean room environment for one week in order to form a thin Al oxide layer on the surface. This layer is known to be beneficial in regulating the Si flux during the AIC layer exchange process [113]. After exposing the sample to air a 360nm thick Si layer was deposited using electron beam (e-beam) evaporation technique. The base pressure of the e-beam system was 1-2 x 10^{-7} Torr. The deposition rate was 1.5 nm/sec (as determined by quartz crystal microbalance), which was attained at 8.5 kV beam voltage and 60-70 mA emission current. The substrate temperature was kept at 200^{o}C. The samples were then annealed in a classical tube furnace (diameter: 10 cm, length: 190 cm) under N_2 flow (4 slm/min) in order to realize the AIC layer exchange process. In order to understand the thermodynamic mechanisms of the crystallization process four different annealing temperatures, 450, 475, 500 and 525°C were used. The crystal formation was monitored by optical microscopy (OM) through the glass side of the samples at incremental durations of annealing for each temperature. After layer exchange process the Al-Si mixture that is left on top layer was removed directly by mechanical polishing. The structural properties of the fully crystallized poly-Si samples were studied by a Horiba 800 Jobin Yvon Raman spectroscopy system. The Raman system has a charge coupled device camera providing a resolution of 1.0 cm^{-1}. Data acquisition of Raman spectroscopy was done by 532.8 nm wavelength He-Ne laser. Further information on the grain size and crystalline orientation of the poly-Si films were obtained using Electron Back Scattering Diffraction technique (EBSD), which was stationed in a Quanta 400F Field Emission Scanning Electron Microscope. The Al concentration in the final poly-Si layer was monitored by Secondary Ion Mass Spectroscopy (SIMS). For electrical characterization Hall effect measurements were carried out with ECOPIA HSM 3000 using four symmetric contact holders.

3.2.3.2. Microscopy Analysis

Optical microscopy (OM) offers a simple and effective way to monitor the crystal growth during AIC. When viewed through the glass substrate, the growing silicon clusters can easily be identified due to the contrast difference between Al and crystalline Si (Al appears much brighter than Si in reflection mode, and vice versa in transmission mode). The effect of annealing time and temperature on the evolution of poly-Si can thus be easily observed by viewing the Al-Si interface. In order to accomplish this, a series of rigorous annealing experiments were carried out. Four different annealing temperatures, 450, 475, 500 and 525 °C, were chosen to study the AIC process. All samples used in this study were taken from the same sample set, i.e., SiN_x, Al, and a-Si layers were deposited in the same runs to minimize any possible experimental variation. A typical optical micrograph taken from the Si/Al interface is given in Figure 26. The image was taken by reflecting the light through the glass substrate (sample was placed upside down onto the microscope glass). It is apparent from Figure 26 that the AIC process is partially completed under the conditions the sample was annealed at (2 hrs at 475^{o}C).

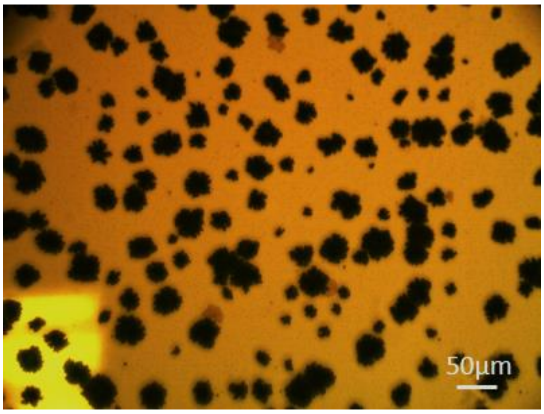

Figure 26: Optical micrograph taken from a-Si/Al/SiN$_x$/glass sample annealed at 475°C for 2 hrs. Image was taken in reflection mode through the glass substrate.

Three distinct features can be identified in the image; the first is the Al phase with relatively high reflectivity, appearing as the yellow background. Within the Al matrix poly-Si crystallites can be easily seen, as the process is well within its growth phase. A third type of feature that can be seen at a closer look are the small black dots that are widely spread within the Al matrix. These are the Si nuclei that were formed during the cooling of the sample. This phenomenon is explained in detail by Schneider et. al. [115]. At the end of the furnace run (prior to the cooling of the sample) the Si composition in the Al matrix (C_{Si}) is high enough to promote growth of the existing grains, but not sufficiently high to induce new nucleation processes. As the sample is cooled down the solid solubility of Si in Al diminishes, rendering C_{Si} to be high enough for nucleation to dominate. Further evidence for this model are the "depletion regions" that are formed around the large grains where the small nuclei are not observed (see Figures 27a and 27b). This is explained by C_{Si} next to the grains being very low due to the ongoing growth process. Based on the above consideration, the small precipitates were regarded as artefacts of the cooling process and were omitted from the crystallization percentage calculations discussed below. In Figure 27a the magnified OM image of the sample annealed at 475°C for 2.5 h and in Figure 27b the corresponding Scanning Electron Microscopy (SEM) image of one crystalline island are given. Unlike OM, SEM analysis cannot be carried out through the glass substrate; therefore the sample surface was mechanically polished prior to analysis.

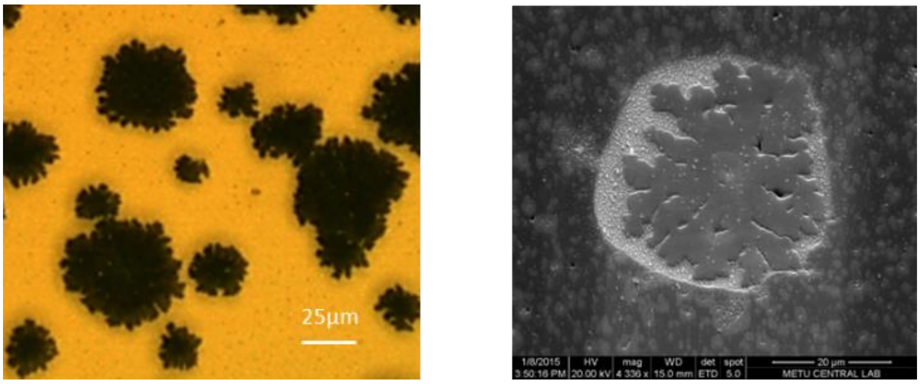

Figure 27: Micrographs taken from a-Si/Al/SiNx/glass sample annealed at 475°C for 2.5 h showing the formation of depletion regions, a) optical micrograph of large grains shown, a depletion region around them where no nuclei formation is present can be seen; b) scanning electron micrograph of a crystalline Si cluster where the sample was polished partially to expose the Si particle yet leave some of the surrounding Al-Si matrix. A high contrast region surrounding the Si grain is visible, indicating the Si-free (depletion) region

The crystallization experiments were done by carrying out annealing runs at incremental durations (approximately 10 runs) for each temperature. Selected optical micrographs showing the evolution of the Al/SiN_x interface for all temperatures are given in Figures 28 through 31.

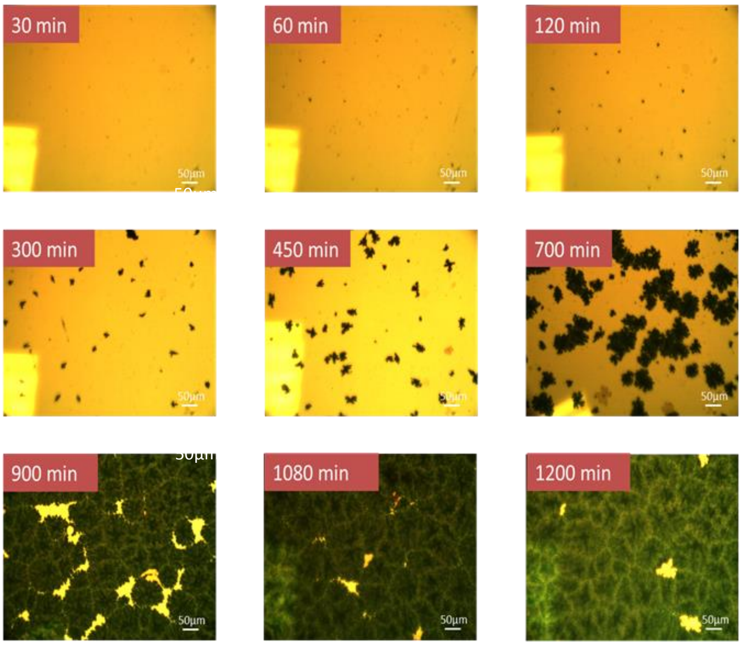

Figure 28: Optical micrographs taken from samples annealed at 450^{o}C at varying annealing times (given in the upper left corner inset for each micrograph).

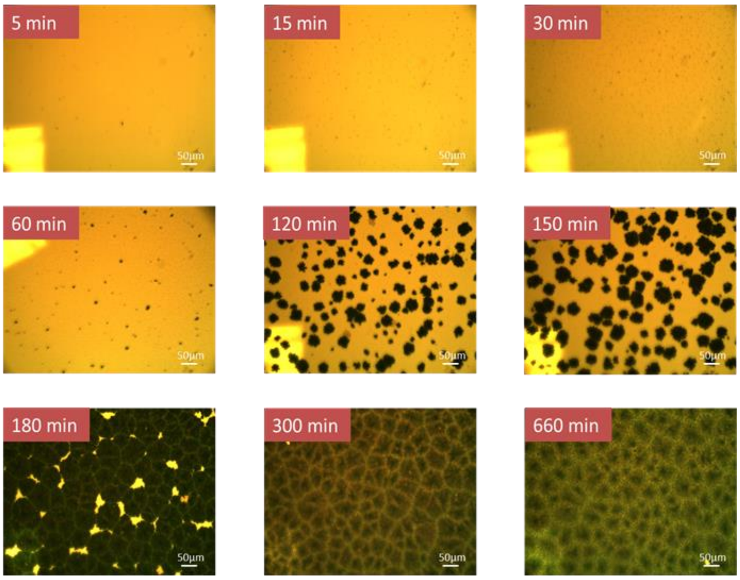

Figure 29: Optical micrographs taken from samples annealed at 475^{o}C at varying annealing times (given in the upper left corner inset for each micrograph).

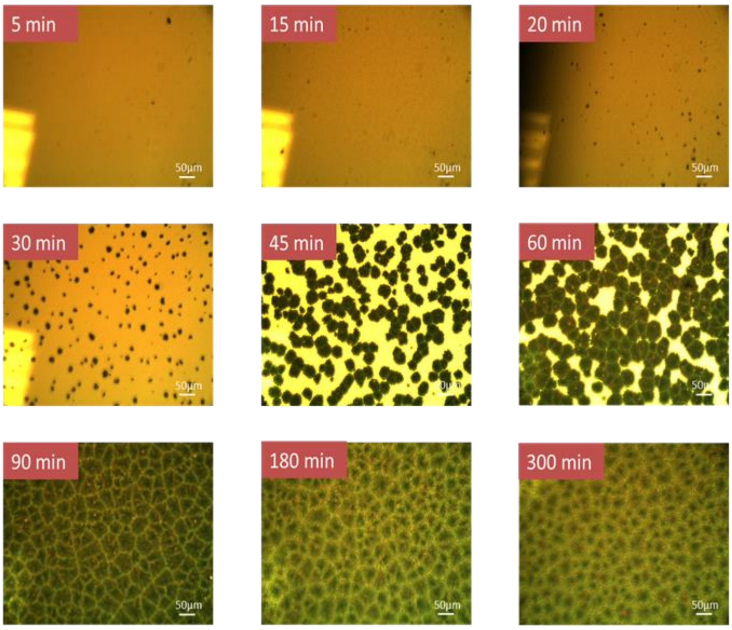

Figure 30: Optical micrographs taken from samples annealed at 500ºC at varying annealing times (given in the upper left corner inset for each micrograph).

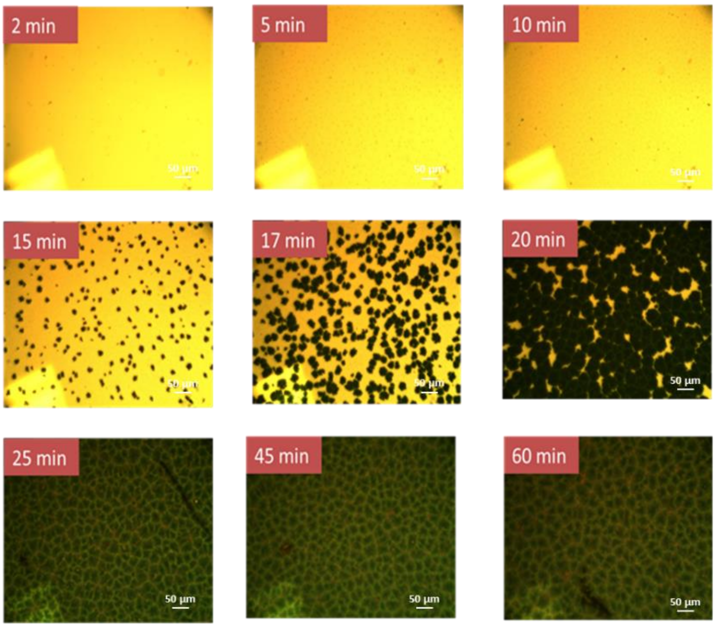

Figure 31: Optical micrographs taken from samples annealed at 525ºC at varying annealing times (given in the upper left corner inset for each micrograph).

It is apparent from Figures 28-31 that the rate of crystallization increases drastically with each temperature increment of 25°C. In other words, the full crystallization is reached earlier by increasing the temperature. Using the accumulated micrographs, the % crystallization for each annealing time and temperature combination was calculated with public domain image processing software ImageJ. The % crystallization vs annealing time curves are plotted as shown in Figure 32.

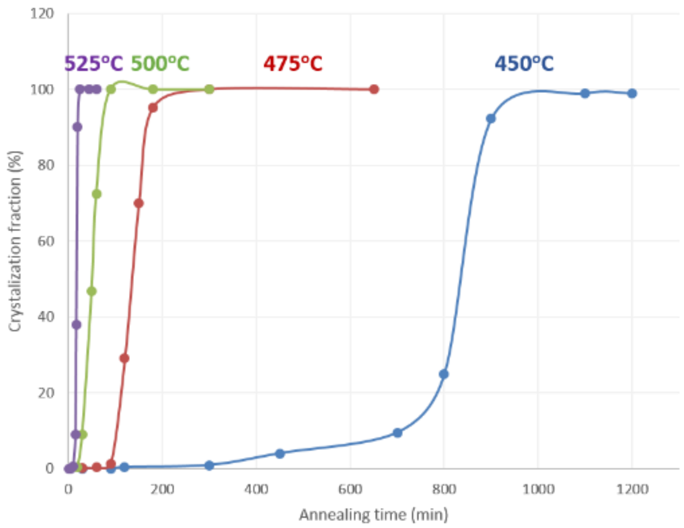

Figure 32: Percent crystallization vs annealing time curves for AIC experiments carried out at 450, 475, 500, and 525°C.

Typical "Avrami-type" crystallization behavior [116] can be seen for all temperatures, with an initial slow rate regime that is associated with nucleation, a near-linear intermediate region associated with the growth of the nuclei, and a saturation tail near the end of the crystallization process. Therefore an Arrhenius type relation between the growth rate and temperature can be inferred from Figure 32, which would enable the calculation of the activation energy of growth for the AIC process. The Arrhenius relation is given in Equation 18:

$$\boldsymbol{k = Ae^{-E_a/k_BT}} \tag{18}$$

Where k is the rate constant (% crystallization/min.) obtained by line fitting the intermediate (growth) region of the Avrami curves for each temperature, A is the pre-exponential factor, E_a is the activation energy for growth (eV), k_B is the Boltzmann constant (8.617 x 10^{-5} eV/K), and T is the annealing temperature in K. The expression can then rearranged in the form of Equation 19:

$$\boldsymbol{ln}(\boldsymbol{k}) = \frac{\boldsymbol{-E_a}}{\boldsymbol{k_B T}} + \boldsymbol{ln}(\boldsymbol{A}) \tag{19}$$

The equation above can be written in y = ax + b form to represent a line. Accordingly, the ln(k) vs $1/k_BT$ shown in Figure 33 would have a slope equal to – E_a. Based on this consideration, our experiments revealed that the activation energy for growth during the AIC process was about 1.93 eV, which is well in accord with the 1.8 eV reported in Gall et. al. [86] and 1.9 eV by Schneider et., al. [112]

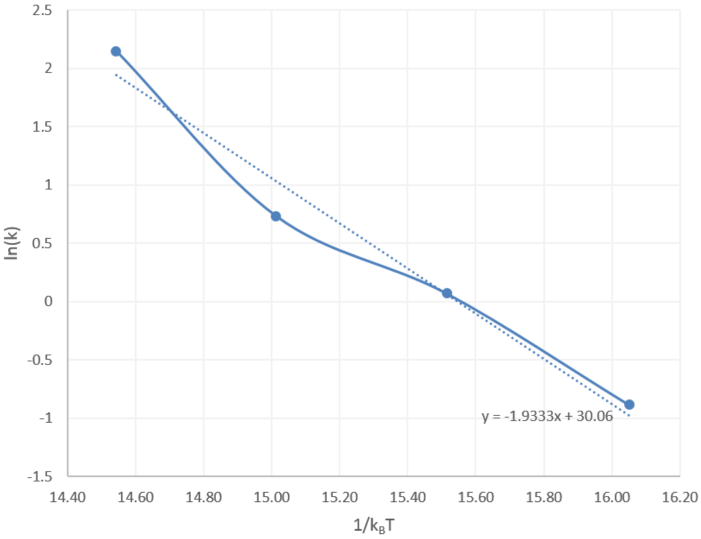

Figure 33: ln(k) vs. $1/k_BT$ graph plotted using the data given in Figure 32. The activation energy calculated from the graph corresponds to 1.93 eV.

The effect of annealing temperature on the final grain size was investigated through OM images and EBSD maps. It is important to note that each of the Si "grains" seen in the optical micrographs given above do not necessarily constitute of a single crystal. EBSD mapping of a partially crystallized AIC sample (obtained by incomplete annealing) is given in Figure 34. As apparent from the color distribution the grains can be of single crystalline as well as poly-crystalline nature. Nevertheless, the size distribution of these poly/single crystal grains provide an effective way of qualitatively comparing the final crystal structure, particularly when coupled with EBSD analysis.

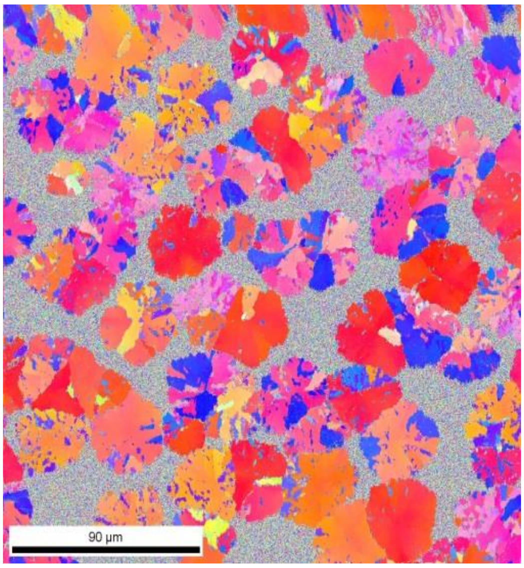

Figure 34: EBSD images taken from partially crystallized samples annealed at 500°C. The grainy (predominantly grey colored) background is Al, whereas the solid colored features are the Si grains. Some of the features consist of only one color (single crystal), while others have multiple colors (multi-crystalline).

The optical images of the fully crystallized samples that were annealed at varying temperatures are given in Figure 35a through 35d. A near steady decrease in the grain size with increasing annealing temperature can be easily observed. In order to acquire a quasi-quantitative comparison of the grain size distribution, the areas of each grain in the given micrographs were measured using ImageJ (since the thickness of the Si film, ~0.2 µm, was significantly smaller than the apparent grain size, an area measurement was found to be sufficient to calculate the grain size). The approximated grain size for each measured area was then obtained by assuming a circular shape and calculating the corresponding diameter. The grain size distribution histograms for each temperature are given in Figure 35e through 35h. The histogram plotted for the sample annealed at 450°C (Figure 35e) shows the highest deviation from a standard Gaussian distribution, possibly related to the high error margin of areal measurement due to the small number of total grains seen in the micrograph. As the grain size reduces (i.e. the number of grains visible in a micrograph increases) the shapes of the histograms appear to better match the Gaussian distribution. Furthermore, the tightest grain size distribution is seen for the sample annealed at 525°C (Figure 35h), which has the smallest average size. This can be seen more clearly in Figure 36, where the average and the standard deviation of the approximated grain sizes at each temperature is plotted.

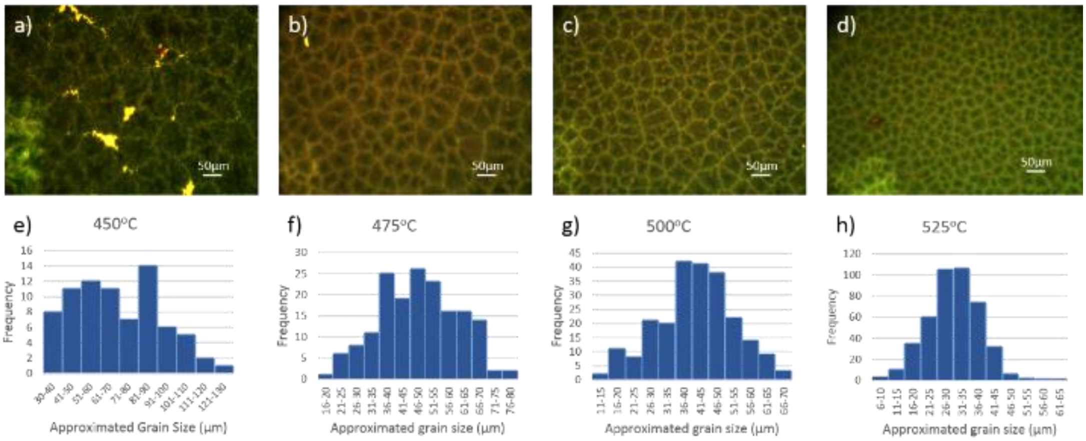

Figure 35: Effect of annealing temperature on poly-Si grain size: optical micrographs taken from fully crystallized samples annealed between 450 and 525°C (a through d), distribution of approximated grain size for fully crystallized samples annealed between 450 and 525 °C (e through h)

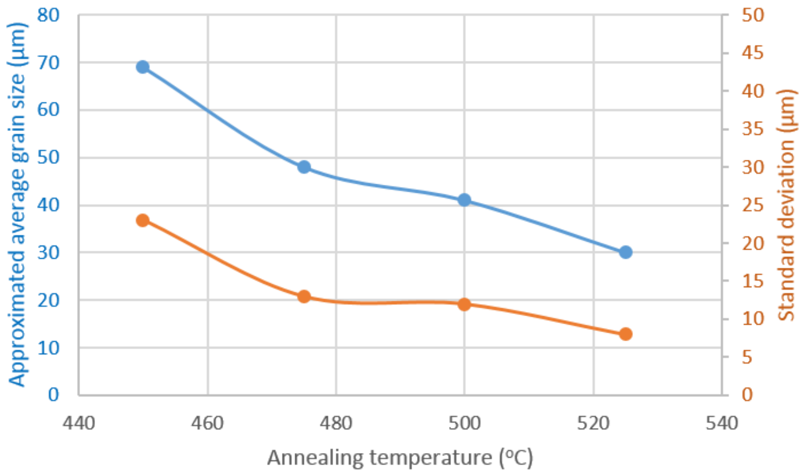

Figure 36: Annealing temperature vs. approximated average grain size and standard deviation. The referred grains do not necessarily represent a single crystal.

In order to verify the observation above, electron backscatter diffraction (EBSD) maps were taken from fully crystallized samples annealed at 450ºC and 525ºC (Figures 37a and 37b, respectively). EBSD images in Figure 37 are indeed in correlation with OM images. Increasing the annealing temperature decreases the grain size. The sample annealed at 450 ºC has grain size as much as 50 µm, however the sample annealed at 525 ºC shows distinctly smaller grains. EBSD analysis also provides information about the orientation of grains. In both cases the orientation of the grains appears to be close to (100) and (111), and a distinctly preferential orientation is not apparent in either case. This observation does not agree with Ref [121], which states that lower annealing temperatures result in preferred grain orientations of (100). One possible influence to consider for explaining this discrepancy is the presence of the SiN_x buffer layer in this study, which was not the case in Ref [117]. However, as the said study explains, the nucleation process is initiated at the a-Si/Al interface, far away from the SiN_x layer. In as much as the grain orientation is chiefly determined during nucleation, the SiN_x layer is not expected to have a significant effect on the preferred orientation of the final poly-Si layer.

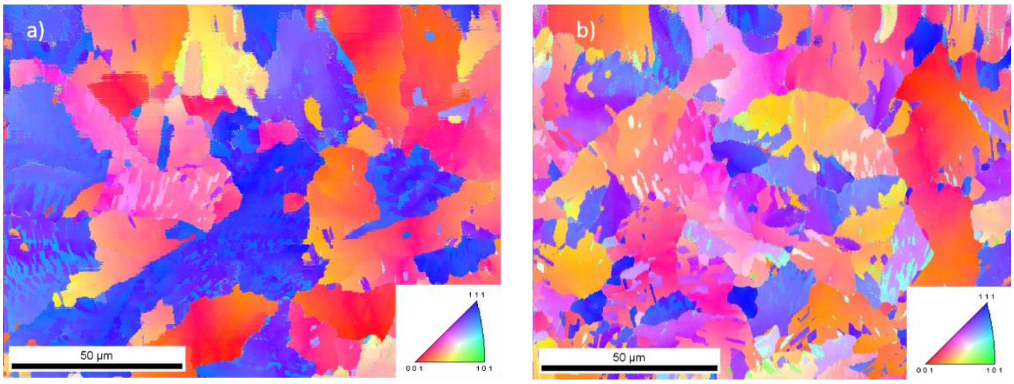

Figure 37: EBSD images taken from fully crystallized samples annealed at a) 450ºC and b) 525ºC. The colors represents the orientation of grains according to the color code given in the lower right corner inset.

3.2.3.3. Raman Analysis

The structural quality of the fully crystallized samples annealed at different temperatures were examined by using Raman spectroscopy. Figure 38a shows a wide wavenumber range scan while Figure 38b shows the same spectra focused around crystalline silicon (c-Si) peak at 520 cm^{-1}. A c-Si peak obtained from a single crystal wafer at the time of the measurements is also added to the graph as reference. From the wide range scans (Figure 38a) all spectra show a sharp c-Si peak comparable to that of the single crystal sample. At a closer look (Figure 38b), a slight increase in width towards lower wavenumbers with increasing annealing temperature is visible. This is believed to be related to the grain boundaries, which result in a small, amorphous-like contribution to the spectra. Lower annealing temperatures promote higher grain sizes, which result in less grain boundary area, therefore, the Raman spectra appears closer to that of the Si wafer. Nevertheless, the structural quality of samples annealed at 475 and 500^{o}C appear to be similar to the sample annealed at 450^{o}C.

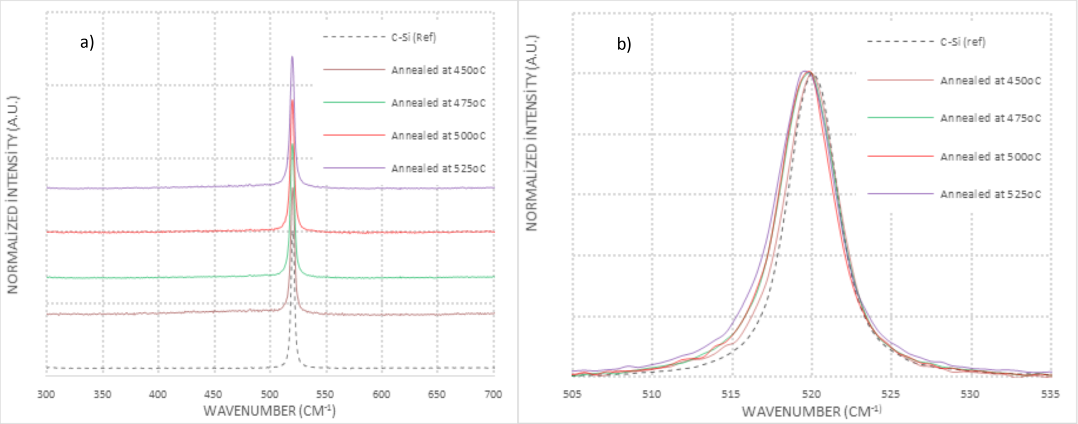

Figure 38: Raman spectroscopy taken from fully crystallized samples annealed at varying temperatures: a) wide wavenumber range, b) near c-Si peak (background subtracted).

3.2.3.4. Secondary Ion Mass Spectroscopy Analysis (SIMS)

The incorporation of aluminum in the final poly-Si film after the AIC process is well known [65]. The Al atoms dope silicon within the solubility limits. Therefore, the doping characterization of the Al profile was of interest. A key tool for this purpose is secondary ion mass spectroscopy (SIMS). The SIMS depth profile taken from an AIC sample annealed at 500^{o}C is given in Figure 39. From the SIMS profile, the Al appears to be distributed along the thickness of the Si layer homogenously, with a concentration of approximately 9x10^{19} cm^{-3}. The 30 nm Al plateau near the surface suggests that the aluminium layer was not polished off completely from the poly-Si surface. To measure the Al that is electrically active in the poly-Si layer Hall effect measurement was carried out, which revealed an active (p-type) carrier concentration of 1.2x10^{18} cm^{-3}. This result is consistent values reported in literature [65]. These findings suggest that only a small fraction (approximately 1%) of the residual Al is electrically active after AIC. The SIMS analysis was done by Evans Analytical Group (EAG) in USA.

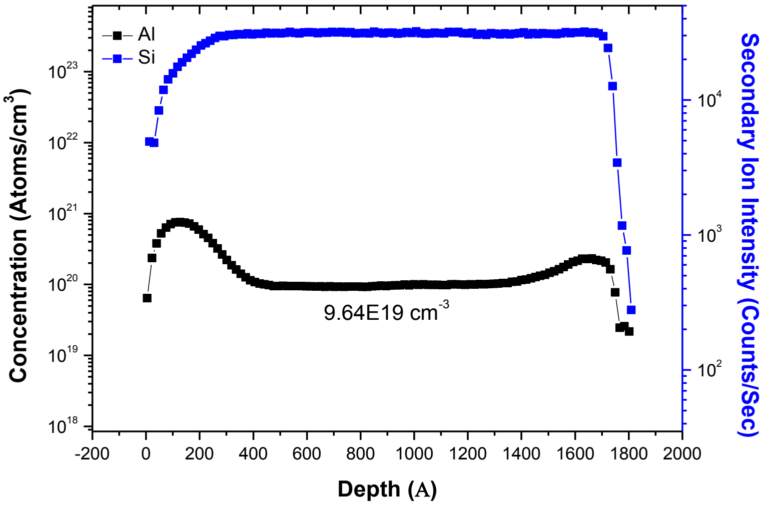

Figure 39: SIMS profile of standard AIC poly-Si film

AIC experiments carried out in GÜNAM laboratories revealed that crystallization of e-beam deposited amorphous silicon films can be realized effectively at temperatures as low as 450°C, resulting in poly-Si films with grain sizes of tens of micrometers. Activation energy associated with the growth of Si crystallites was determined as 1.93 eV, which correlates well with previous studies. Raman spectroscopy on the final AIC poly-Si layers shows a slight increase in C-Si peak (near 520 cm^{-1}) with increasing annealing time, which is likely related to the increase in grain boundary fraction of the films. The residual Al that is left in the final poly-Si layer is around 9x10^{19} cm^{-3}, as measured by SIMS. However Hall effect measurements show that the active Al is approximately two orders of magnitude smaller than the total Al.

3.2.3.5. Transmission Electron Microscopy (TEM)

TEM is an alternative way of microscopy for detailed imaging analysis. In TEM technique, a beam of electrons is transmitted through a thin specimen. The image is provided by interaction of the electrons with the sample. In this manner, the standard AIC poly-Si sample was prepared for TEM analysis. The TEM images of the poly-Si sample is shown in Figure 40.

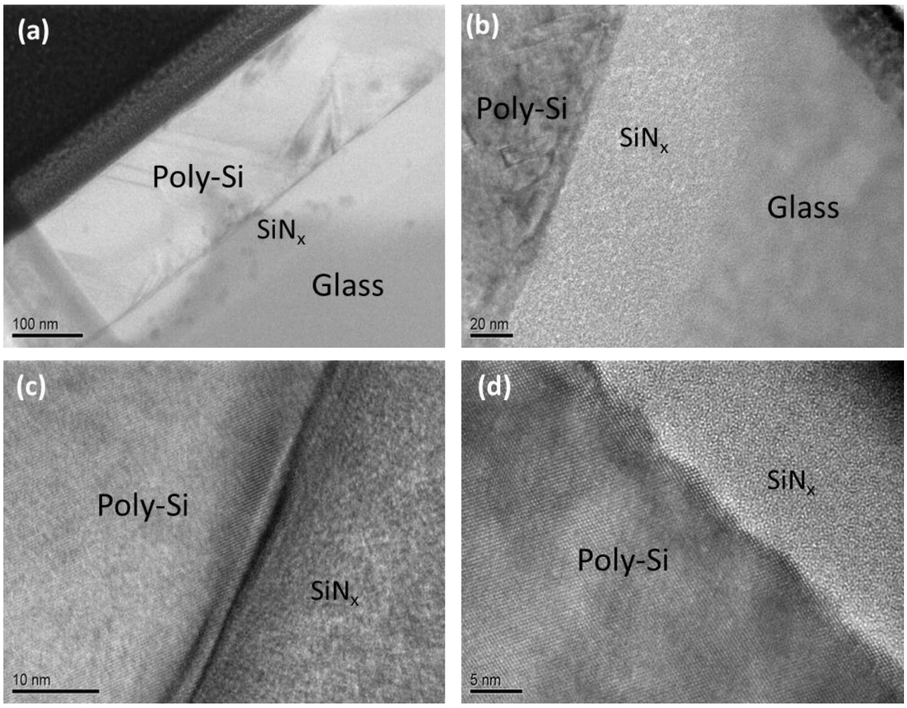

Figure 40: TEM images of standard AIC poly-Si film

TEM images were taken with different resolutions. In Figure 40a, the full stack can be clearly seen with the individual layers of 180-200 nm poly-Si, 80 nm SiN_x and the glass substrate. Besides some boundaries or defective regions are visible in poly-Si layer. When the magnification is increased, in Figure 40d, the atomic array of Si structure is also seen, especially close to the poly-Si/SiN_x interface. TEM images indicate that a good quality of AIC poly-Si film has been established.

3.2.4. AIO$_x$ Membrane Studies

Additional experiments were carried out to examine the effect of AlO_x membrane on the AIC process. For this purpose, three samples of SiN_x/glass (from the same batch) were Al coated (180 nm) by thermal evaporation. The first sample was directly taken to the clean room and inserted to the e-beam evaporation system which was pumped down immediately and kept under high vacuum (~10^{-7}Torr level), corresponding to an atmospheric air exposure of about 10 min. The second and third samples were kept in the clean room under atmospheric pressure prior to their insertion into the e-beam system for 24 h and 1 week, respectively. All samples were then coated with 360 nm thick a-Si layer using standard deposition parameters. Each sample was then cut into 4 pieces and were annealed at 500^{o}C for durations of 30, 60, 180 and 300 minutes. The optical micrographs obtained from the samples at various stages of annealing are given in Figure 41. As seen, the AIC process was the fastest in the sample with the Al layer that was exposed to atmosphere for the shortest duration. This was an expected outcome, in as much as the Si-flux limiting AlO_x layer has the smallest thickness for this sample. There was, however, little difference between the crystallization behaviours for samples with Al layers exposed to atmosphere for 24 h and 1 week. This could be indicative of the fact that the majority of the Al oxidation occurs within the first day of exposure, and further exposure has little effect on the AlO_x membrane formation.

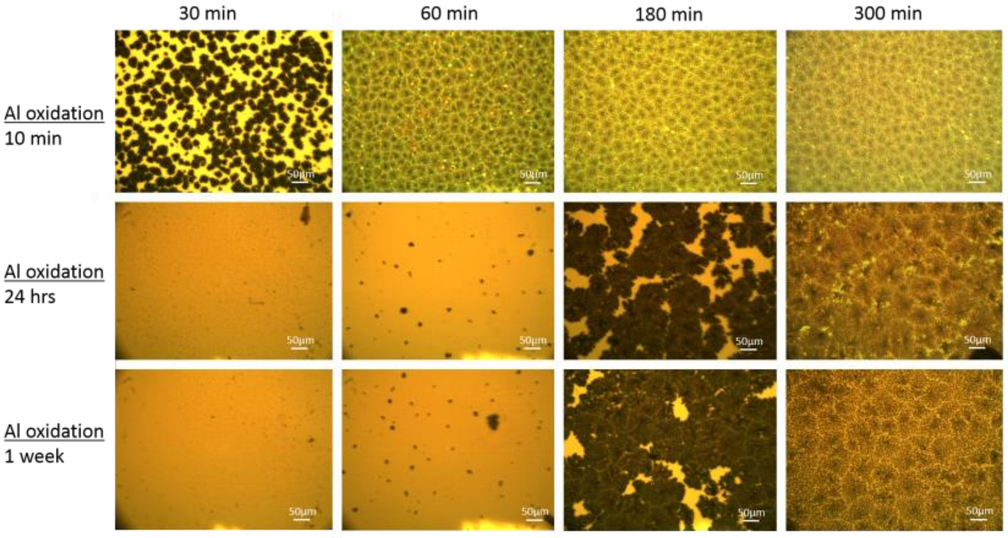

Figure 41: Optical micrographs taken at various durations of annealing at 500^{o}C of AIC samples with different Al-oxidation conditions.

3.2.5. Defect Etching of AIC poly-Si layers

A common method to investigate the grain boundaries and defects is the use of etching solution. In addition, the grain quality of the films can be explored. The etching solution preferentially etches the defects and grains. The etching process for materials like Si, SiGe or Ge, requires an oxidizing agent and a fluoride component which dissolves the oxidized material. Generally the oxidizing agents are nitric acid (HNO_3), peroxide hydrogen (H_2O_2), and chromate in the form of hexavalent chromium (CrO_3, $K_2Cr_2O_7$) [118]. Some solutions require a dissolving agent in order to dilute the solution and provide a control on the etching rates. The ratio between the different components determines the mechanism of the reaction. Whatever the type of etchants used, defects selective etching requires a modification of the surface potential between the perfect crystalline materials and defects. Chromium-based etching solutions, such as Sirtl, Secco, Wright or Schimmel techniques have been known for defects indication in crystalline materials [119].The etching mechanism for Cr^{6+}- containing etching solutions is not well-known. A strong adsorption of chromates on the Si surface via silanol groups is expected, resulting in the formation of Si-O-Cr-(O_2)-O-Cr(O_2)-OH [120]. It is important that the density and arrangement of any surface dislocations can be determined. Schimmel etchants are used to reveal the presence of surface threading dislocations [121]. Here, Schimmel etching technique was used to reveal out the defects and to see the effect of solution with different concentrations. CrO_3, HF and H_2O solution was prepared for etching. Three different solutions with different concentrations were prepared as seen in Table 7 and in Table 8 etching time with respect to the solution type and sample is given.

Table 7: Different concentrations of CrO_3 - HF - H_2Osolution

	CrO_3 (cc)	HF (cc)	H_2O (cc)
Sol A	20	20	15
Sol B	20	20	100
Sol C	20	20	2000

Table 8: Etching time with respect to the solution type and sample

Sample	Solution used	Sample type	Etching time (s)
1	Sol A	AIC	1
2	Sol A	SPC	1
3	Sol B	AIC	1
4	Sol B	AIC	4
5	Sol B	AIC	10
6	Sol C	AIC	1
7	Sol C	AIC	10
8	Sol C	AIC	30

After etching, samples were analysed by SEM. The SEM images are given in Figure 42 where the sample numbers are written on the pictures.

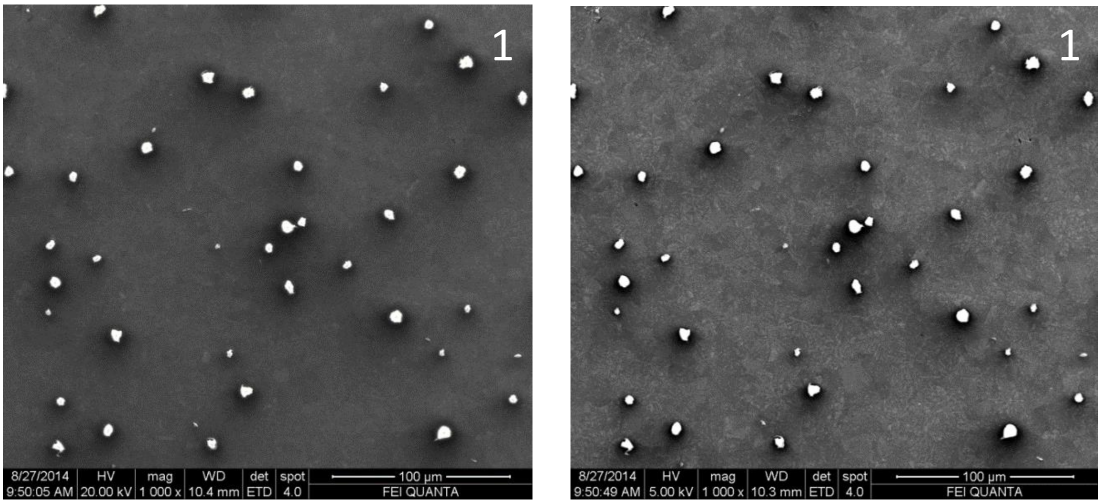

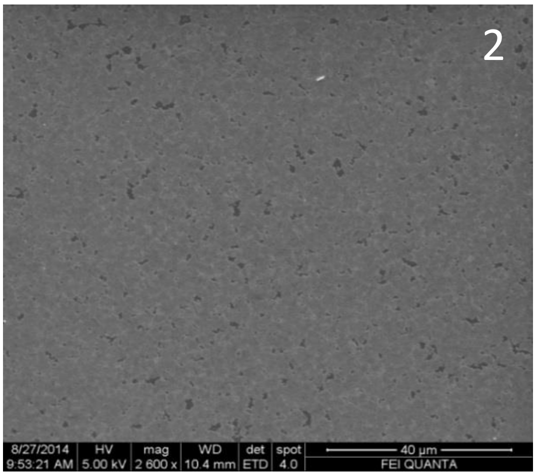
2
8/27/2014 | HV | mag | WD | det | spot | 40 µm
9:53:21 AM | 5.00 kV | 2 600 x | 10.4 mm | ETD | 4.0 | FEI QUANTA

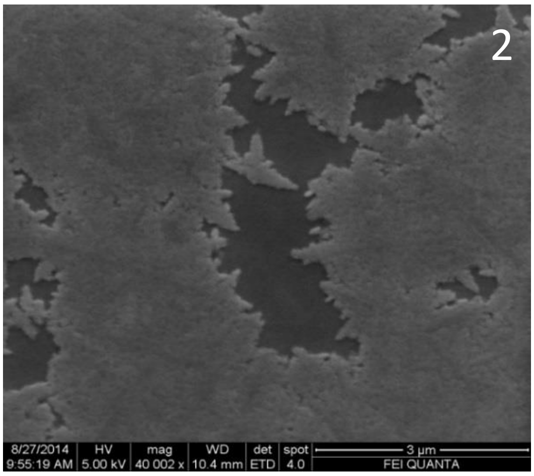
2
8/27/2014 | HV | mag | WD | det | spot | 3 µm
9:55:19 AM | 5.00 kV | 40 002 x | 10.4 mm | ETD | 4.0 | FEI QUANTA

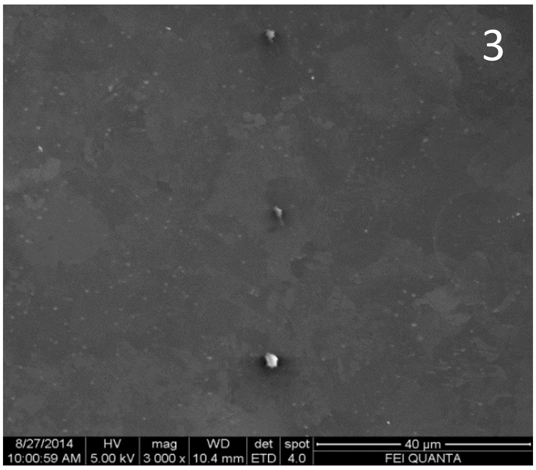
3
8/27/2014 | HV | mag | WD | det | spot | 40 µm
10:00:59 AM | 5.00 kV | 3 000 x | 10.4 mm | ETD | 4.0 | FEI QUANTA

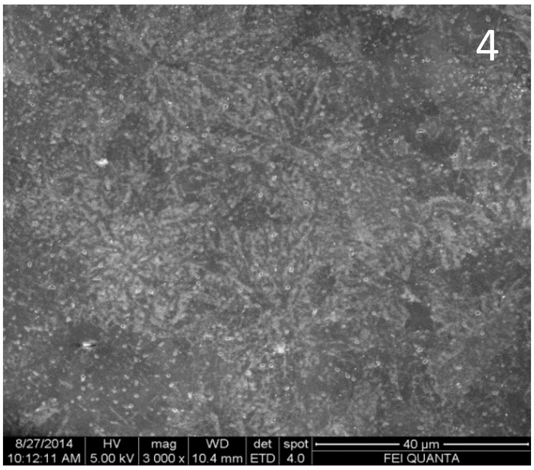
4
8/27/2014 | HV | mag | WD | det | spot | 40 µm
10:12:11 AM | 5.00 kV | 3 000 x | 10.4 mm | ETD | 4.0 | FEI QUANTA

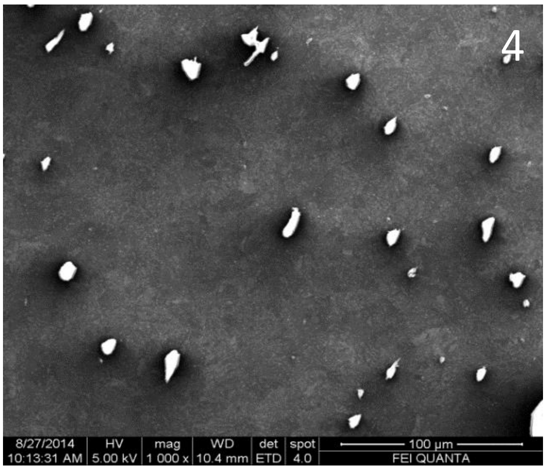
4
8/27/2014 | HV | mag | WD | det | spot | 100 µm
10:13:31 AM | 5.00 kV | 1 000 x | 10.4 mm | ETD | 4.0 | FEI QUANTA

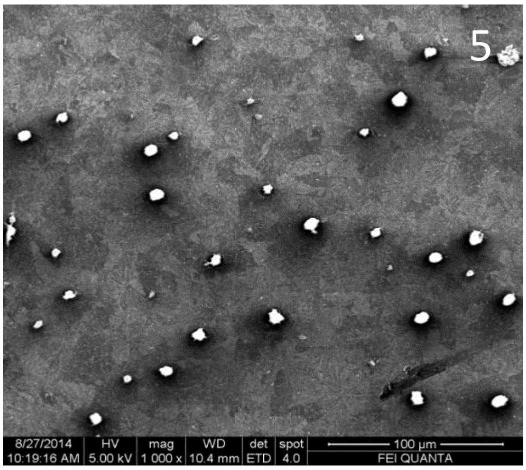
5
8/27/2014 | HV | mag | WD | det | spot | 100 µm
10:19:16 AM | 5.00 kV | 1 000 x | 10.4 mm | ETD | 4.0 | FEI QUANTA

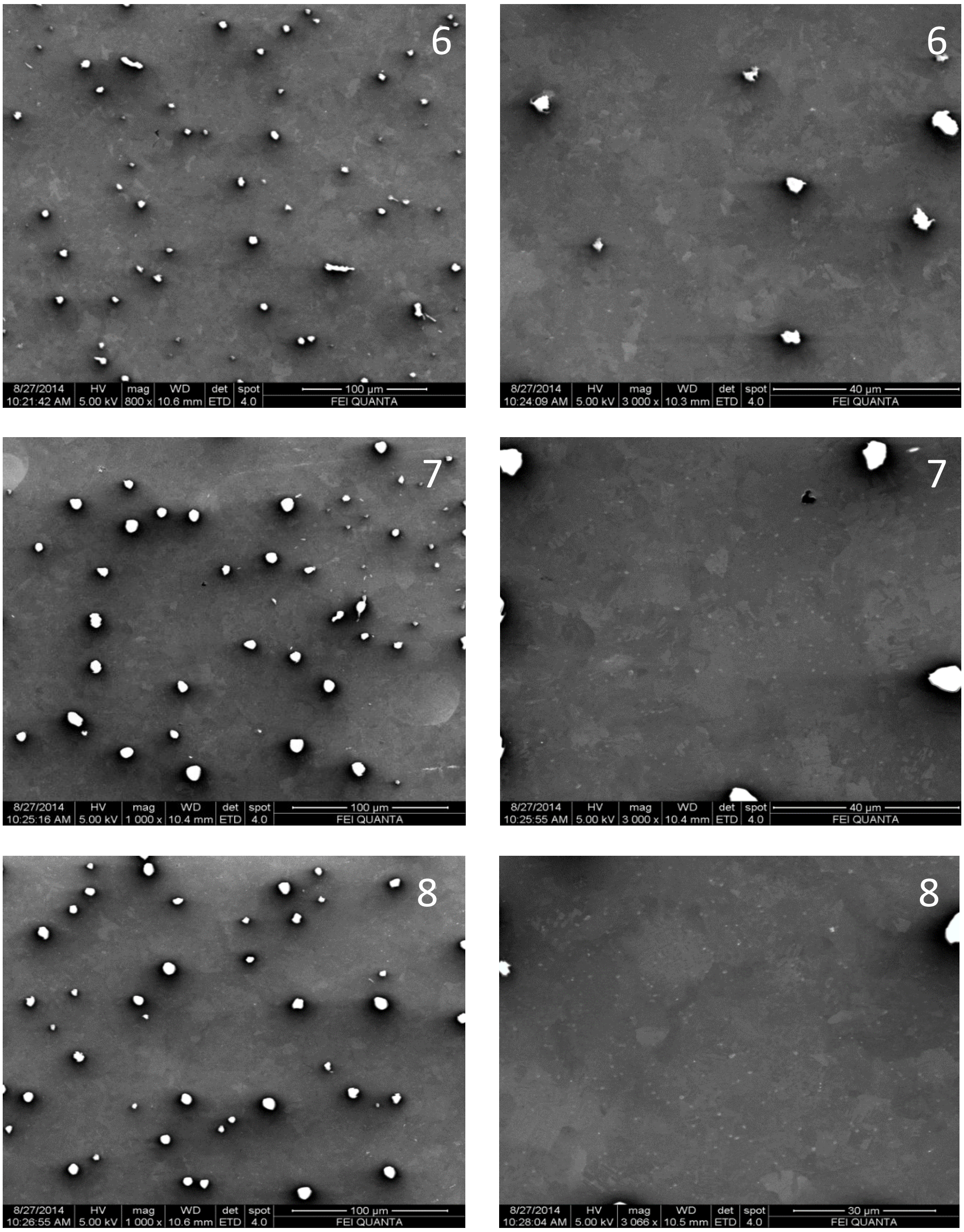

Figure 42: SEM images of Schimmel etched AIC and SPC samples

The white dots seen on the images are charged regions occurred due to pinholes. Solution A is used for the comparison of AIC and SPC samples. The grains are clearly seen on AIC sample however SPC sample has no indication for grain structure. The surface has some island structures. After the solution is diluted, in other words converted into solution B, the grains of AIC sample becomes more apparent as the etching time is applied as 1 s, 4 s and finally 10 s. When the solution is diluted further, as solution C, even up to 30 s of etching the surface shows no difference with respect to 1 s of etching. Here the Schimmel etching most clearly shows the grains at sample 5 which is etched with solution B for 10 s. However the desired boundary etching is not achieved in this etching study. After Schimmel etching another chemical etching technique was tried on AIC sample. The solution was prepared by HNO_3:HF (100:1). The advantage of using this solution is its' simple preparation. AIC samples were etched for 5,10 and 30 seconds. In Figure 43, the SEM images of this etching study is given.

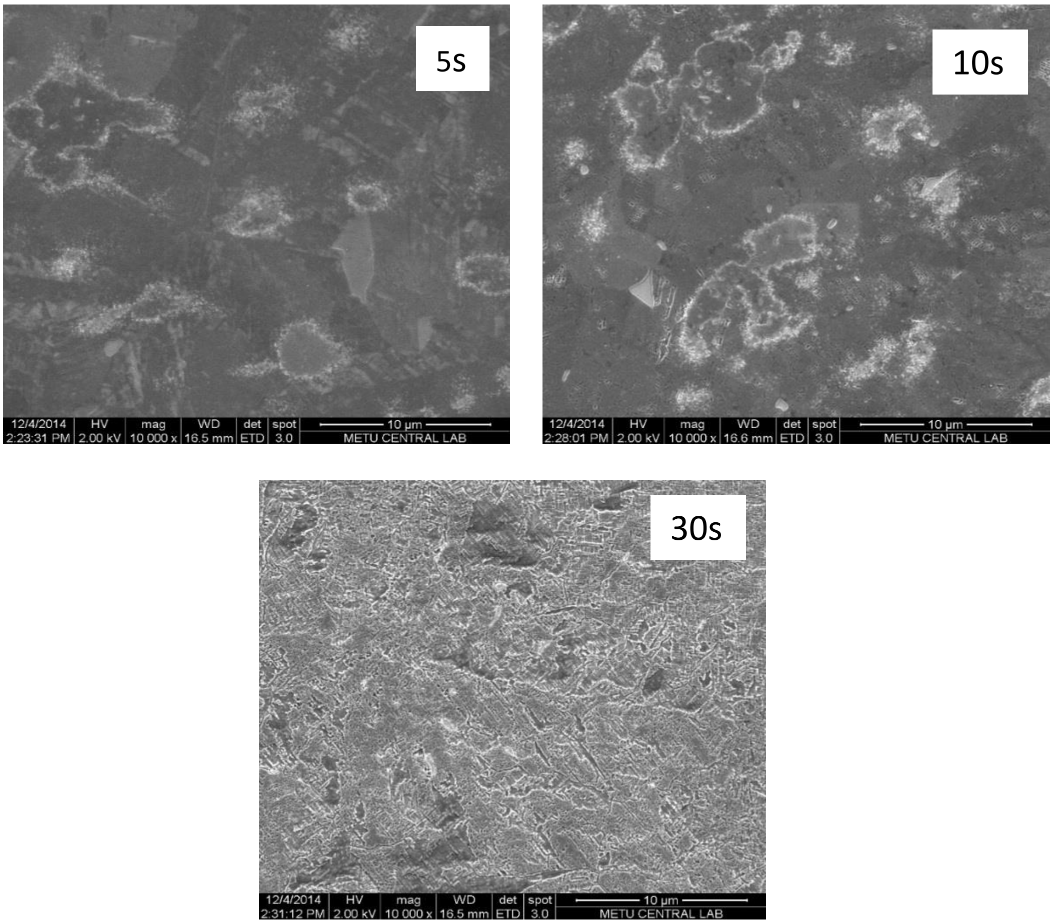

Figure 43: SEM images of HNO_3:HF solution etching

As it is clear in the Figure 43, 30 seconds etching destroys the surface too much. When 5 s and 10 s etchings are compared this technique seems to be more efficient for grain boundary etching. Because the etching is clear around the grains. This method may be more promising for surface defect analysis among the other etching techniques.

3.3. Solid Phase Epitaxy (EPS) Experiments

Absorber growth experiments on the AIC seed layers were also carried out and three samples of the stacked a-Si/Al/SiN_x/glass layers were produced. Like in the previous section, the samples were furnace annealed at 450, 500, and 525^{o}C, respectively, to form fully crystallized poly-Si structures before the Al-Si top layer was removed by polishing (crystallinity was confirmed by Raman spectroscopy, which yielded identical spectra to that given in Figure 38 for each corresponding annealing temperature). The samples were then dipped in 10% HF solution to ensure the surfaces were completely hydrophobic (i.e., no native oxide was present), and were inserted in the e-beam deposition chamber for growth of 1 μm thick a-Si absorber layers. Deposition was carried out at 8.5 kV beam voltage and 100 mA emission current, resulting in a deposition rate of 2 nm/sec. The samples were then annealed at 600^{o}C in N_2 atmosphere in incremental steps in order to induce solid phase epitaxy of the a-Si layers. Raman spectroscopy measurements were carried out on all samples before and after each annealing step, as plotted in Figure 44. In all cases, a gradual crystallization process is observable with increased annealing time, which is expected as the epitaxial growth would begin at the seed/absorber interface and continue towards the absorber surface.

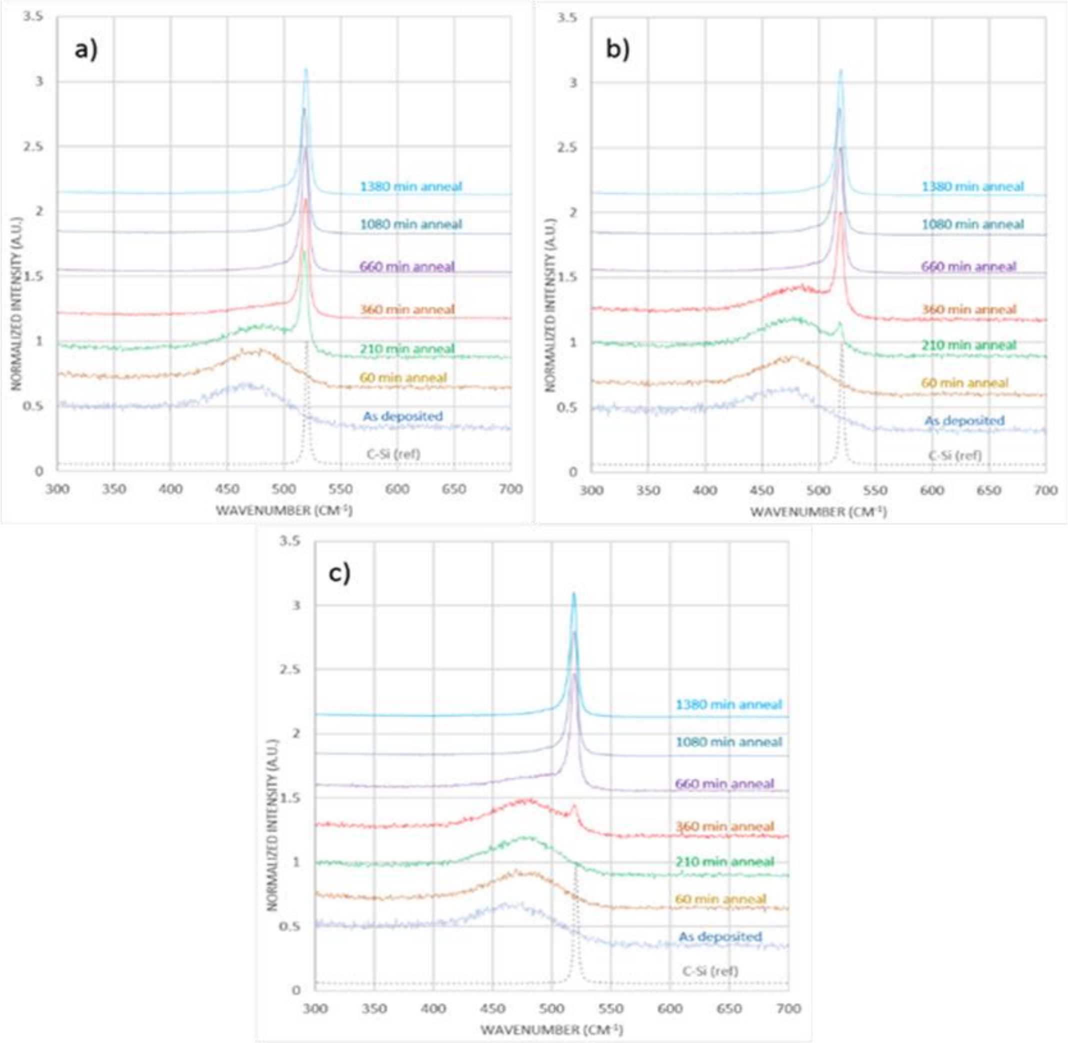

Figure 44: Raman spectroscopy taken from absorber layers before and after 600ºC SPE annealing steps; grown on AIC seed layers annealed at: a) 450ºC, b) 500ºC, and c) 525ºC.

A difference in the crystallization rate, however, is clearly visible when one compares the evolution of the Raman spectra: majority of the crystallization is done within the first 210 min. for the sample with 450^{o}C annealed seed (Figure 44a), 360 min. for the sample with 500^{o}C annealed seed (Figure 44b), and 660 min. the sample with 525^{o}C annealed seed (Figure 44c). A possible explanation for this trend is the amount of grain boundaries on the seed layer diminishing the rate of crystallization. A discussion of the grain boundary contribution is already done regarding the Raman spectra given in Figure 38. As mentioned, the seed layer that was annealed in 450^{o}C is expected to have the smallest amount of grain boundaries, i.e., the greatest amount of crystalline surface for the epitaxial process to occur, therefore the crystallization rate is the highest. A second possible explanation is that it is possible that for seed layers annealed at 500°C and/or 525°C, no epitaxial process occurred, possibly due to a thin layer of native oxide that was formed in between the HF dip and the insert of the samples into the e-beam system. Instead, homogenous solid phase crystallization was the dominant process. Initial observations using scanning electron microscopy (SEM) showed that the seed layer surface of the 450°C annealed sample morphology is indeed imitated on the absorber layer (Figure 45). Further SEM analysis concerning the samples with seed layers annealed at 500 and 525°C, as well as EBSD analyses for all samples is expected to shed more light on this phenomenon.

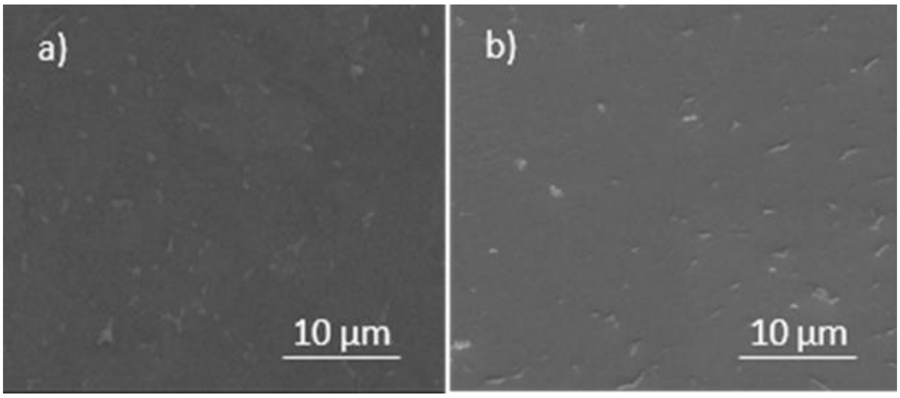

Figure 45: Scanning electron micrographs taken from the seed layer annealed at 450°C (a), and the absorber grown on this layer following 600°C annealing (b). The surface features visible on both images are thought to be discontinuities in film thickness where two crystals coalesced during the AIC process. Similar features being present in both surfaces is indicative that the epitaxial growth occurred in the absorber layer.

Further investigation on SPE studies continued with subsequent experiments. Since the process is based on ex-situ epitaxy, the properties of the interface between the poly-Si seed layer and amorphous silicon is crucial. Any oxide layer can inhibit the epitaxial process. However, during the loading of samples into the chamber, after HF cleaning the surface of the samples were kept in methanol. Another possible problem could be the residual Al on poly-Si layer since after layer exchange of Al and Si the residual Al+Si mixture was removed by mechanical polishing. To address this issue, the possibility of residual Al on the seed surface (left after the mechanical polishing step) was investigated by SIMS analysis which was carried out on a stacked sample with the following layers: intrinsic poly-Si (SPE, 1µm)/poly-Si (AIC, ~180nm)/SiN_x/glass (Figure 46a). All layers were prepared based on their respective standard conditions established in the previous sections. SPE was carried out at 550°C for two days under N_2 atmosphere. As seen in Figure 46b, the Al SIMS profile suggests significant Al concentration at the seed/absorber interface, which diffuses into the absorber layer during annealing.

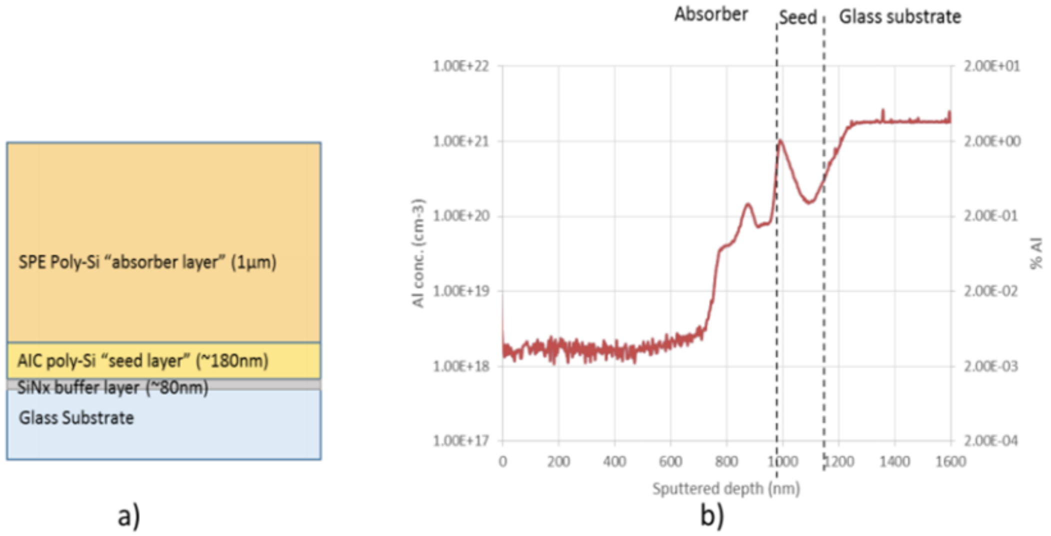

Figure 46: SPE absorber a) a sketch showing the consecutive layers, and b) SIMS depth profile of after annealing at 550°C at 48hrs (w/out Al etch prior to absorber deposition).

In order to ensure a seed surface with no Al residue, a selective Al-etch step prior to absorber layer deposition was added to the standard process. In this manner, just after the mechanical polish step, the seed layers were treated with a H_3O4_P (80) –

CH_3COOH (5) – HNO_3 (5) – H_2O (10) etch solution for approximately 20 seconds. A subsequent 10% HF dip was accomplished to remove the oxides left on the surface. Then, during the sample mounting on the holder and inserting into the e-beam chamber, the surface of the samples were wetted by high purity methanol. The film structure shown in Figure 46a was obtained by SPE. Both Raman FWHM and EBSD analysis (Figures 47a and 47b) revealed that the epitaxial growth was successful, producing large grains with (100) preferred orientation. A control sample that was prepared without the Al step (identical otherwise) did not result in epitaxial growth, as evidenced by Raman analysis (data not shown).

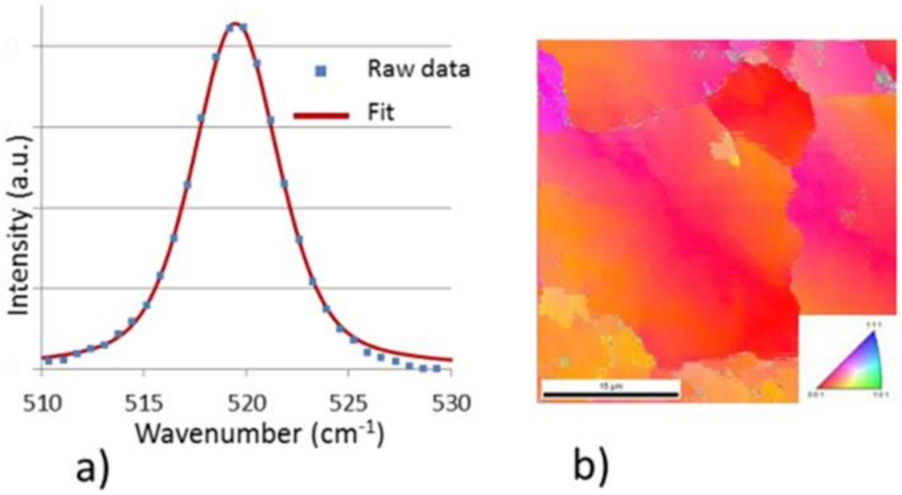

Figure 47: Structure of the SPE absorber layer (Al etch prior to absorber deposition), a) Raman peak with a Lorentzian/Gaussian fit, and b) EBSD image.

CHAPTER 4

INFLUENCE OF VACUUM ANNEALING OF ALUMINUM PRIOR TO AMORPHOUS SILICON DEPOSITION ON ALUMINUM INDUCED CRYSTALLIZATION

It has been known that many factors like temperature [86], Al bulk oxygen content [111], properties of AlO_x [112,113], Al grain structure [114,122] affect the formation of final AIC poly-si layer. Especially, Al grain size has a significant effect on the final grain size of poly-Si layer, the larger the Al grain size, larger the grain size of poly-Si film. After some basic characterizations of AIC process the effect of Al grain structure on the poly-Si film and on the AIC kinetics was investigated.

4.1. Sample Preparation

Two sets of samples were prepared in the a-Si/Al/SiN_x/glass configuration for the annealing experiments. The two sets have the same Al deposition run. However, just before the Si depositon, one set was annealed in vacuum for 2 h which is referred as “pre-annealed” sample and the other set was kept in vacuum at room temperature for 2 h which is referred as the “control” sample. A 1.1 mm thick Schott AF ECO 32 glass was cleaned by ultrasonic cleaning with a sequence of acetone, isopropanol and distilled water 10 min for each. Finally samples are dipped into 10% HF solution for 15 s prior to 80 nm SiN_x deposition. SiN_x film was deposited with “d” conditions as discussed in the previous sections. Then 180 nm Al was deposited by thermal evaporation after reaching a base pressure below $5x10^{-6}$ Torr. In order to form a thin Al-oxide layer on the surface the deposited Al film was kept in atmosphere in clean room for approximately 5 days. After this step, the samples were separated into two groups, and the “pre-annealed” sample set was mounted on substrate holder of the e-beam chamber to be kept at 500 ^{o}C at 7 x 10^{-7} Torr levels for 2 h, while the “control” sample set was placed in the same chamber and kept at room temperature. Following this step, samples were placed onto the substrate holder of electron beam (e-beam) evaporator to deposit 360 nm a-Si layer. The substrate temperature was set to 200 ^{o}C. After reaching a base pressure between 3-6 x 10^{-7} Torr the deposition was started and the deposition rate was adjusted to 1 nm/s. AlO_x interface layer between the Al and a-Si films was examined by PHI 5000 VersaProbe X-ray photoelectron spectroscopy (XPS). Each layer was examined following a 1.5 min Ar-sputtering at 1.5 kV. The samples were annealed in a classical tube furnace between 420 and 450 ^{o}C. Optical microscope (OM) was used for tracking the crystal formation through the glass side of the samples at incremental durations for each temperature. After layer exchange of Al and Si the residual (Al+Si) layer at the top was removed by mechanical polishing. Colloidal silica having 60 nm particles was used for polishing. Electron backscattering diffraction technique (EBSD) was used to analyse the crystalline orientation maps and grain size of the samples. Quanta 400F field emission scanning electron microscopy (SEM) was used for EBSD measurements at 30 kV electron beam acceleration.

4.2. Microscopy Analysis

Optical microscopy (OM) serves a simple and easy way of observing the crystallization behaviour during layer exchange process. The contrast difference between Si crystallites and Al enables observing the growth of Si crystals easily [123]. In Figure 48, the OM images taken from control and pre-annealed samples immediately after a-Si deposition is given.

The results in this section are used by the permission of John Wiley and Sons Publishing with licence number of 3924711226792.

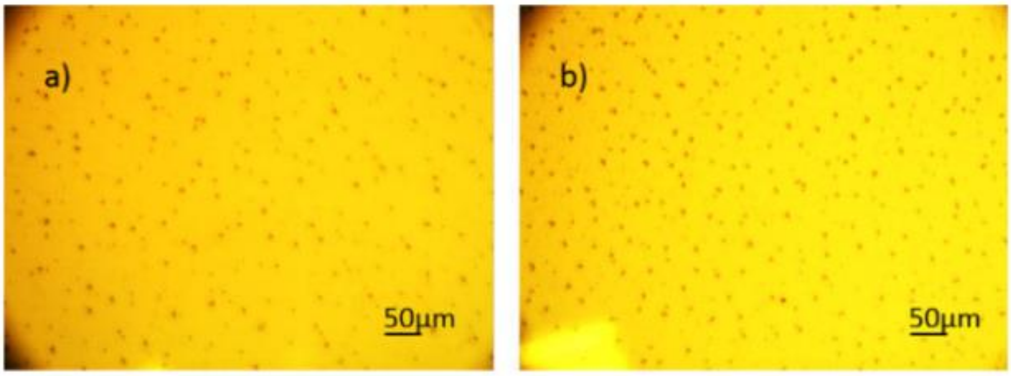

Figure 48: Optical micrographs of as-deposited samples: (a) control and (b) pre-annealed.

Both in Figures 48a and 48b the nucleation can be seen clearly that is occurred during the Si deposition at 200 ^{o}C substrate heating. For each sample set the AIC annealing temperatures of 420, 435 and 450 ^{o}C are were used. In Figures 49 and 50 the selected OM images show the Si/Al interface evolution of the control and as-deposited samples during annealing at 420 ^{o}C. To achieve the full crystallization, the time required for the as-deposited sample set was longer than control sample set. This observation was independent of annealing temperature.

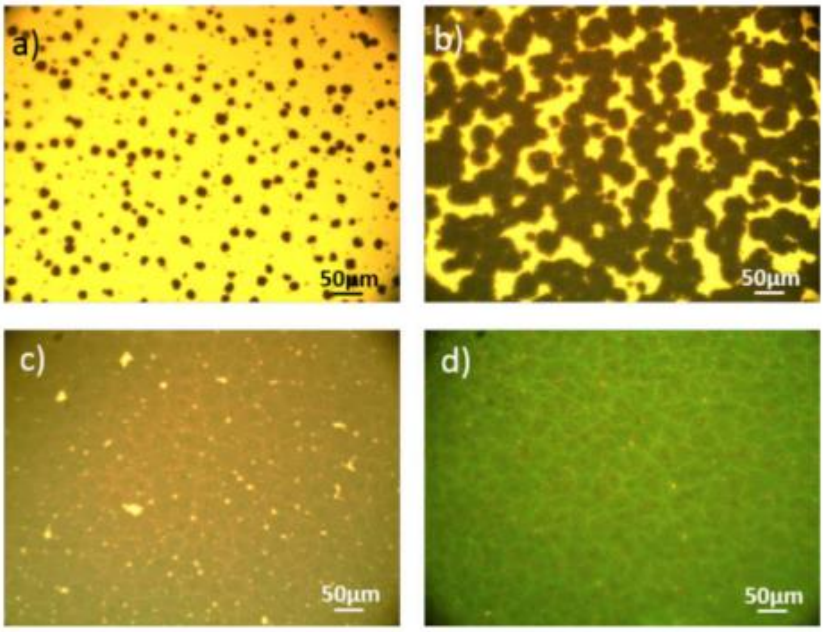

Figure 49: Optical micrographs taken from control samples annealed at 420 °C for varying durations: (a) 40, (b) 65, (c) 90, and (d) 120 min.

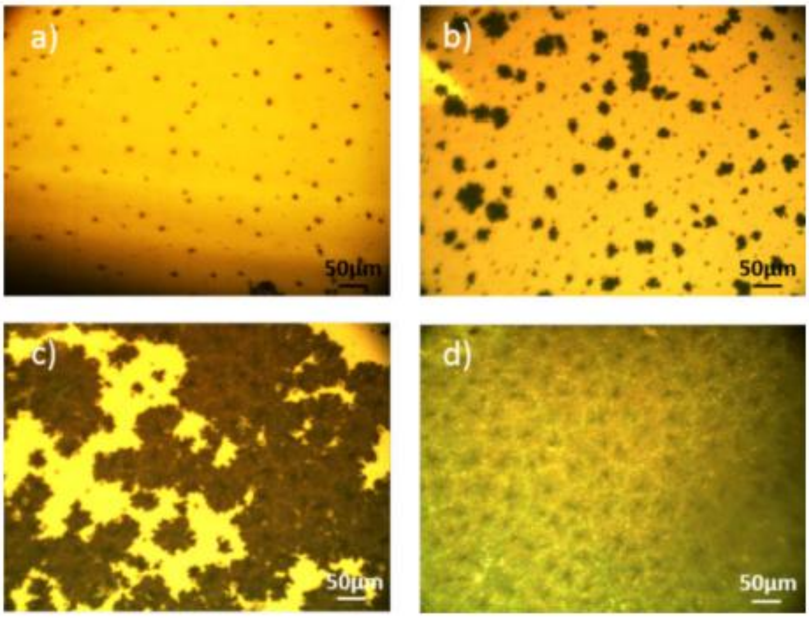

Figure 50: Optical micrographs taken from pre-annealed samples annealed at 420 °C for varying durations: (a) 220, (b) 420, (c) 1080, and (d) 1200 min.

4.3. X-Ray Photoelectron Spectroscopy Analysis

Depth-resolved XPS was used for the control and pre-annealed sample sets (prior to any furnace annealing) in order to examine the effect of vacuum-annealing of the Al layer. Figures 51a and 51b shows the XPS spectra taken from control and pre-annealed samples. The selected depths represents the transition from a-Si film to Al layer. For comparison, all spectra are normalized with respect to their maxima. In both cases, the Al2p near 72 eV peak was visible within several layers into the a-Si film, which suggests that the layer exchange process has already been initiated. The transition from a-Si to the Al film through the interfacial AlO_x layer spanned over 80 sputtering processes for the control sample, however the same transition was observed only within five sputtering runs for the pre-annealed sample.

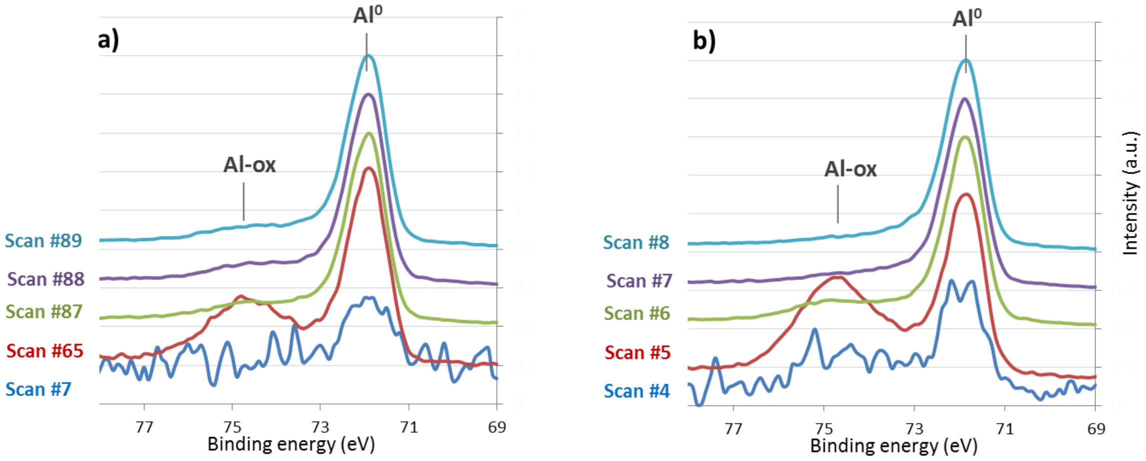

Figure 51: Selected XPS spectra taken from a-Si/Al/SiN_x/glass stacks: (a) control sample and (b) pre-annealed sample. All spectra are normalized with respect to their maxima.

XPS spectra of the highest ratio of Al-oxide to metallic Al peak for the control (Figure 51a, scan no.65) and pre-annealed (Figure 51b, scan no. 5) sample is shown in Figure

52. Al-oxide and metallic Al peaks can be seen in both samples however Al-oxide peak is greater in the pre-annealed sample.

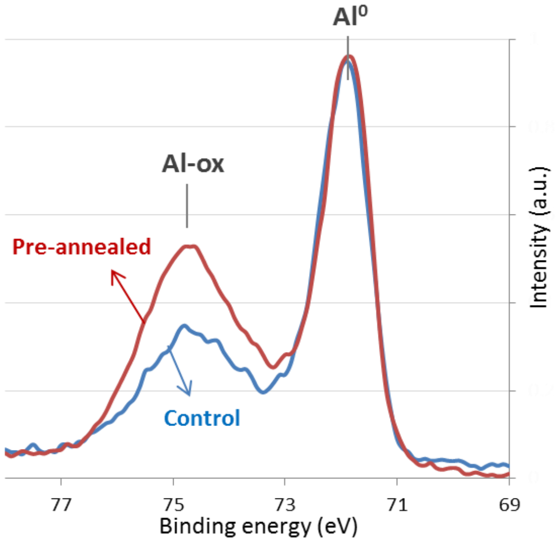

Figure 52: Comparison of the normalized photoelectron spectra showing the highest Al-oxide peak for the control and pre-annealed samples.

4.4. Electron Back Scattering Diffraction Analysis of Al and Poly-Si layers

The correlation between Al and poly-Si layer was analysed by EBSD. Prior to a-Si deposition in the e-beam chamber, some portion of the control and pre-annealed samples were masked such that the Al layers go through the identical thermal cycles like as-deposited a-Si/Al/SiN_x full-stack samples (the bare Al layers were not subjected to any post-deposition annealing). The surface oxide of the masked areas were removed by mechanical polishing. In Figure 53a and 53b the EBSD maps taken from control and pre-annealed Al films are shown. The pixelated image in Figure 53a indicates that the resolution of the EBSD system was not sufficient to detect the grain structure of the control sample. However the Kikuchi patterns (left top on Figure 53a) verifies the crystallinity of this layer. Previously, 65 nm grain size of Al films deposited by thermal evaporation was presented [122]. Due to an interference in the EBSD pattern from the neighbouring grains, the analysis software cannot identify the crystal orientation properly at such small grain sizes. In contrast to control sample, the EBSD image (Figure 53b) from the pre-annealed Al film reveals much larger grains on the order of micro meter sizes which indicates that the grain enlargement occurred during the vacuum anneal of Al.

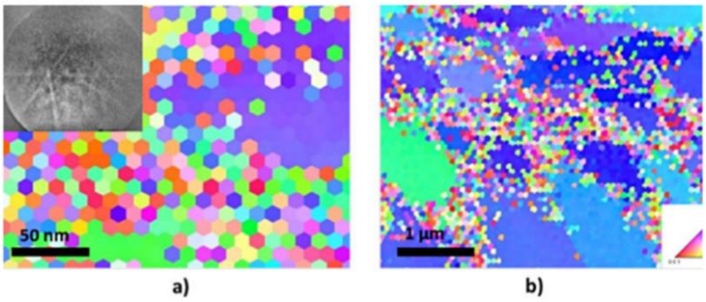

Figure 53: EBSD images taken from Al layers: (a) control sample (inset showing the Kikuchi pattern) and (b) pre-annealed sample.

The grain structure of the poly-Si layers produced by AIC at two different conditions were compared by EBSD. First, the crystallization was monitored by optical microscopy and then the residual part (Al-Si mixture) at the top of the samples was removed by mechanical polishing. The EBSD images taken from fully crystallized control and pre-annealed samples are shown in Figures 54a and 54b.

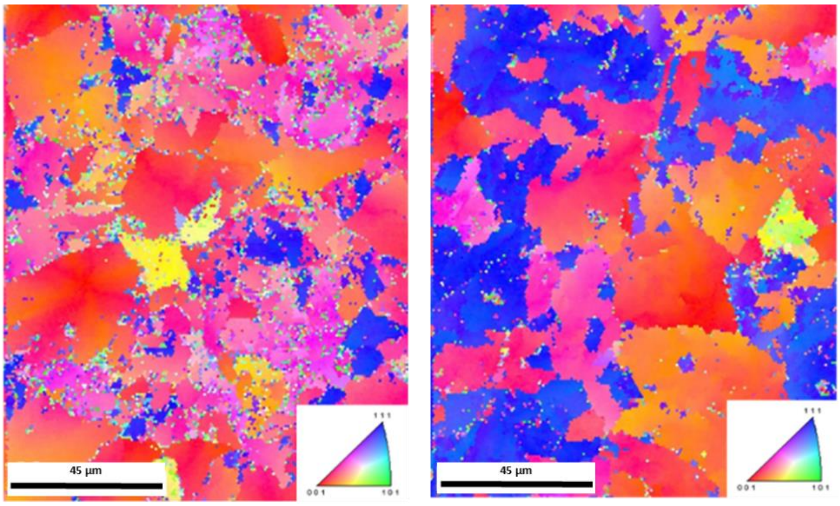

a) b)

Figure 54: EBSD images taken from final poly-Si layers: (a) control sample and (b) pre-annealed sample. Grain colors correspond to crystal axes normal to the surface of poly-Si films as represented in the color codes given in the lower right inset.

Both of the samples contain large grains that are close to <100> orientations normal to the surface. Beside this <100> slight preference, a relatively wide distribution can be observed in the control sample, whereas the large grains close to <111> orientation are also prominent for the pre-annealed sample. The inverse pole figures in Figure 55a (control sample) and 55b (pre-annealed sample) shows the orientation distribution obtained from Figure 54.

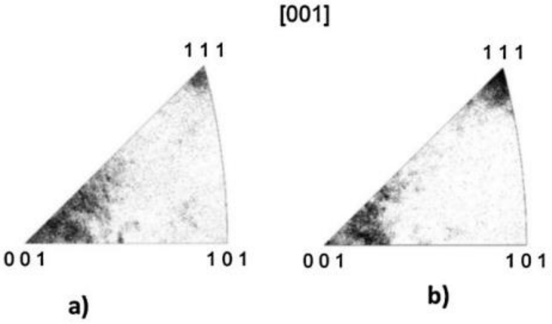

Figure 55: EBSD inverse pole figures showing the orientation distribution of poly-Si films in the direction normal to the surface: (a) control sample and (b) pre-annealed sample

4.5. Discussion

Here the main focus was the effect of Al annealing on AIC process. Given the complexity of the factors affecting AIC, it was important to eliminate variables that may have had any compounding influence on the crystallization mechanism. To eliminate any kind of resultant structural complexity, two nearly identical sample sets were produced and the only difference between the sample sets was a vacuum anneal step of Al layers prior to a-Si deposition. Hence, any observed difference could be attributed to the vacuum annealing of Al/SiN_x/glass stack.

OM images taken from both control and pre-annealed samples were shown in Figure 48. Both of the samples indicate small nuclei which suggests that the crystallization process has already begun during a-Si deposition. This situation was an unexpected observation, considering that during a-Si deposition the thermal load on the substrate was relatively small, around 6 min at 200 ^oC. Wang et al. have reported that the annealing time required for complete AIC layer exchange at 195 ^oC was on the order of 5 days [124]. This observation could be understood considering the AlO_x layer: in Figure 52, the XPS spectra of the highest AlO_x peaks are given for the control and pre-annealed samples. Both of the samples contain metallic Al and oxidic Al in the interface layer. This could be indicative of the fact that the Al – oxide interface does not form a continuous layer, where Si transition to metallic Al exists. Direct transition from a-Si to the metallic Al film exists. If this is true, then it would also explain the early nucleation that occurred during a-Si deposition for both samples; without a continuous Al-oxide layer acting as a diffusion barrier, the Si atoms easily penetrated into the Al layer and formed the crystalline nuclei. Moreover, during deposition Si adatoms can directly diffuse into the Al matrix upon arrival. In this way, the energy necessary to break the a-Si bonds will be surpassed unlike the case of post-deposition annealing of the a-Si/Al system. Hence, the AIC process could be implemented at lower energies.

The crystallization evolution was monitored by OM images (Figures 49, 50) and then the crystallization percentages were calculated (via public domain image processing software ImageJ). The crystallization percentage vs annealing time was plotted for annealing durations of 420, 435 and 450 ^{o}C for both samples as given in Figure 56.

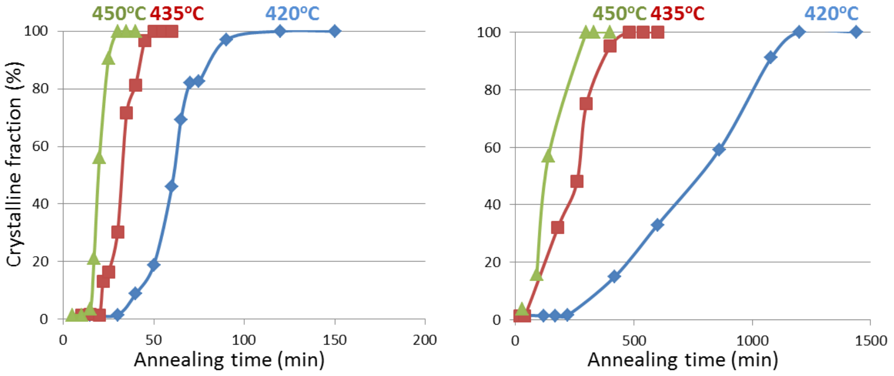

a)

b)

Figure 56: Crystallization percentage versus annealing time at 420, 435, and 450 ^{o}C: (a) control sample and (b) pre-annealed sample.

In Figure 56, both of the samples show the typical “Avrami” behaviour for the three temperature values where the crystallization rate increases significantly with temperature. An Arrhenius type relationship between temperature and crystallization rate for AIC is well known and has been reported before [110]. However, when crystallization durations in Figures 56a and 56b are compared, it can be seen that time required for crystallization is roughly an order of magnitude greater for the pre-annealed sample set than that for the control sample set for all annealing temperatures. The crystallization kinetics causes this difference in the time scales, as it was shown in Figure 48, the nucleation has already been started just after the a-Si deposition. The difference in growth rates requires an explanation through the vacuum annealing of the Al/SiN_x/glass prior to a-Si deposition. By this way, AlO_x layer and Al grain structure will be considered as being the two potential parameters.

In the light of the XPS spectra of as grown samples shown in Figure 51, a small Al peak was detected in the layers close to the surface. The series of XPS spectra seems to be same at first glance, however in the case of control sample (Figure 51a) it spun over 83 sputtered layers while this number is 5 for the pre-annealed sample. A distinct Al-oxide peak was seen for about 20 consecutive depths for the control sample, while for the pre-annealed sample, XPS spectrum from only one depth shows a well-defined Al-oxide peak. The sputter rate of Al-oxide is much lower than that of Al [125], so it is difficult to estimate the thickness ratio of the Al-oxide layers in control and pre-annealed samples quantitatively. Nevertheless, it appears that the control sample has considerably thicker oxide layer, which is confirmed by the depth resolved O1s spectra (data not shown).

AlO_x interfacial layer is well known about having a significant effect on the AIC kinetics as reported by Kim et al. [126]. It was clarified that the presence of AlO_x membrane reduces the crystallization rate of AIC process notably by restricting the diffusion of Si atoms into Al layer. If all the other parameters are kept constant, it is therefore expected that crystallization rate is lowered by thicker oxide layer. This statement seems to contradict with findings discussed above; in the control sample, the Al-oxide layer appears to be considerably thicker, whereas, the growth rate of Si crystallites are much greater than the pre-annealed sample. The chemical nature of the AlO_x layer may be the one possible factor to consider (as opposed to its thickness). When the oxide/metal peak ratios for the Al2p of control and pre-annealed samples are compared (Figure 52), it is seen the pre-annealed spectra indicate a considerably higher oxide ratio relative to the control sample. This could indicate that during the pre-annealing treatment the surface Al-oxides condensed into a thin yet heavily oxidized layer, which inhibits the crystal growth process by acting as a diffusion barrier.

However the interfacial layer alone is not enough to explain the difference in growth rates. It is accepted that Al grain boundaries behave as preferential sites for nucleation [110,124,117,127]. As discussed before, in the light of EBSD images in Figure 53, the grain size of the pre-annealed sample is much larger than the control sample which suggests a much smaller Al grain boundary density for the pre-annealed sample. Owning a smaller quantity of GBs, lower diffusivity of Si through the AlO_x layer of the pre-annealed sample should have resulted in a drastically reduced nucleation rate (compared to the control sample), which was not the case.

Therefore, the inconsistency in the observed growth rate is attributed to the diffusivity of Si through the Al grain boundaries. Since the diffusivity of Si in Al is greatly enhanced in the grain boundaries [114], a smaller grain size yields a higher crystallization rate. This situation would be valid if one considers the AIC model proposed by Wang et al. [124]. This model claims that the crystallization is utilized through the wetting of Al grain boundaries by the a-Si film. The case here can be addressed as; while the control sample had a much thicker layer hindering diffusion of Si adatoms, the available nucleation sites were greater due to the small Al grain size (i.e., high Al GB density). The two mechanisms therefore balanced each other out, resulting in a net nucleation rate that is comparable with the pre-annealed sample (while the growth rate differed immensely).

It is worthwhile to evaluate a caution against this model at this point. In their study on the kinetic simulation of AIC, Sarikov et al. [127] showed that Si diffusivity in bulk Al is negligibly small compared to diffusivity in AlO_X membrane layer. In the present study this conflict is acknowledged and the Al-grain boundary model is handled as the most suitable one in explaining the data.

EBSD images of the final poly-Si layers in Figure 54 (both samples were annealed at 420 ^oC) indicate that grain sizes were comparable for both sample. Since the grain size is mostly determined by the nuclei density at the beginning of crystallization [110], this was an expected case, which has already been shown to be similar for both sample sets. Meanwhile, the grain orientation distribution of the samples appears to be different. Figures 54 and 55 show that in the pre-annealed sample, large grains with orientations near <111> are seen along with those that are near <100>. The factors that have impact on grain size distribution have been investigated before by Schneider et al. [117] and by Sarikov et al. [127]. Again the grain orientation is mostly determined during nucleation, and does not change in the following step. The nucleation sites occurred preferentially on the Al grain boundaries and this means that the Al grain orientation could have an impact on the Si nuclei. Since there was a lack of clarity in EBSD scan for the control sample, the direct comparison of the Al grain orientations of the samples was not possible. However it is clear that the grain structure of the pre-annealed sample is significantly different than the control sample. It is possible that the difference of the grain orientation of the Al layer could have contributed to the inconsistency observed in the poly-Si grain orientation. A second significant factor is, as explained in Ref [127] the correlation between the specific energy of the AlO_x/Si-grain interface ($\sigma_{AlOx/Si}$) and the Al/Si-grain interface ($\sigma_{Al/c-Si}$). The ratio of these interfacial energies strongly affect the degree of preferential orientation. Considering the properties of the AlO_x and the Al layers were significantly altered by the vacuum anneal and the influence of the “new” ratio of the interfacial energies on the final grain orientations could be expected. However a quantitative measurement of the interface energies was not possible for this study.

CHAPTER 5

STRUCTURAL PROPERTIES OF AMORPHOUS SILICON FILMS AND THEIR EFFECT ON ALUMINIUM INDUCED CRYSTALLIZATION

In this part of the thesis, two different amorphous silicon (a-Si) deposition methods, e-beam evaporation and plasma enhanced chemical vapour deposition (PECVD), are compared for AIC process. Both techniques have prominent advantages: e-beam evaporation exhibits high deposition rate, however PECVD enables large area deposition. Many parameters of AIC process like annealing temperature [86], Al grain structure [114,122], properties of AlO_x layer at Si/Al interface [112,113] have been investigated before. However the influence of a-Si layer on AIC has not been largely explored (barring a study focusing on the hydrogen content of sputtered a-Si films [128])

5.1. Sample Preparation

The AIC experiments were carried out using a-Si/Al/SiN_x/glass stack configuration. Schott AF32 Eco glass substrates were cleaned as discussed in the previous parts. After glass cleaning, approximately 80 nm SiN_x was deposited by PECVD using the standard conditions ("d" conditions; discussed in 3.2.1). As the first step of AIC process, 180 nm Al was deposited by using thermal evaporation. The same Al/SiN_x/glass batch was used in order to isolate the a-Si layer as the sole variable. Then AlO_x formation was carried out after 4 days of clean room environment exposure and samples were separated into 4 batches prior to a-Si deposition. The four different a-Si deposition runs and their corresponding sample designations are given in Table 9.

Table 9: a-Si deposition methods and parameters for different batches

Batch Name	a-Si Deposition	Substrate Temperature (°C)	SiH_4:H_2 Ratio
E-RT	E-beam	25	N/A
E-HT	E-beam	420	N/A
P-9	PECVD	25	1:9
P-29	PECVD	25	1:29

All of the final thickness of the a-Si films were 360 nm. For the e-beam deposition runs (E-RT and E-HT) the base pressure of the e-beam system was 1-2 x 10^{-7} Torr, which rose up as high as 8 x 10^{-7} Torr during evaporation. The deposition rate was 1.5 nm/sec. The PECVD depositions (P-9 and P-29) were done using a capacitively coupled plasma system with a base pressure of 5 x 10^{-6} Torr and an operating pressure of 1 Torr. A-Si film growth in PECVD silicon was done by using a mixture of 10%SiH_4 -90%H_2 as the silane source. For batch P-9, 350 sccm silane mixture was given into the chamber, which results in a deposition rate of approximately 0.4nm / sec. For batch P-29, the silane mixture was flown at 100 sccm and further diluted by H_2 at 200 sccm, corresponding to a deposition rate of about 0.15 nm / sec. During deposition of a-Si, also additional quartz and Si-wafer pieces were loaded into the chamber to enable Raman and FTIR analysis, respectively. Then the samples were annealed in a classical tube furnace for varying durations between 420 and 450 °C. The AIC process was monitored by using optical microscope. The micrographs were obtained by reflection of the light through the glass side of the samples.

5.2. In-situ AIC during e-beam Si deposition

As shown in Table 8, the e-beam deposition was done at room temperature (E-RT) and 420 °C (E-HT). In Figures 57a and 57b the optical micrographs of E-RT and E-HT just after a-Si deposition (before annealing) are given, respectively. E-RT sample shows no indication of crystallization at the a-Si/Al interface (Figure 57a), however small dendritic Si crystallites are seen for the E-HT sample in Figure 57b. The small crystallites suggest that the nucleation has already begun at the end of a-Si deposition.

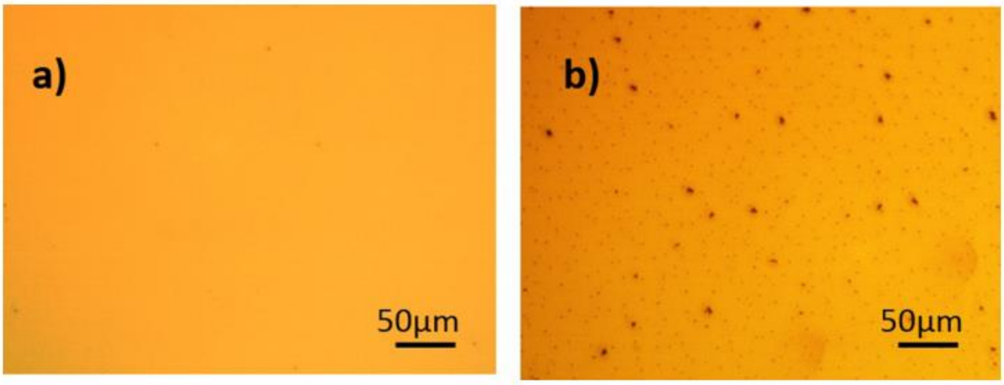

Figure 57: Optical micrographs from the a-Si / Al interface taken from samples from batches a) E-RT, and b) E-HT. The interface for the E-RT sample appears featureless, while small crystal nuclei are visible for the E-HT sample.

5.3. Microscopy Analysis

In Figures 58 and 59, the selected micrographs present the a-Si/Al interface of samples from batches E-RT, E-HT, P-9 and P-29 after annealing at 420 and 450 ^{o}C for different annealing durations, respectively. The both annealing temperature show that e-beam deposited a-Si samples (Figures 58a and 58b, Figures 59a and 59b) have considerably higher crystallization rate with respect to PECVD deposited a-Si samples (Figures 58c and 58d, Figures 59c and 59d).

When the e–beam deposited samples (E-RT and E-HT) are compared, it can be clearly seen that E-HT has higher crystallization rate and smaller crystallite size which was an expected result since the nucleation had already started just after a-Si deposition (Figure 57). However, for E-RT sample the nucleation barrier that had to be overcome for E-RT was not present. The early stages of the micrographs of 420 ^{o}C (Figures 58a and 58b, 15 min) and 450 ^{o}C (Figures 59a and 59b, 10 min) annealing apparently indicate the crystallization rate difference between E-RT and E-HT. While E-HT is well in its growth stage, nucleation has not yet started for E-RT.

When the PECVD deposited samples (P-9 and P-29) are compared voids of diameters on the order of 50-100 μm is visible for P-9 sample (Figures 58c and 59c), however no such voids are seen for P-29 (Figures 58d and 59d). Excessive residual hydrogen in PECVD grown a-Si has been known to cause micro-voids upon subsequent heat treatment [129,130]. Besides, the AIC kinetics of P-9 and P-29 differ in terms of annealing duration for initial nucleation as well. The complete crystallization for P-9 was significantly shorter than P-29.

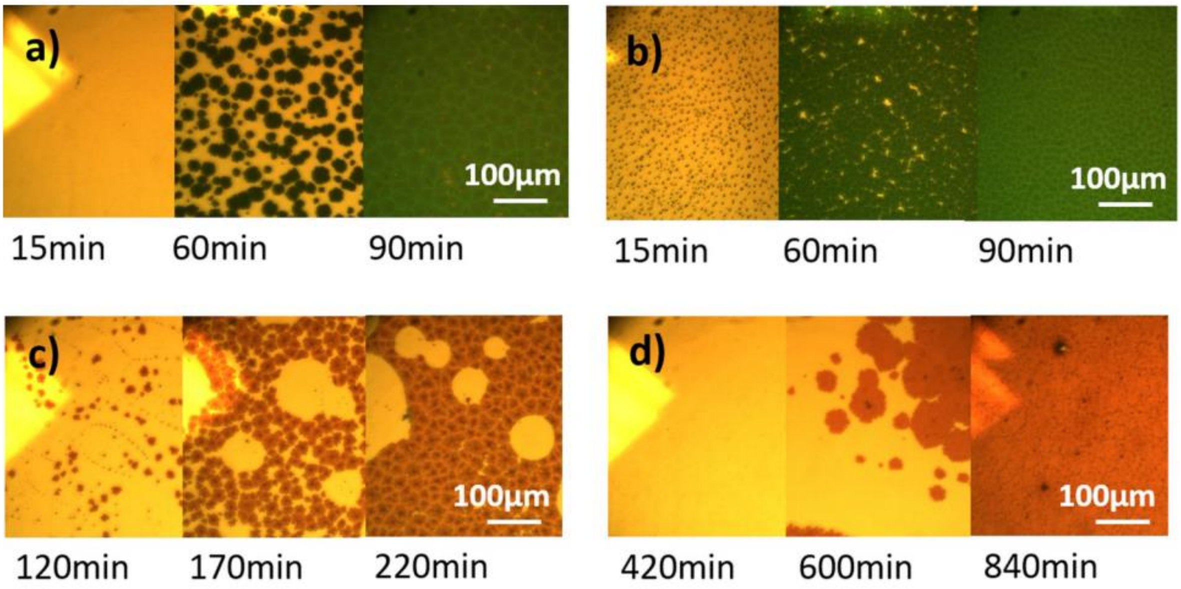

Figure 58: Optical micrographs taken from the a-Si / Al interface of samples annealed at 420 ^{o}C at varying annealing times (as given in the lower left corner insert for each micrograph), a) E-RT, b) E-HT, c) P-9, d) P-29.

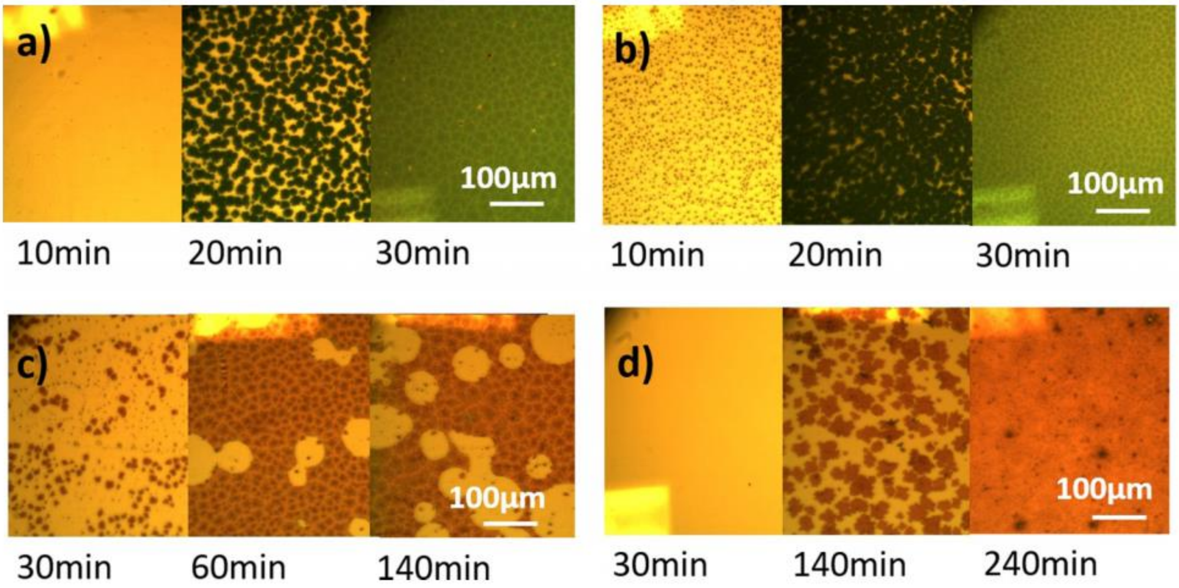

Figure 59: Optical micrographs taken from the a-Si / Al interface of samples annealed at 450^{o}C at varying annealing times (as given in the lower left corner insert for each micrograph), a) E-RT, b) E-HT, c) P-9, d) P-29.

5.4. EBSD Analysis

After the samples were completely crystallized, the top residual (Al-Si) layer was removed by mechanical polishing to investigate the grain structure of the samples by electron backscatter diffraction (EBSD). In Figure 60 the EBSD images of the samples annealed at 450 ^{o}C are given.

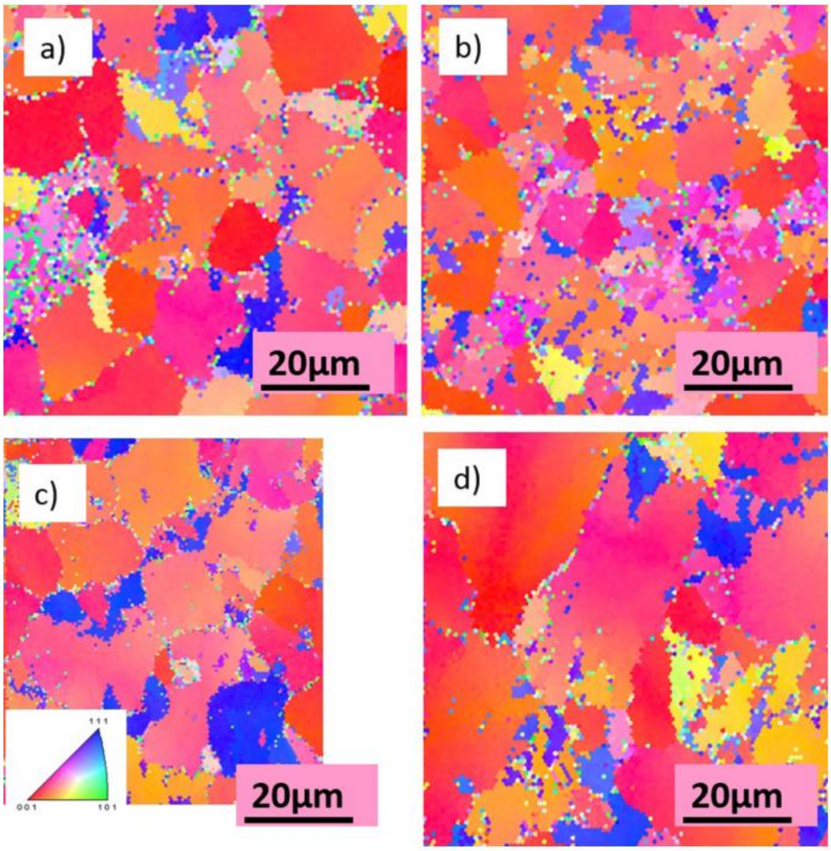

Figure 60: EBSD images taken from fully crystallized samples annealed at 450 ºC, a) E-RT, b) E-HT, c) P-9, and d) P-29. The colors represents the orientation of grains according to the color code given in the lower left corner inset.

In Figure 60, as expected an inverse relation between grain size and crystallization rate was observed. P-29 sample has the highest average grain size and E-HT sample has the lowest. The samples show no significant difference in grain orientation. All samples have preferred orientation toward <100> which is indicated by the dominance of red/orange color grains.

5.5. Raman and FTIR Spectroscopy Analysis

The samples were characterized by Raman spectroscopy and Fourier Transform Infrared Spectroscopy (FTIR) in order to clarify the observed differences in AIC kinetics between the four sample sets. In Figure 61 the Raman spectra of a-Si samples deposited on quartz substrates during each deposition run are given.

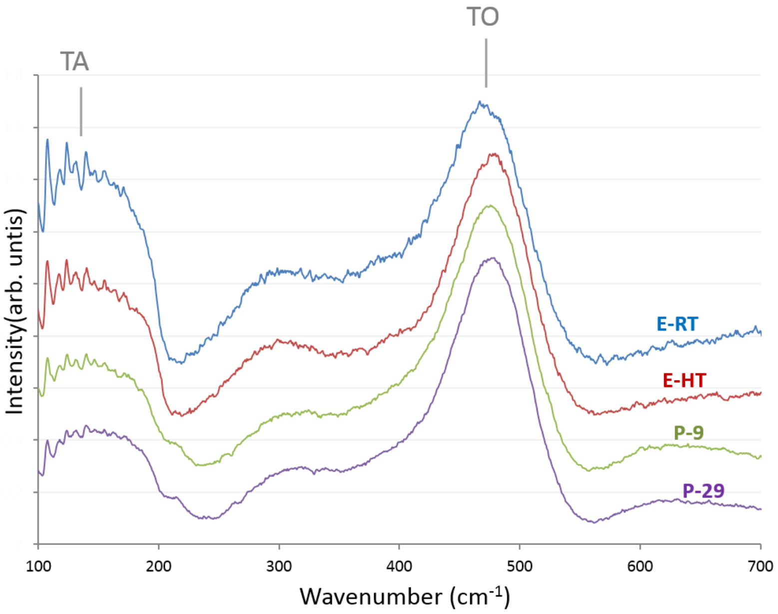

Figure 61: Normalized Raman spectra taken from the as-deposited a-Si films from batches E-RT, E-HT, P-9 and P-29. Spectra are stacked on the same graph (with varying intensity off sets) for ease of comparison. Approximate positions of the transverse acoustic (TA) and transverse optical (TO) peaks are indicated on the graph.

In Figure 61, the characteristic peaks related with transverse acoustic (TA), longitudinal acoustic (LA), and transverse optic (TO) modes are visible in the vicinity of 150, 300 and 480 cm^{-1}, respectively (for simplicity, only the peak positions of TA and TO modes are indicated on the graph). Moreover, P-9 and P-29 samples (PECVD grown) indicated a small feature near 620 cm^{-1}, which has previously been attributed to Si-H wagging modes [130]. TA and TO peaks are considered to be essential for a-Si bond structure. Correspondingly, the line width of the TO peak is directly proportional to the short range disorder and greater intensity ratio between TA and TO peaks (I_{TA} / I_{TO}) is known to indicate a higher intermediate range disorder [130,131].

With regard to this consideration, it seems that E-RT sample has higher short range disorder with respect to the other samples and there is no significant difference for TO line width is apparent between E-HT, P-9 and P-29. However, I_{TA} / I_{TO} ratio of each spectrum indicates a more notable trend. Based on the I_{TA} / I_{TO} ratios, the intermediate range disorder for the a-Si films, ranks as follows from the most disordered to the least: E-RT > E-HT > P-9 > P-29. Based on this result, PECVD grown samples (P-9, P-29) have higher order which is attributed to the presence of hydrogen in the a-Si. The strain relieving effect of hydrogen on the a-Si network was discussed before by Morell et. al. as it is related to their comparison between PECVD and (un-hydrogenated) sputtered films [132].

The heart of the AIC process is the dissolution of a-Si in Al and the following precipitation as discussed before. The solubility of a-Si is related with its chemical potential, $\mu_{a\text{-}Si}$, where higher $\mu_{a\text{-}Si}$ makes the dissolution process easier by lowering the stability of a-Si. In this perspective, keeping all other process variables constant, higher disorder in the a-Si film would correspond to lower activation energies for its dissolution in Al which results in higher crystallization rates. Although the disorder in the E-RT sample is greater than the E-HT sample, the latter has higher crystallization rate. This situation is an exception about the trend given above for the disorder in different types of a-Si films based on Raman spectra is in accord with the crystallization rates observed by optical microscopy. The reason of this exception has already been given as the in-situ nucleation process that had occurred during the a-Si deposition of the E-HT sample.

FTIR spectroscopy was conducted for P-9 and P-29 a-Si layers on Si wafer substrates to further analyse the nature of hydrogen bonding in the PECVD samples. In Figure 62 FTIR analysis of the samples are given. The wavenumber range that is related with the bending modes of Si-H bonds are shown in Figure 62a. A peak around 640 cm^{-1}, which is associated with the bend-rock-wag modes, is observed in both samples, while in P-9 sample, two additional peaks between 800 and 900 cm^{-1} is seen. These two peaks are associated with bend/scissors and wag modes and are indicative of the presence of SiH_2 [130]. From Figures 62b to 62d the further evidence of this observation can be found for each sample. In this range two peaks are identified. One of them is around 2000 cm^{-1}, which is low stretching mode related to SiH bonds and the other peak is high stretching mode around 2070-2090 cm^{-1} which is associated with SiH_2 bonds [128]. When Figures 62c and 62d are compared, it is understood that P-9 sample has significantly higher SiH_2 bonds with respect to sample P-29, which are known to constitute poor quality a-Si films [130]. In the case of sample P-29, this can be explained based on the fact that, at high H_2 dilution the additional hydrogen in the system attacks the weakly bound SiH_2, dissociating it to the more stable form of SiH. On the other hand, there is no significant difference in total hydrogen quantity of both films. The hydrogen in P-29 is mostly in SiH form which builds up higher film stability and as a result of this it causes lower AIC rates. Moreover, upon annealing the weakly bound SiH_2 in sample P-9 lead to hydrogen micro-voids.

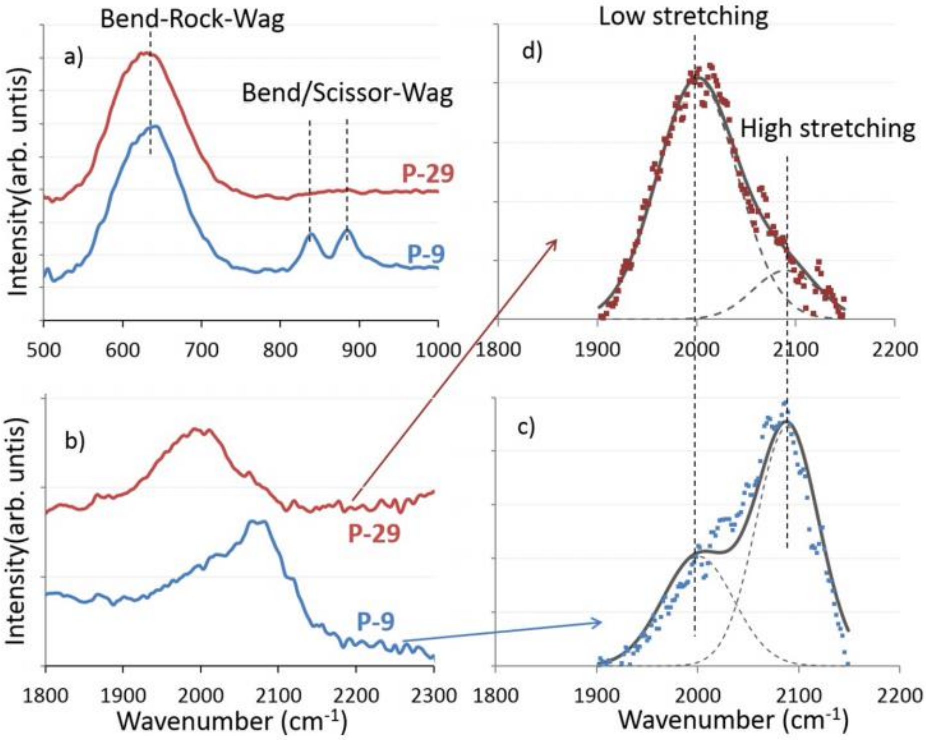

Figure 62: Normalized FTIR spectra taken from the as-deposited a-Si films from batches P-9 and P-29: a) Bend modes, b) stretch modes, c) Gaussian

CHAPTER 6

LASER ASSISTED PROCESSING

Most manufacturing processes attach priority to the low production costs and efficiency. As the technology developes, the new approaches for the conventional production steps have emerged. In this manner, solar industry also chooses the applicable conditions for the market in terms of production lines. This technology improvement caused the solar energy feasible since the serious researches started in the late 70s. The use of lasers also emerged in solar cell productions as the photovoltaic technologies are improved day by day. For wafer based solar cell process, the laser can be used for cutting the wafers, drilling metal wrap through (MWT) and emitter wrap through (EWT), edge isolation, selectively increasing the doping concentration under the contact fingers [133]. Also the use of laser emerge in thin film processes which can be the significant steps for preparing solar modules and cells. The laser scribing for amorphous and microcrystalline solar modules is the crucial step for obtaining the cells connected in series on large area [134]. In this section, poly-Si obtained by laser crystallization of amorphous silicon and laser doping of poly-Si films have been explained. As a result of laser doping Homojunction concept for thin film crystalline silicon on glass approach has been studied through laser doping process. Finally some solar cell results have been given after obtaining quasi cells (mesa cell).

6.1. Thin film polycrystalline silicon solar cells by laser processing

6.1.1. Diode Laser Crystallization

An important application of laser for thin film concept is the crystallization of amorphous silicon. The most common techniques of furnace annealing (SPC) and metal induced crystallization (MIC) for the crystallization of amorphous silicon have been known for many years. However, in the last decade the crystallization by laser have also been studied extensively. The fast process and high quality yield of laser crystallization opens up a promising area for silicon thin film photovoltaics. The laser induced crystallization is liquid phase crystallization (LPC) since the laser beam melts the silicon locally and then silicon is solidified as a crystal. Laser crystallization of amorphous silicon yields high quality polycrystalline silicon on glass with large grain size up to few millimeters [135]. In addition, the laser crystallization eliminates the high durations of furnace annealing. Laser melting of the silicon leads to an epitaxial regrowth of the silicon on the solidified region which leads to enlarging grains during laser scanning. Figure 63 shows a 10 µm silicon layer crystallized by cw-diode laser where the grain structures are apparent after applying pyramid etching procedure with KOH/IPA.

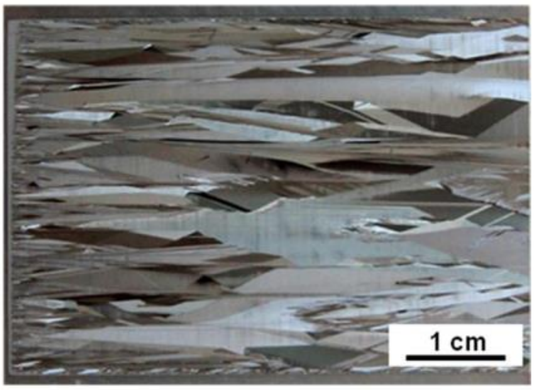

Figure 63: 10 µm silicon layer crystallized by cw-diode laser [135]

At the beginning of the scan, the grain structures are very small with respect to the end of the scan. Furthermore, the grains expand up to cm sizes. It can be understood from Figure 63 the laser is scanned on the Si surface from left to right.

6.1.2. Laser Doping Concept

Laser doping (LD) have been known for many years. Firstly, the wide spread application of LD was for selective emitter process which reduces the series resistance by increasing the dopant concentration under the contact fingers [136], [137]. Additionally, LD is used for full area doping to obtain a p-n junction. Laser doping of semiconductors has emerged first in the 60s [138] and continued even also during the 80s with some detailed research [139,140]. Up to now, with the development of laser technologies, LD of semiconductors has received great attention due to its fast and simple process ability. LD enables local selectivity of dopant incorporation as well as full area doping. It is possible to obtain highly doped regions or emitter layers by laser scanning or pulses using different types of precursors like boron or phosphorus [139], [140]. LD for solar cell applications can be classified into three processing types with respect to the usage of precursor: (a) gas immersed laser doping (GILD), where silicon material is immersed in precursor dopant gas [141], (b) wet laser doping using liquids [142], and (c) dry laser doping, where a solid thin film is used as a dopant precursor [143,144]. Among these methods of LD, gas immersed and wet laser doping requires more complex laser systems which increase cost in terms of production [145]. As a result, dry laser is the most suitable method for LD process. It is possible to obtain the dopant source layer using different methods like PECVD and spin-on coating [146], [147].

6.1.3. Sample Preparation

In this part of the thesis, polycrystalline silicon thin film homojunction solar cells were investigated. The crystallization of the material and doping were both achieved by laser. The constructed cells were analyzed by the basic characterization techniques. In all of the laser based experiments LIMO cw-diode infrared (808 nm) laser was used. The line shaped laser has a gaussian profile with a width of 0.177 mm (FWHM) in scan direction and a top-hat profile with a length of 31 mm perpendicular to the scanning direction. A photograph of the system is shown in Figure 64.

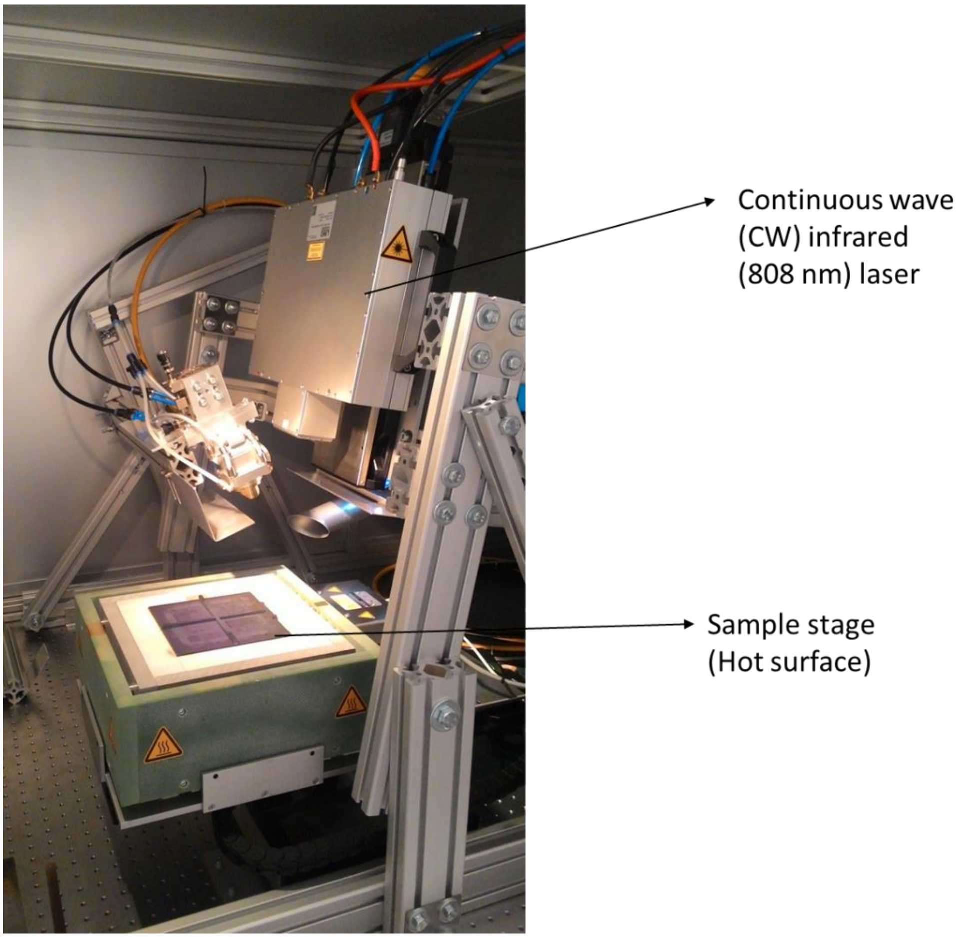

Figure 64: cw-diode laser system used at HZB, Germany

The system has ~12x12 cm^2 metal sample stage which can be divided into four 5x5 cm^2 individual areas. The heating over 700 ^{o}C is possible on the stage.

In all of the laser based (lazer doping, laser crystallization) experiments, Schott borosilicate glass with a thickness of 3 mm was used. Prior to intermediate layer (IL) deposition the 5x5 cm^2 glasses were exposed to alkaline cleaning which is strongly base based.

6.1.3.1.Buffer Layer Deposition (Intermediate Layer(IL))

IL is composed of three layers. IL stack was deposited by AKT1600 PECVD cluster tool following a sequence of SiN_x, SiO_x, and SiO_xN_y with a final total thickness of about 200 nm (Figure 65). During IL deposition, amorphous SiN_x, SiO_x, and SiO_xN_y materials were deposited one by one and substrate heating was kept at 400 °C. The deposition was performed by the dissociation of the gas mixtures of SiH_4, H_2, CO_2 and N_2.

Figure 65: Substrate with buffer layer stack

6.1.3.2. Amorphous Silicon (a-Si:H) Deposition

Then the samples were followed by the a-Si:H absorber layer deposition. 10 µm of intrinsic a-Si:H was deposited by PECVD and then a thin a-Si:H doping layers were also deposited just after the absorber layer doping. Both n-type and p-type doping layers were deposited about 10 nm thickness (Figure 66).

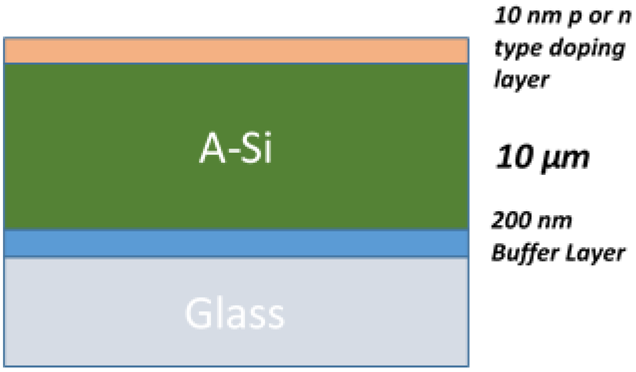

Figure 66: a-Si:H and doping layer depositions

6.1.3.3. Laser Crystallization

The samples were crystallized in an air atmosphere. The side view of the process is shown in Figure 67. The laser crystallization was performed with 10 mm/s scan velocity with 24.5 A current. The samples were heated on a stage at 700 ^{o}C for 15 minutes before laser scanning and after crystallization, samples were cooled down on a warmer stage.

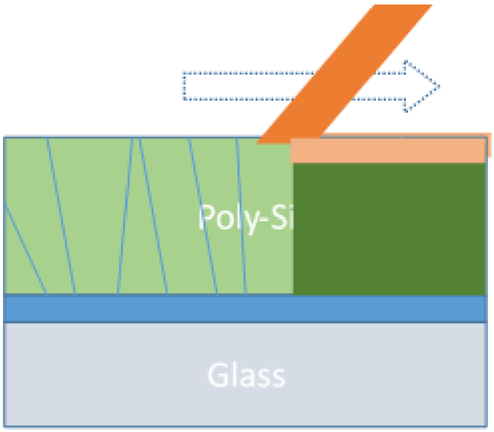

Figure 67: The side view of laser crystallization

Since the whole silicon layer is melted during the crystallization process, the thin doping layer is intermixed with the silicon layer to obtain a moderately doped absorber region. After laser crystallization process samples were etched in a polysilicon etch solution to remove the surface damages and contaminations occurred after laser scanning. The etching was done in a solution which consists of HNO_3 : HF : H_3PO_4 : H_2O (30: 1: 10: 15). After etching for 1 minute about 500 nm of the sample was etched. Finally, samples cleaned in a diluted HF (2%) solution.

6.1.3.4. Spin-on Dopant Coating

Prior to laser doping (LD), the surface of the samples were coated with phosphorus (P508) and boron (B153) containing spin-on dopant solutions which were supplied from FILMTRONICS ltd. P508 solution contains 8% phosphorus and B153 solution contains 4% boron respectively. Spin-on coating was applied in two steps for both dopant solutions: 500 RPM for 5s and 3000 RPM for 20s (Figure 68). Then samples were baked in a furnace for 5 min at 200 °C to evaporate the liquid content of the coated layers.

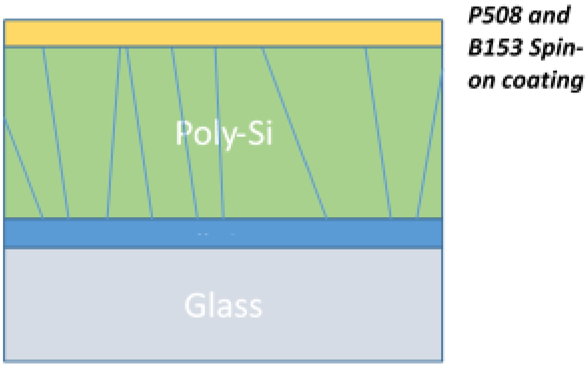

Figure 68: Spin-on dopant coating

6.1.3.5. Laser Doping (Emitter Formation)

Following the spin-on coating, LD was applied with two different laser scanning velocities with corresponding laser currents, in order to obtain different junction depths. The samples were heated on the stage at 700 °C for 15 min before doping. The scanning parameters were 1mm/s with 11.7 A current and 5 mm/s with 15 A current. After LD, samples were cleaned in a diluted (2%) HF solution to remove the surface residuals (Figure 69).

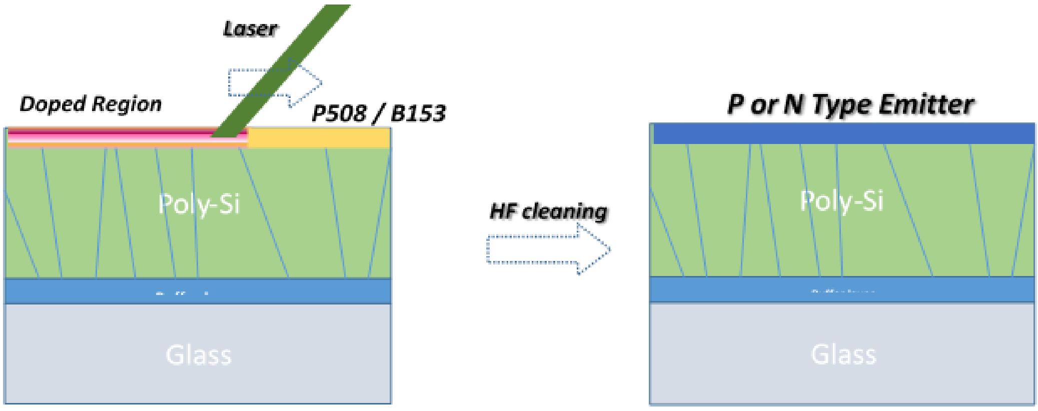

Figure 69: Laser doping process of P508 and B153 spin-on dopants.

However surfaces were partially doped to be able to check Suns V_{oc} values of the samples quickly at the beginning. Since laser has 3 cm width the doped region is 3x5 cm^2 (Figure 70).

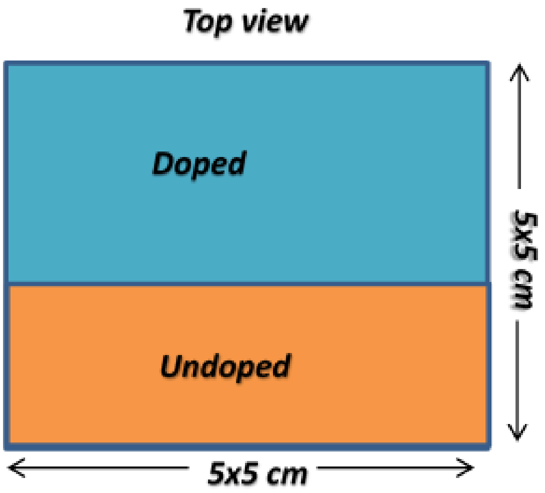

Figure 70: Top view of one of the sample after laser doping.

Using the procedure described above, two P type (with N type emitter) cells and two N type (with P type emitter) cells were produced and samples were checked in terms of V_{oc} with Suns V_{oc} measurements through doped and undoped regions. The p-type materials are coded as 51-13x and n-type materials are coded as 115-13x. Then half of the samples (one for 1mm/s and one for 5mm/s laser doped) were exposed to hydrogen (H_2) passivation. H_2 passivation was accomplished under H_2 plasma at 400 ^oC for 30 min by using 50W of plasma power.

6.1.3.6. Solar Cell Formation

Up to here there was no information about the junction depths of the solar cells. Part of the doped region was etched in polysilicon etch solution at different durations both for 1mm/s and 5mm/s laser doped samples. Here it was aimed to understand the junction characteristics (solar cell) of the samples via Suns V_{oc} measurements. After obtaining optimized etching durations according to V_{oc} values solar cell construction was followed. The round kaptons were stuck on the doped region and then the samples were etched according to the optimized durations. Each cell on the sample has an area about 0.5 cm^2 (Figure 71).

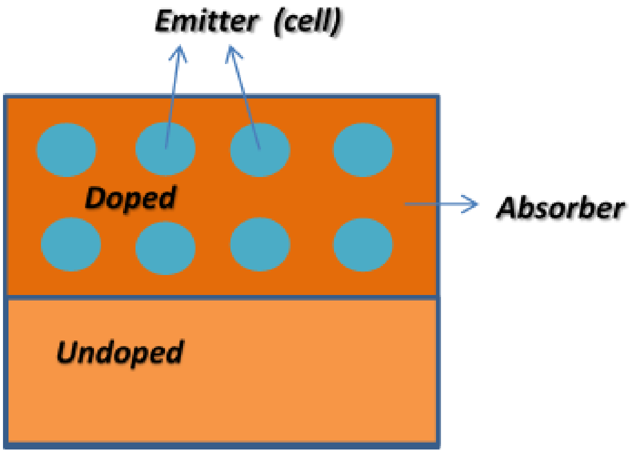

Figure 71: Cell construction on the samples after etching.

Suns V_{oc} measurement was taken every individual cell on all of the samples. Then 200 nm of Al was deposited onto the absorber region. Emitter layers were isolated by using bigger sized kaptons during the Al evaporation (Figure 72).

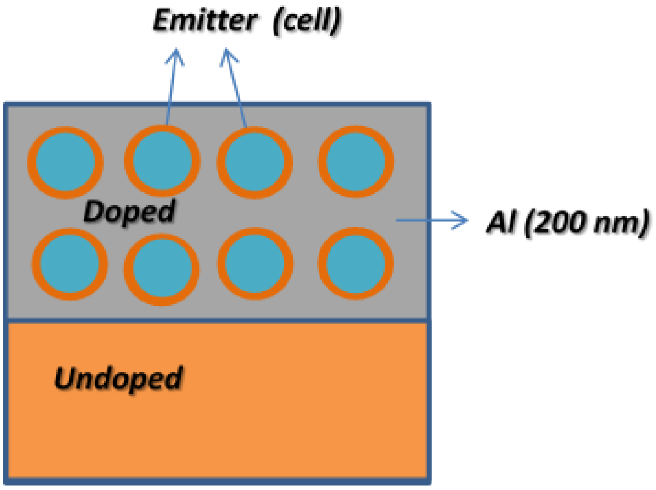

Figure 72: Top view of 5x5 cm^2 sample having Al deposition on absorber layer.

Directly after the Al deposition Suns V_{oc} measurement was carried out for each cell on each sample. However due to improper contacting the Voc values were very low. Accordingly, samples were annealed in a furnace at 200 °C for 30 min to obtain ohmic contact. As a result of the diffusion of Al into Si c-Si/Al during annealing contact resistivity around 10-20 mΩcm^{-2} [148]. I-V characteristics of the the solar cells were analyzed by using dual source (tunsten and xenon lamp) solar simulator with class AAA characteristics (Wacom Electric Co, Japan) both in substrate and superstrate configurations.

6.2. Results and Discussion

Suns Voc measurement is a quick way to understand the junction characteristic in terms of voltage. After laser doping (Figure 70), Suns V_{oc} measurement was applied through the doped and undoped region of the samples. In Table 10, the codes of the samples are given in according to their LD scanning velocities and doping types also voltage values of the samples are given before and after H_2 passivation.

Table 10: Suns V_{oc} measurement before and after H_2 passivation

Sample	**Laser Doping Velocity (mm/s)**	**Suns V_{oc} (V)**	**Suns V_{oc} (V)**
		Before H_2	After H_2
P5a	**5**	**0.468**	
P5b	**5**	0.470	**0.498**
P1a	**1**	**0.494**	
P1b	**1**	0.468	**0.489**
N5a	**5**	**0.486**	
N5b	**5**	0.483	**0.300**
N1a	**1**	**0.494**	
N1b	**1**	0.529	**0.318**

As clearly seen in Table 10, H_2 passivation improves the V_{oc} values of the p-type samples both for 1 and 5 mm/s of laser doping. However, the passivation causes a decrease in Voc for n-type samples. This may be related with the degradation of p-type emitter. Because after laser doping of n-type material the surface does not de-wet even in cleaning in HF solution. The boron solution (B153) contains oxygen, which may be the reason for hydrophilic behavior. During plasma passivation the hydrogen atoms could break the Si-O bonds and increase the deep energy states in the bangap of the material. As a result, this situation also causes the degradation of the junction.

As explained in the experimental part, the etching optimization for the cell production was carried out by using different etching durations of doped region and then measuring the V_{oc} by Suns V_{oc}. This was applied by cutting small pieces from the doped region. Each piece was exposed to polysilicon etch solution. This method is sketched in Figure 73.

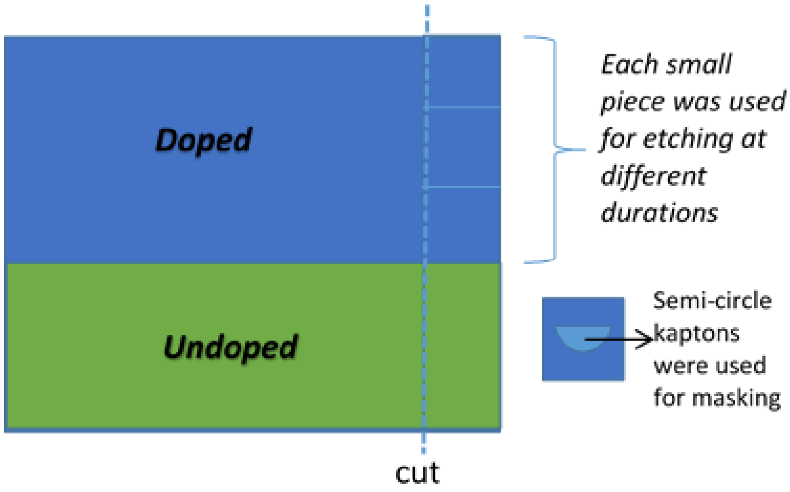

Figure 73: Etching optimization for cell preparation

Since 1 and 5 mm/s doped samples would create different junction depths, etching optimization was carried out both with 1 and 5 mm/s p and n-type samples. Three small pieces were cut out separately from samples P5a, P1b, N5b and N1b. Then half of the kapton was stuck on the small pieces to protect the emitter layer. Any individual sample character was etched at three different durations and small pieces and then the voltage values of the samples were checked by SunsV_{oc}. In Table 11 the etched samples were given with the corresponding etching durations and voltage results.

Table 11: Etching optimization of 1 and 5 mm/s doped samples and SunsV$_{oc}$ results.

Absorber/Emitter	Sample Code	Laser Emitter Doping Velocity (mm/s)	Etch time (s)	SunsV$_{oc}$ (mV)
P/N	P5a	5	120	470-458
			150	163-293-432
			180	481-470-475
	P1b	1	30	495-366-460-522
			60	508-548-550-547-517
			90	527-509-498-548-548-436-527
N/P	N5b	5	120	250-254
			150	253-251
			180	263-262
	N1b	1	30	228-230
			60	277-269
			90	242-246

Since deeper junction was expected with 5mm/s laser doping, longer etching durations were used and multiple measurements were carried ou through the emitter surface. 5 mm/s doped samples were etched for 120, 150 and 180 s however 1 mm/s doped samples were etched for 30, 60, 60 s. Suns V$_{oc}$ results show that the maximum etching durations would be enough for the expected approximate voltage results. However, the slight overetch would ensure the desired structure without compromising it. Based on this idea 5 mm/s doped samples were etched for 4.5 min and 1 mm/s doped samples were etched 2.5 min in polysilicon etch solution.

The round kaptons were then stuck on the doped regions of the samples and etching was carried out. Thus the structure which was shown in Figure 67 was obtained. The number of the cells vary depending on the sample size. Because some samples have smaller area since some part of them were used for etching optimization. After the removal of the kaptons Suns V_{oc} measurement was carried out for each cell. The results are given in Table 12 (p-type) and Table 13 (n-type).

Table 12: SunsV_{oc} results of cells on the p-type samples

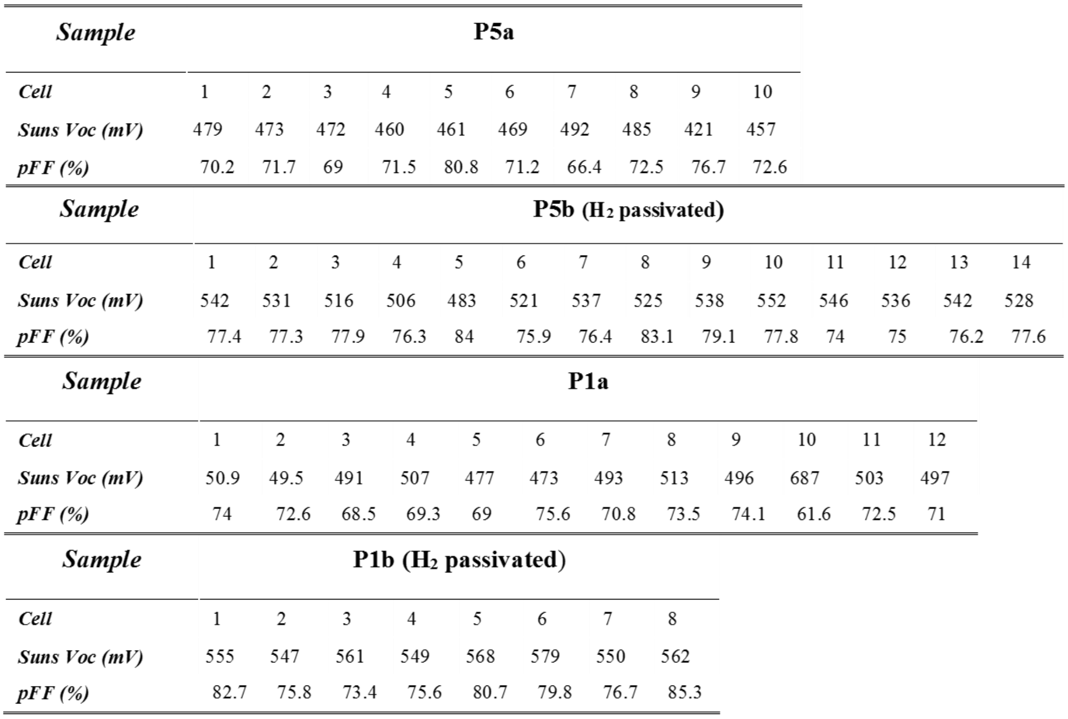

Sample	**P5a**									
Cell	1	2	3	4	5	6	7	8	9	10
Suns Voc (mV)	479	473	472	460	461	469	492	485	421	457
pFF (%)	70.2	71.7	69	71.5	80.8	71.2	66.4	72.5	76.7	72.6

Sample	**P5b** (H2 passivated)													
Cell	1	2	3	4	5	6	7	8	9	10	11	12	13	14
Suns Voc (mV)	542	531	516	506	483	521	537	525	538	552	546	536	542	528
pFF (%)	77.4	77.3	77.9	76.3	84	75.9	76.4	83.1	79.1	77.8	74	75	76.2	77.6

Sample	**P1a**											
Cell	1	2	3	4	5	6	7	8	9	10	11	12
Suns Voc (mV)	50.9	49.5	491	507	477	473	493	513	496	687	503	497
pFF (%)	74	72.6	68.5	69.3	69	75.6	70.8	73.5	74.1	61.6	72.5	71

Sample	**P1b (H_2 passivated)**							
Cell	1	2	3	4	5	6	7	8
Suns Voc (mV)	555	547	561	549	568	579	550	562
pFF (%)	82.7	75.8	73.4	75.6	80.7	79.8	76.7	85.3

Table 13: SunsV$_{oc}$ results of cells on the n-type samples

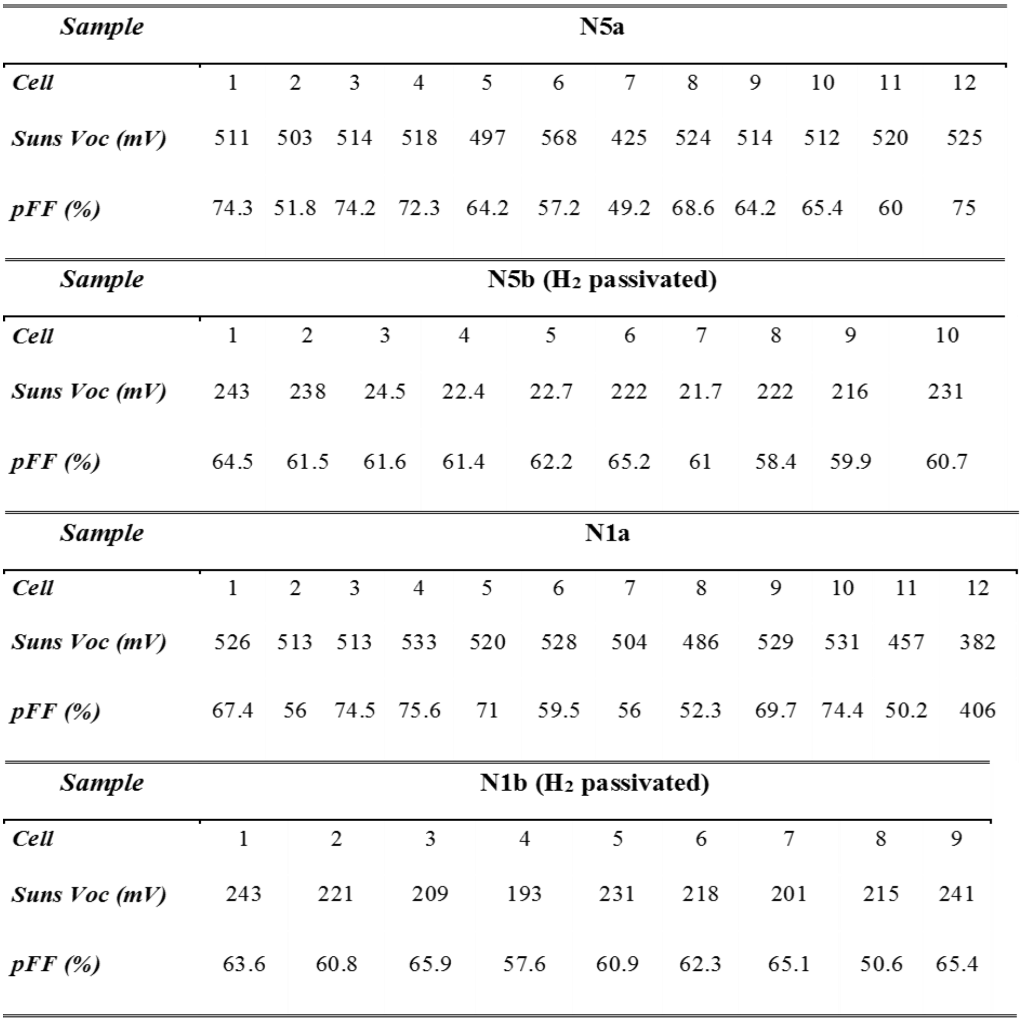

Sample	**N5a**											
Cell	1	2	3	4	5	6	7	8	9	10	11	12
Suns Voc (mV)	511	503	514	518	497	568	425	524	514	512	520	525
pFF (%)	74.3	51.8	74.2	72.3	64.2	57.2	49.2	68.6	64.2	65.4	60	75

Sample	**N5b (H_2 passivated)**									
Cell	1	2	3	4	5	6	7	8	9	10
Suns Voc (mV)	243	238	24.5	22.4	22.7	222	21.7	222	216	231
pFF (%)	64.5	61.5	61.6	61.4	62.2	65.2	61	58.4	59.9	60.7

Sample	**N1a**											
Cell	1	2	3	4	5	6	7	8	9	10	11	12
Suns Voc (mV)	526	513	513	533	520	528	504	486	529	531	457	382
pFF (%)	67.4	56	74.5	75.6	71	59.5	56	52.3	69.7	74.4	50.2	406

Sample	**N1b (H_2 passivated)**								
Cell	1	2	3	4	5	6	7	8	9
Suns Voc (mV)	243	221	209	193	231	218	201	215	241
pFF (%)	63.6	60.8	65.9	57.6	60.9	62.3	65.1	50.6	65.4

Voltage values in Table 12 and 13 shows that etching durations for the cells seem to be sufficient. Suns V$_{oc}$ also gives us the pseudo fill factor (pFF). In Table 12 it is clear that hydrogenation increases the voltage values both for 1 and 5 mm/s of doping and voltage values over 500 mV has been achieved. However for n-type material hydrogenation significantly decreases the voltage, which was also shown just after the doping process.

Following the Suns V$_{oc}$ measurements an Al layer was deposited onto the absorber layer for all of the samples.The cells were checked by Suns V$_{oc}$ immediately after metal deposition. However, the voltage results were very low with respect to the results before Al deposition. Some cells presented voltage values below 200 mV. The reason of this voltage decline was due to the high resistance at the metal and silicon interface. In order to overcome this problem the samples were annealed at 200 °C for 30 min to obtain a better ohmic contact. Then the voltage values of the samples were checked by Suns V_{oc}. Notable increment of the voltage values for all of the samples has been observed. The new results are shown in Table 14 and Table 15.

Table 14: SunsV_{oc} results of cells on the p-type samples after Al deposition and annealing

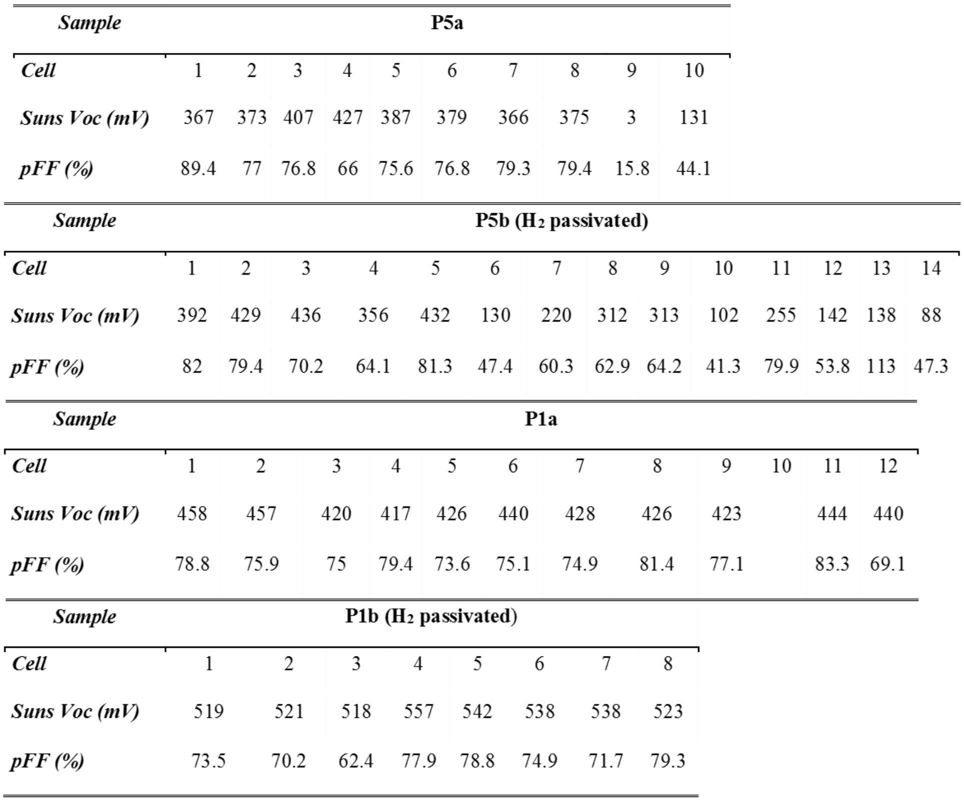

Sample	**P5a**									
Cell	1	2	3	4	5	6	7	8	9	10
Suns Voc (mV)	367	373	407	427	387	379	366	375	3	131
pFF (%)	89.4	77	76.8	66	75.6	76.8	79.3	79.4	15.8	44.1

Sample	**P5b (H_2 passivated)**													
Cell	1	2	3	4	5	6	7	8	9	10	11	12	13	14
Suns Voc (mV)	392	429	436	356	432	130	220	312	313	102	255	142	138	88
pFF (%)	82	79.4	70.2	64.1	81.3	47.4	60.3	62.9	64.2	41.3	79.9	53.8	113	47.3

Sample	**P1a**											
Cell	1	2	3	4	5	6	7	8	9	10	11	12
Suns Voc (mV)	458	457	420	417	426	440	428	426	423		444	440
pFF (%)	78.8	75.9	75	79.4	73.6	75.1	74.9	81.4	77.1		83.3	69.1

Sample	**P1b (H_2 passivated)**							
Cell	1	2	3	4	5	6	7	8
Suns Voc (mV)	519	521	518	557	542	538	538	523
pFF (%)	73.5	70.2	62.4	77.9	78.8	74.9	71.7	79.3

Table 15: SunsV$_{oc}$ results of cells on the n-type samples after Al deposition and annealing

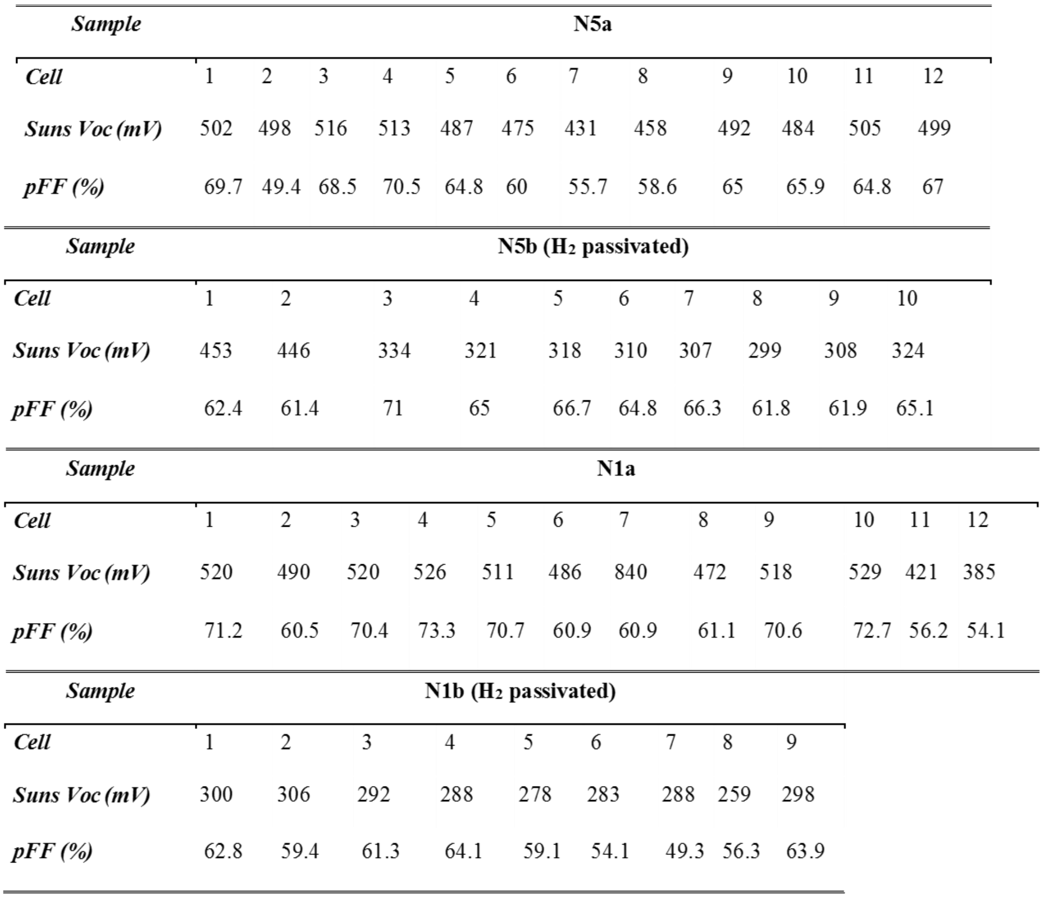

Sample	N5a											
Cell	1	2	3	4	5	6	7	8	9	10	11	12
Suns Voc (mV)	502	498	516	513	487	475	431	458	492	484	505	499
pFF (%)	69.7	49.4	68.5	70.5	64.8	60	55.7	58.6	65	65.9	64.8	67

Sample	N5b (H_2 passivated)									
Cell	1	2	3	4	5	6	7	8	9	10
Suns Voc (mV)	453	446	334	321	318	310	307	299	308	324
pFF (%)	62.4	61.4	71	65	66.7	64.8	66.3	61.8	61.9	65.1

Sample	N1a											
Cell	1	2	3	4	5	6	7	8	9	10	11	12
Suns Voc (mV)	520	490	520	526	511	486	840	472	518	529	421	385
pFF (%)	71.2	60.5	70.4	73.3	70.7	60.9	60.9	61.1	70.6	72.7	56.2	54.1

Sample	N1b (H_2 passivated)								
Cell	1	2	3	4	5	6	7	8	9
Suns Voc (mV)	300	306	292	288	278	283	288	259	298
pFF (%)	62.8	59.4	61.3	64.1	59.1	54.1	49.3	56.3	63.9

After annealing of Al, it is clear from Table 14 and 15, an increase in V_{oc} values can be seen (with respect to the values before annealing of Al). As shown before the average cell results of n-type H_2 passivated samples have low V_{oc} values which was discussed before. As a result, the highest V_{oc} values are summarized in Table 16

Table 16: Highest V_{oc} of the samples

Absorber/Emitter	**Annealing**	**Highest Voc (mV)**			
		1 mm/s (shallow junction)		5 mm/s (deep junction)	
		No H_2	H_2	No H_2	H_2
p/n	Before	513	**579**	492	552
	After	458	557	427	436
n/p	Before	**533**	243	525	243
	after	526	306	516	453

According to the V_{oc} results, 1 mm/s of doping (shallow junction) yields the highest V_{oc} for both of the material types. H_2 passivation increases the V_{oc} for p-type material however it causes a decline for n-type material. H_2 passivated p-type material presents 579 mV V_{oc} and n-type material gives 533 mV of V_{oc} without passivation. N-type material seems to be more advantageous after passivation if the degradation problem can be overcome.

The I-V characteristics were analyzed by solar simulator measurements, however, some selected ones are given here. In Figure 74 and Figure 75 solar simulator results are given with the corresponding cell number written on the graphs. Both superstrate and substrate configurations were measured.

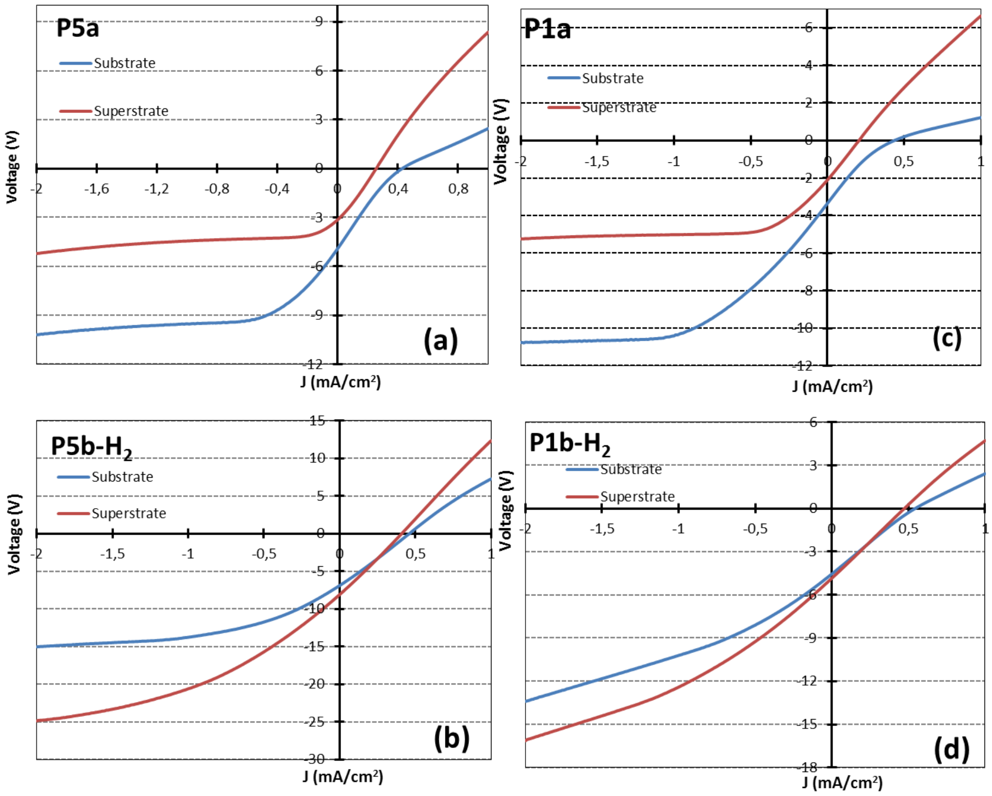

Figure 74: Solar simulator results of the selected cells on p-type samples 5 mm/s doped (a), (b) and 1 mm/s doped (c), (d)

Solar simulator results in Figure 74 also shows us that H_2 passivation increases the V_{oc} values for both 1 mm/s and 5 mm/s doping in superstrate configuration. This is also true for substrate condition but 1 mm/s doped sample (c,d) has very small increment, in superstrate configuration, the increment is more than substrate version. Also in superstrate condition 5 mm/s doping has more increment than 1 mm/s doping after H_2 passivation. When the current values compared there is a notable increment in superstrate configurations. When the light enters from the glass (superstrate) the light has longer way to reach the junction region than substrate configuration. In other words, the probability of a carrier to reach to the junction region is higher in substrate configuration, so the passivation has more influence in superstrate condition that it shifts the current significantly.

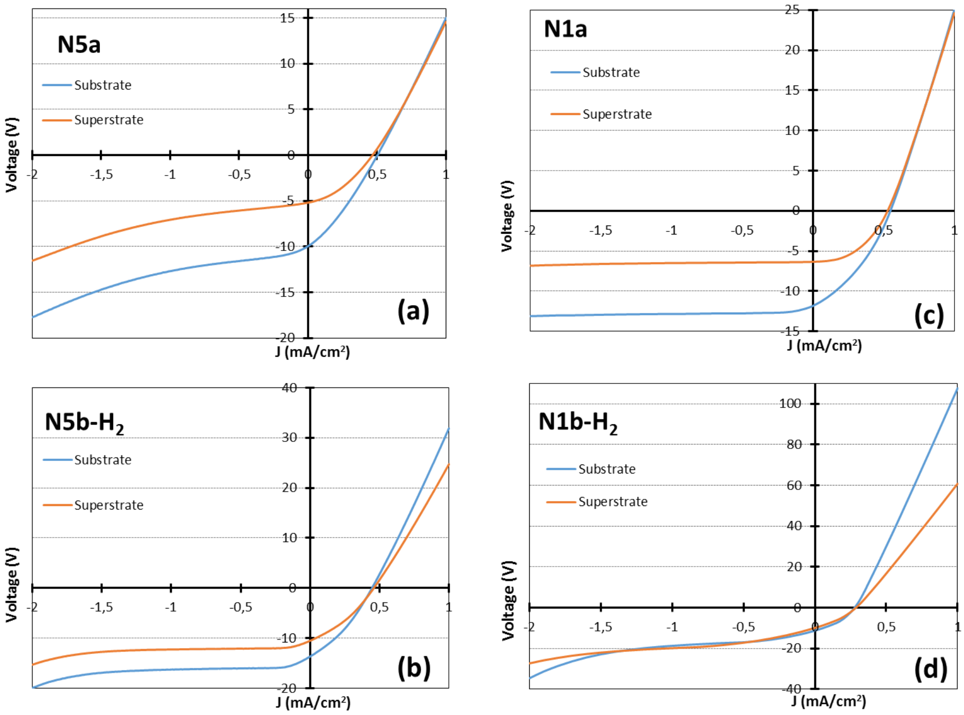

Figure 75: Solar sim results of the selected cells on n-type samples 5 mm/s doped (a), (b) and 1 mm/s doped (c), (d)

In Figure 75, the effect of H_2 passivation can be seen both for 5 mm/s (a,b) and 1 mm/s (c,d) doping that passivation causes a decline in V_{oc} of the cells. This effect can be notably seen in 1 mm/s doped samples than 5 mm/s doped samples because 1 mm/s doped samples have the junction region closer to the surface which means that more H_2 can reach to the junction region and can create more deep energy states by breaking Si-O bonds as discussed before. Also it seems that the current increment is more in superstrate configuration than substrate condition after H_2 passivation. This shows that the H_2 has a positive effect on n-type absorber layer.

In general n-type samples show better solar cell characteristics than p-type samples in terms of fill factor and current. The V_{oc} values are also comparable. It seems that the hydrogenation degrades the emitter regions of the n-type materials. The current increment shows that the absorber layer is passivated well. However current density measurements may not be reliable enough as it was done using a simple probe which has a very small surface area. The metallization of the emitter surface probably would increase the current amount. But the effect of hydrogenation can be understood clearly without metal contacts of the emitter surface. In Figure 76a, the photograph of the solar cells are given. As mentioned before, some portion of each sample is not doped and the grains can be clearly seen in undoped regions. The round shaped solar cells are located on the doped side of the substrates. There is no emitter metallization which inhibites the proper current collection. Al layer is on the absorber layer. Moreover, in Figure 76b, the same photograph was taken after the samples were illuminated from the glass side, which gives details about the crack in poly-Si films. This is another possible reason for improper current collection from emitter regions.

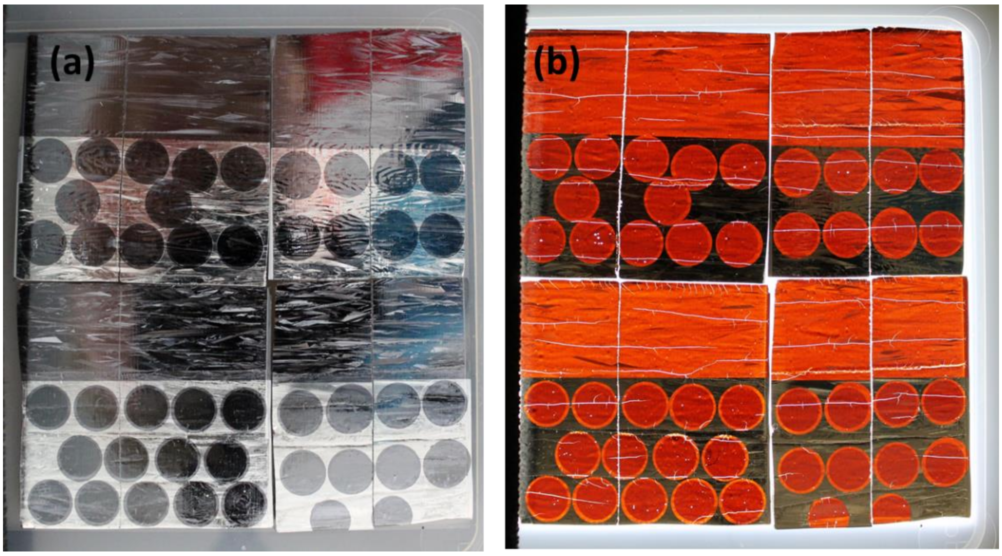

Figure 76: Picture of the final version of solar cells. Normal mode (a) and samples are illuminated from glass side (b)

In the light of given results, the solar simulator analysis presented a maximum efficiency of 2.9 % from sample N5b in superstrate configuration. The sample has Fill Factor of 41.46 %, current density of 15 mA and 454 mV of open circuit voltage respectively. A good current collection without cracks in the samples can be expected to increase the efficieny of solar cells.

In Figure 77 and 78 external quantum efficiency (EQE) measurements of the selected cells, which are analysed in solar simulator measurements, are given. The analysis was accomplished both for substrate and superstrate cases. Substrate and superstrate configurations are shown on the right hand side of Figures 77a and 77b. The response of the cells vary with respect to the incident light direction because the junction region is closer to the emitter side surface.

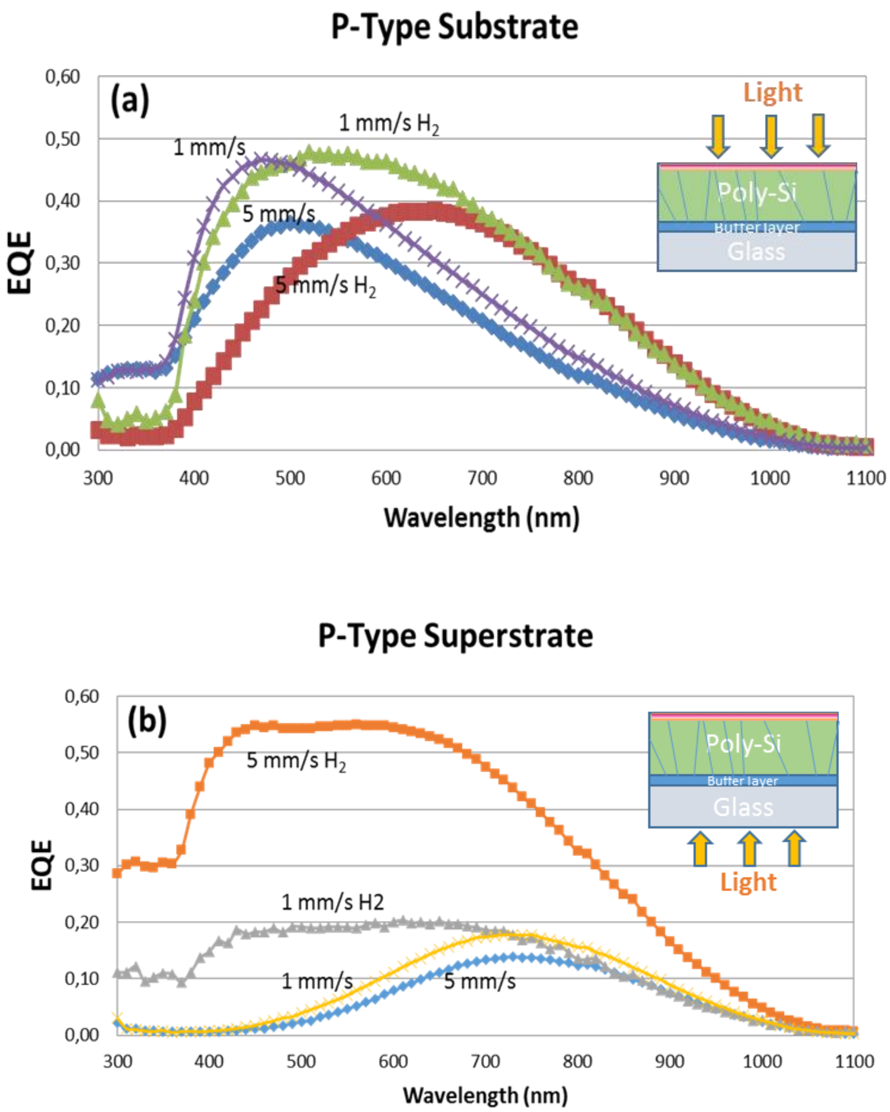

Figure 77: External Quantum Efficiency (EQE) measurement of p-type samples both in substrate (a) and superstrate (b) configurations

EQE results shown in Figure 77 presents the effect of hydrogenation. From Figure 77a, it can be understood that H_2 passivation decreases the emitter diffusion length (short wavelenths) which is due to the increase in surface recombination. However the broadening after H_2 passivation for the both doping conditions demonstrates the increase of base diffusion length. 1 mm/s doped samples have higher EQE values because they have shallow junction than 5 mm/s doped samples. In Figure 77b the unpassivated samples have small response at higher wavelengths because the high energy photons are absorbed far away from the junction region in superstrate configuration and the carriers can not reach to the junction effectively. However, after H_2 passivation the EQE response increases due to the saturation of defects. Besides, 5 mm/s doped sample has significantly large response because the junction region is closer to the glass interface than 1 mm/s doped sample. In other words recombination is more dominant in 1 mm/s doped sample.

In both cases, hydrogenation increases the base diffusion length but not as much as in p type case. After hydrogenation, EQE for short wavelength values (300-400) decreases (emitter diffusion length). This may be due to the increase of surface recombination after H_2 plasma.

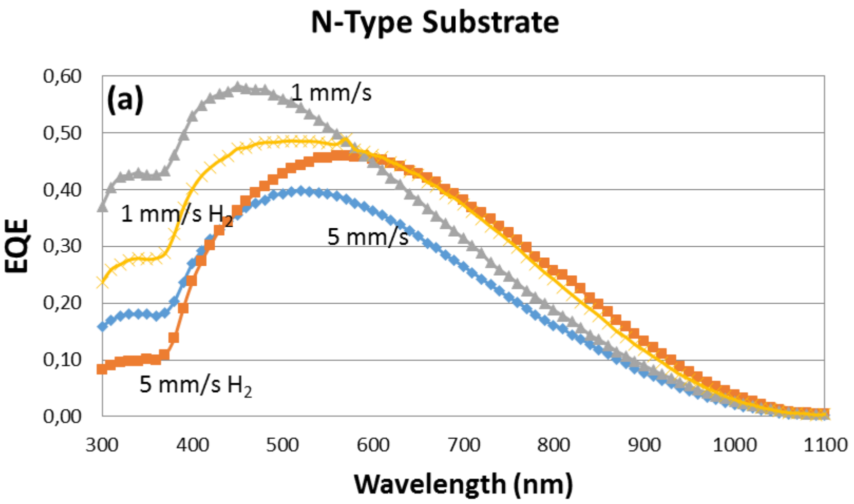

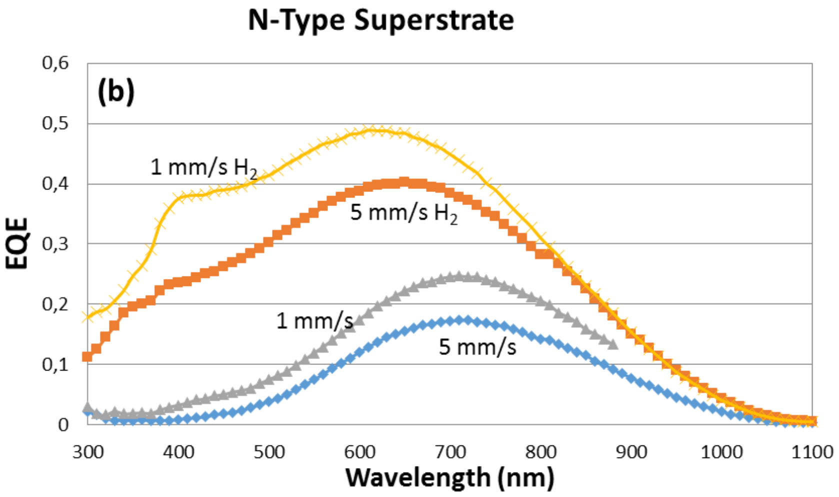

Figure 78: External Quantum Efficiency (EQE) measurement of n-type samples both in substrate (a) and superstrate (b) configurations

For the n-type case the decline of emitter diffusion length can be seen after H_2 passivation (Figure 78a) like in p-type case. Also hydrogenation increases the base diffusion length but not as much as in p type case. For n-type materials the thickness of the emitter region dominates the EQE signal. In Figure 78b before and after H_2 passivation 1 mm/s doping has better response. Since the p-type emitter region is degraded and thicker in 5 mm/s doped samples, 1 mm/s doped samples have less recombination sites especially at higher wavelengths. But in general the H_2 passivation works well for both doping type.

CHAPTER 7

CONCLUSIONS

In this thesis, a comprehensive study on the processing of polycrystalline silicon thin films was presented. A variety of crystallization schemes were employed, and the structural and electronic properties of the resulting poly-Si thin films were characterized. The following conclusions were drawn throughout the course of this research project:

Metal Induced Crystallization (MIC) of amorphous silicon was first investigated by Au metal. Production of Gold Nanoparticles (AuNPs) on Aluminum doped Zinc Oxide (AZO) via annealing thin Au films at 500 ^{o}C was first studied as a crystallization agent for a-Si. It was shown that AuNPs with larger diameters and wider spacing can be obtained on AZO by increasing the pre-anneal Au film thickness from 5nm to 15nm. Further analysis is required for precise control of the distribution of AuNP size and separation distance. The crystallization of Si was studied by annealing a-Si films grown on 'larger' AuNPs (with a pre-anneal film thickness of 15nm) at various temperatures and durations. No indication of crystallization was observed at 500^{o}C for 12h, whereas more than 60% crystallinity was achieved for 600^{o}C annealing for 2h. Further annealing at 600^{o}C resulted in a small increase in crystallinity (approximately 70% after 12h), suggesting that the amount of Au limited the crystallization percentage. The sample without AuNPs showed no crystallization. It seems that, the full crystallization was not achieved even annealing at 600 ^{o}C for 12h with AuNPs. These results indicate that MIC of a-Si via AuNPs works well although the metal amount is very small. However, it is believed that the increment of metal amount can increase the crystallization fraction. As stated before, the NP formation is another issue since the initial structure/properties of Au thin film can change the de-wetting conditions. It is known that Au induced silicon is not suitable for solar cell applications due to Au contamination. However, Au was introduced to see the MIC of a-Si before the observation of effect of Al as the Aluminium Induced Crystallization (AIC) is the core of this thesis.

In Chapter 3.2 AIC of a-Si was investigated. At first, AIC was handled with buffer layer optimization. Different types of SiN_x buffer layers were deposited by changing the deposition conditions. As the NH_3/SiH_4 fraction decreases, it was observed that the refractive index of the layers were approaching 2, which is a well-accepted value for SiN_x, Besides, one type of AZO layer was deposited as a buffer layer. Then, AIC of a-Si on these buffer layers were processed and the effects of the buffer layers on the final poly-Si layers were observed. The poly-Si films were obtained after annealing of a-Si/Al/ SiN_x(AZO)/glass stack at 500 °C for 5 h. The Raman analysis demonstrated that the samples are fully crystallized, and, crystallinity is independent of the buffer layer content. The FWHM values of the samples are quite close to each other and have no notable difference with respect to c-Si FWHM. As a result of XRD analysis, the crystallographic orientation factor Θ_{hkl} (%) was defined as <111>, <311> and <100> spectral peaks for all samples and <100> orientation has a fraction of about 60-70 %. Among the SiN_x based samples the largest crystallite size of 48.5 nm was obtained for sample “d” which has NH_3/SiH_4 fraction of 2. The larger crystallite size with lower NH_3/SiH_4 fraction was attributed to the high silicon content in the SiN_x layer where silicon atoms can form clusters and nanoparticles. Therefore, the silicon crystallization can be supported by the buffer layer after the nuclei grow enough to touch the buffer layer. The increase of RF deposition power creates lower Si content in SiN_x which forms smaller clusters as well as smaller silicon crystallite size. EBSD results show that the grain sizes are up to 20-25 μm. Furthermore, EBSD maps confirm that the amount of silicon content in SiN_x layer affects the poly-Si grain size. Besides, AFM analysis of SiN_x layers showed that high NH_3/SiH_4 fraction leads to much rough surface which increases the number of Si nucleation sites and results in smaller grain size than Si growth on smoother surface. The resistivity of Poly-Si films was measured by Four Point Probe (FPP) and resistivity of the SiN_x based samples were found to be around 0.1 Ωcm which is quite low compared to the c-Si (1-10 Ωcm) due to Al doping. These results indicate that MIC of a-Si via AuNPs works well although the metal amount is very small. Furthermore, the resistivity was also deduced by *I-V* characteristic under dark and illuminated conditions and it was calculated as 0.087 Ωcm by which is close to the result of 0.1 Ωcm obtained by FPP technique. The high conductivity indicates that poly-Si films are highly Al doped. The SiN_x deposited with precursor fraction (NH_3/SiH_4) of 2 with 100 W PECVD power was the standard deposition condition of buffer layer for the further experiments.

In Chapter 3.2 of this thesis, the kinetics of AIC process is discussed. Different than first AIC annealing temperature, the layer exchange annealing was carried out between 450 ^oC and 525 ^oC. It was observed that rise in the annealing temperature increases the crystallization rate while it decreases the grain size of the films. Annealing at 450^oC results in poly-Si films with grain sizes of tens of micrometers. Activation energy associated with the growth of Si crystallites was determined as 1.93 eV, which correlates well with previous studies. Raman spectroscopy on the final AIC poly-Si layers shows a slight increase in c-Si peak (near 520 cm^{-1}) with increasing annealing time, which is likely related to the increase in grain boundary fraction of the films. The residual Al that is left in the final poly-Si layer is around $9x10^{19}$ cm^{-3}, as measured by SIMS. However Hall effect measurements showed that the active Al is approximately two orders of magnitude smaller than the total Al. Besides, the AlO_x membrane was studied in terms of different oxidation durations of Al layer. The oxidation was carried out by exposure of Al layer to native air for 10 min, 24 h and 1 week. Since 10 min of exposure forms a thinner oxide layer with respect to 24 h and 1 week of exposure, the crystallization is completed at the end of 60 min annealing, however, the crystallization for 24 h and 1 week exposed samples just starts around 60 min of annealing. There was no difference in crystallization kinetics between 24 h and 1 week exposed samples. Besides, the grain size of 10 min exposed sample is smaller than 24 h and 1 week exposed samples since short oxidation duration results thinner oxide layer than longer oxidation duration which increases the number of possible nucleation sites. These results are indicative of the fact that the majority of the Al oxidation occurs within the first day of exposure.

SPE experiments were conducted on the AIC poly-Si seed layers that are obtained after annealing at 450 ^oC, 500 ^oC and 525 ^oC. The SPE annealing was done at 600 ^oC. The majority of the crystallization was done within the first 210 min. for the sample with

450^{o}C annealed seed, 360 min. for the sample with 500^{o}C annealed seed, and 660 min. the sample with 525^{o}C annealed seed. These results provide a possible explanation that the amount of grain boundaries on the seed layer diminishing the rate of crystallization. Poly-Si/a-Si interface on the 450 ^{o}C annealed seed has a better promotion for SPE since the grain size of the 450 ^{o}C annealed seed is larger than 500 ^{o}C and 525 ^{o}C annealed seeds. However, due to residual Al detected on the poly-Si surface, an Al etching procedure was carried out prior to a-Si deposition. Finally, highly <100> oriented SPE layer was obtained. However, a control sample that was prepared without the Al etch step did not result in epitaxial growth.

In Chapter 4, the process modifications on the AIC poly-Si layer are given. The effect of Al annealing on the AIC process was observed. Two identical sample sets were prepared, where the only difference between two sets is the vacuum annealing of the Al/SiN_x/glass stack prior to a-Si deposition. These samples are labelled as pre-annealed and control samples. The optical microscope images of 420 ^{o}C annealing of both samples indicate that the crystallization rate is higher in control sample which brings in mind that control sample has thinner AlO_x membrane. However, XPS results indicate that, control sample has thicker AlO_x layer than pre-annealed sample. XPS of pre-annealed spectra show a higher oxide ratio with respect to the control sample when the oxide/metal peak ratios for the Al2p of the samples are compared. This indicates that pre-annealed sample has a thin yet heavily oxidized AlO_x layer, due to Al annealing, which suppresses the crystallization rate. Meanwhile, the EBSD analysis of the Al layers of the pre-annealed and control samples show that pre-annealed sample has micrometer sized Al grains. However, control sample shows no detectable grains. This means that control sample has quite a lot grain boundaries in the Al layer. The high density of grain boundary increases the possible nucleation sites since Si diffusivity is enhanced in the Al grain boundaries compared to bulk Al. The EBSD images of the final poly-Si layers confirm these explanations. The average poly-Si grain size of pre-annealed sample is larger than control sample. Besides, the <111> silicon grain orientation is enhanced by Al annealing.

In Chapter 5, the different Si deposition techniques of E-beam and PECVD are compared. For e-beam samples, during the silicon deposition, room temperature (E-

RT) and 420 ^{o}C substrate temperatures were used. In addition, the PECVD samples were deposited at room temperature, however, SiH_4:H_2 ratio was varied as 1:9 (P-9) and 1:29 (P-29). The samples were annealed in a furnace at 420 ^{o}C and 450 ^{o}C. Prior to furnace annealing, the optical microscopy images show that E-HT sample has already grown dendritic crystalline structures due to high substrate temperature. It was observed that both 420 ^{o}C and 450 ^{o}C furnace annealing the crystallization rate of e-beam samples are higher than PECVD samples. Moreover, E-HT samples show higher crystallization rate than E-RT samples and P-9 samples has higher rate than P-29 samples, respectively. However, it was realized that P-9 sample has large voids besides the crystalline regions. These results indicate that the hydrogen has a great effect on lowering the crystallization rate. The EBSD images taken from 450 ^{o}C annealed samples show that average final poly-Si grain size has an order of P-29 > P-9 > E-RT > E-HT as expected. Before furnace annealing of the samples, the Raman spectroscopy and FTIR analysis were carried out in order to understand the differences in crystallization kinetics. Transverse acoustic (TA) and transverse optical (TO) modes of Raman spectra at 150 and 480 cm^{-1} are crucial for the bond structure of amorphous silicon. Moreover, the width of TO peak is proportional to the short range disorder and I_{TA}/I_{TO} ratio indicates a higher intermediate range disorder. According to Raman spectra of the samples, the E-RT sample has the highest short range disorder. Based on the I_{TA}/I_{TO} ratios, the intermediate range disorder of the samples can be given as E-RT > E-HT > P-9 > P-29. The higher order of the PECVD samples can be explained by the presence of hydrogen compared to e-beam samples which is attributed to the strain relieving effect of hydrogen. E-RT sample has higher disorder than E-HT. However, E-RT sample has larger Si grain size than E-HT. This situation was explained by the in-situ nucleation process which occurred during the a-Si deposition. The Si-H bonding structures of PECVD samples were investigated by FTIR. At first glance, the presence of SiH_2 bonding was observed in P-9 sample with the two peaks around 800-900 cm^{-1}. The low stretching mode near 2000 cm^{-1} is related with SiH bonding which was observed for P-29. Another indication of SiH_2 bonding for P-9 sample was high stretching mode near 2100 cm^{-1}. As a result, rise in the hydrogen amount dominates the SiH bonding in amorphous silicon which leads to a more stable form. The hydrogen bonding in SiH_2 is weaker than SiH. The bonds of SiH_2 can be easily broken in a furnace annealing which was the reason of voids in P-9 sample. Consequently, it was observed that SiH based amorphous silicon is more resistant and stable than SiH_2 based amorphous silicon.

In Chapter 6, the laser induced crystallization of amorphous silicon was studied. Continuous wave CW diode laser was used for the crystallization and doping of Si layers. Both n-type (has p-type emitter) and p-type (has n-type emitter) solar cells were constructed. The doping of the cells was carried out by laser scanning velocity of 1 mm/s and 5 mm/s after spin-on coating of dopant solutions. Since 5 mm/s doping was done with higher power, deeper junction depth was expected. Each doping type has two different doping velocities and H_2 passivation. After doping, the V_{oc} values were checked by Suns V_{oc} measurements. The V_{oc} values were over 460 mV and it was highest for the n-type 1mm/s doped sample as 529 mV. After H_2 passivation, the V_{oc} values of p-type samples (both 1 and 5 mm/s doped samples) indicate a rise in V_{oc} around 20 mV. However, H_2 passivation degrades the V_{oc} of n-type samples down to around 300 mV. This situation was attributed to the creation of deep energy levels due to Si-O bond breaking by H atoms since boron solution contains oxygen. After mesa cell construction (etching, metallization of absorber layer), it was observed that 1 mm/s of doping yields the highest V_{oc} values both for n-type and p-type materials. H_2 passivated p-type material yields 579 mV V_{oc} and n-type material gives 533 mV of V_{oc} without passivation. N-type material seems to be more advantageous after passivation if the degradation problem can be overcome. Solar simulator measurements of the selected cells also show the rise in Voc after passivation. The difference between two types of doping (1 and 5 mm/s) was observable in terms of current density when the analysis were carried out for substrate and superstrate modes. 1 mm/s and 5 mm/s doping leads to different junction depths. When the current densities were checked, it was observed that H_2 passivation has better effect for superstrate configurations, because the light has a longer path to reach to the junction region. Moreover, the increment of current density for 1 m/s doping is higher than 5 mm/s doped samples since the junction is lower in 1 mm/s case in superstrate configuration. For n-type case, as expected, H_2 passivation leads to a decline in V_{oc} like as observed in Suns V_{oc} case. Furthermore, this decline is more notable for the 1 mm/s doping since the junction is closer to the surface with regard to 5 mm/s doped sample. When the junction is close to the surface, the possibility of H_2 degradation increases. However, there is an increase in current density for all n-type samples, which indicates that absorber region is well passivated. EQE measurements showed that, H_2 passivation leads to a decline in emitter diffusion length of the whole cells due to the increase in surface recombination. In contrast, the passivation increases the base diffusion length which indicates that passivation works well for absorber layer. Solar simulator results presented a maximum efficiency of 2.9 % for n-type 5 mm/s doped sample in superstrate configuration. Higher efficiency values are expected with a proper current collection, good metallization and solving the cracking problems of Si films.

REFERENCES

[1] "International Energy Agency (IEA) World Energy Outlook 2015, https://www.iea.org/Textbase/npsum/WEO2015SUM.pdf.

[2] Fraunhofer Institute for Solar Energy Systems, Photovoltaic Report 2016, https://www.ise.fraunhofer.de/en/downloads-englisch/pdf-files-englisch/photovoltaics-report-slides.pdf.

[3] R. W. Becquerel, J. Chem. Phys. 32 (1960) 1505–1514.

[4] P. Gevorkian, Sustainable energy systems engineering: the complete green building design resource, McGraw Hill Professional (2007).

[5] "The Nobel Prize in Physics 1921: Albert Einstein", Nobel Prize official page, Web: http://www.nobelprize.org/nobel_prizes/physics/laureates/1921/.

[6] R. Ohl. Light sensitive electric device. US Patent240252, filed 27 March 1941. Light-sensitive electric device including silicon. US Patent 2443542, filed 27 May 1941.

[7] "April 25, 1954: Bell Labs Demonstrates the First Practical Silicon Solar Cell" American Physical Society News, Web: https://www.aps.org/publications/apsnews/200904/physicshistory.cfm.

[8] K. Masuko, M. Shigematsu, T. Hashiguchi, D. Fujishima, M. Kai, N. Yoshimura, T. Yamaguchi, Y. Ichihashi, T. Yamanishi, T. Takahama, M. Taguchi, E. Maruyama, S. Okamoto, IEEE J. Photovolt. 4 (2014) 1433 – 1435.

[9] S. Zhang, X. Pan, H. Jiao, W. Deng, J. Xu, Y. Chen, P. Altermatt, Z. Feng, PJ. Verlinden, IEEE J. Photovolt. 6 (2016) 145 – 152.

[10] "Rest in Peace: The List of Deceased Solar Companies".GreenTechMedia (2014) Web: http://www.greentechmedia.com/articles/read/Honoring-the-fallen-solar-soldiers.

[11] "NovaSolar, Formerly OptiSolar, Leaving Smoking Crater in Fremont" GreenTechMedia (2012), Web: http://www.greentechmedia.com/articles/read/NovaSolar-the-former-OptiSolar-Leaving-Smoking-Crater-in-Fremont.

[12] T. Baba, T. Matsuyama, T. Sawada, T. Takahama, K. Wakisaka, S. Tsuda, S. Nakano, Polycrstalline Silicon Thin-film Solar Cell Prepared by Solid Phase Crystallization (SPC) Method, IEEE Photovoltaic Specialists Conference , 2 (1994), pp. 1315-1318..

[13] T. Kamins, Polycrystalline Silicon for Integrated Circuit Applications, Kluwer Academic, Boston (1998)

[14] P. Woditsch, W. Koch, “Solar grade silicon feedstock supply for PV industry,” Sol. Energy Mater. Sol. Cells, 72, (2002), 11–26.

[15] B. Prior, C. Campbell, “Polysilicon 2012–2016: Supply, demand and implications for the global PV industry,” GMT Res., Boston, MA, USA, 2012.

[16] Star Solar “Difference between monocrystalline polycrystalline and Amorphous thin film solar cell” Web.http://www.pvsolarchina.com/difference-between-monocrystalline-polycrystalline-and-amorphous-thin-film-solar-cell.html, last accessed on 14/08/2011.

[17] M. E. Crowder, T. O. Sedgewick, J. Electrochem. Soc. 119, (1972), 1565.

[18] T. Kamins, J. Appl. Phys. 42, (1971), 4357-4365.

[19] J. Y. W. Seto, J. Appl. Phys. 46, (1975), 5247-5254.

[20] P. A. Basore, Simplified processing and improved efficiency of crystalline silicon on glass modules, Proc. 19th European Photovoltaic Solar Energy Conference, 455–458 (2004).

[21] G. Beaucarne, A. Slaoui, “Thin Film Polycrystalline Silicon Solar Cells”, In: Thin Film Solar Cells, John Wiley & Sons (2006).

[22] A. Slaoui, P. Siffert, “Polycrystalline Silicon Films for Electronic Devices”, In: Silicon-Evolution and Future of a Technology, Eds.: P. Siffert, E. Krimmel, Springer, 2004.

[23] M. L. Terry, A. Straub, D. Inns, D. Song, A. G. Aberle, Appl. Phys. Lett. 86 (2005), 172108.

[24] L. Haji, P. Joubert, J. Stoemenos, N. A. Economou, J. Appl. Phys. 75, (1994), 3944.

[25] P.A. Basore, in: Proceedings of the 19th European Photovoltaic Solar Energy Conference, WIP, Munich, 2004, p. 455.

[26] M.J. Keevers, T.L. Young, U. Schubert, M.A. Green: ‘10% efficient CSG minimodules’, Proc. of the 22nd European Photovoltaic Solar Energy Conference, Milan, Italy (2007) 1783.

[27] T. Baba, T. Matsuyama, T. Sawada, T. Takahama, K. Wakisaka, S. Tsuda, MRS Symp. Proc. 358 (1995) 895.

[28] E. S. Cielaszyk, K. H. R. Kirmse, R. A. Stewart, A. E. Wendt, Appl. Phys. Lett. 67 (1995) 3099.

[29] L. Carnel, I. Gordon, K. V. Nieuwenhuysen, D. V. Gestel, G. Beaucarne, J. Poortmans, Thin Solid Films, 487 (2005) 1.

[30] I. Martín, P. Ortega, M. Colina, A. Orpella, G. López, R. Alcubilla., Progress in Photovoltaics: Research and Applications 21 (2013) 1171-1175.

[31] Niyibizi, A., Ikua, B.W., Kioni, P.N., Kihato, P.K. “Laser Material Processing in Crystalline Silicon Photovoltaics”, Proceedings of the 2012 Mechanical Engineering Conference on Sustainable Research and Innovation 4, 69-74 (2012).

[32] Seto, J.Y.W., J. Appl. Phys. 46 (1975) 5247–5254.

[33] H. El Ghitani, M. Pasquinelli, S. Martinuzzi, Journal de Physique III 3 (1993) 1941–1946.

[34] M. Mitani, T. Endo, Y. Taniguchi, T. Katou, S. Shimoto, T. Ohno, S. Tsuboi, T. Okada, K. Azuma, G. Kawachi, M. Matsumura, Jpn. J. Appl. Phys. 47 (2008) 8707.

[35] J. S. Im, H. J. Kim, Appl. Phys. Lett., 64 (1994) 2303–2305.

[36] Y. Helen, R. Dassow, M. Nerding, K. Mourges, F. Raoult, J. R. K¨ohler, T. Mohammed-Brahim, R. Rogel, O. Bonnaud, J. H. Werner, and H. P. Strunk, Thin Solid Films, 383 (2001) 143.

[37] M. Nerding, S. Christiansen, J. Krinke, R. Dassow, J. R. K¨ohler, J. H. Werner, H. P. Strunk, Thin Solid Films, 383 (2001).112.

[38] M. Nerding, R. Dassow, S. Christiansen, J. R. K¨ohler, J. Krinke, J. H. Werner, H.-P. Strunk, J. Appl. Phys., 91 (2002) 4125.

[39] A. Bonfiglietti, A. Valletta, P. Gaucci, L. Mariucci, G. Fortunato, S. D. Brotherton, J. Appl. Phys. 98 (2005) 033702.

[40] S. Varlamov, B. Eggleston, J. Dore, R. Evans, D. Ong, O. Kunz, J. Huang, U. Schubert, K. H. Kim, R. Egan, M. Green, Proc. of SPIE Vol. 8608 86080Q-1.

[41] J. Dore, D. Ong, S. Varlamov, R. Egan, M. A. Green, J. Photovoltaics, 4 (2013) 33-39.

[42] Toet D., Koopmans B., Bergmann R.B., Richards B., Santos P.V., Albrecht M., and Krinke J. Large area polycrystalline silicon thin films grown by laser-induced nucleation and solid phase crystallization. Thin Solid Films, 296 (1997) 49–52.

[43] Toet D., Koopmans B., Santos P.V., Bergmann R.B., and Richards B. Growth of polycrystalline silicon on glass by selective laser-induced nucleation. Applied Physics Letters, 69 (1996) 3719–3721.

[44] Shimokawa R., Ishii K., Nishikawa H., Takahashi T., Hayashi Y., Saito I., Nagamine F., and Igari S. Sub-5 m thin film c-si solar cell and optical confinement by

diffuse reflective-substrate. Solar Energy Materials and Solar Cells, 34(1994) 277–283.

[45] Saboundji A., Mohammed-Brahim T., Andrä G., Bergmann J., and Falk F. Thin film transistors on large single crystalline regions of silicon induced by cw laser crystallization. Journal of Non-Crystalline Solids, 338 (2004) 758–761.

[46] Sameshima T. Laser crystallization for large-area electronics. Applied Physics A: Materials Science and Processing, 96 (2009) 137–144.

[47] T. Frijnts, S. Kühnapfel, S. Ring, O. Gabriel, S. Calnan, J, Haschke, B. Stannowski, B. Rech, R. Schlatmann, Sol. Energ. Mat. Sol. Cells, 143 (2015) 457-466.

[48] E. Leitz, British Patent No. 691355 (1950).

[49] E. I. Givargizov, N. N. Sheftal, V. I. Klykov, Diataxy (graphoepitaxy) and other approaches to oriented crystallization on amorphous substrates, Current Topics in Materials Science 10 (1982) 1–53.

[50] Y. Kawama, A. Takami, H. Naomoto, S. Hamamoto, T. Ishihara, In situ control in zone-melting recrystallization process for formation of high-quality thin film polycrystalline Si, in Proceedings of the 25th IEEE Photovoltaic Specialists Conference (IEEE; New.

[51] C. Hebling, Die kristalline Silicium-D¨unnschichtsolarzelle auf isolierenden Substraten, Ph.D thesis, Universit¨at Konstanz (1998).

[52] S. Reber, W. Zimmermann, T. Kieliba, Zone melting recrystallization of silicon films for crystalline-silicon thin-film solar cells, Solar Energy Materials and Solar Cells, 65 (2001) 409.

[53] T. Ishihara, Zone-melting recrystallization of Si films for solar cells, in Growth, Charecterization and Electronic Applications of Amorphous and Crystalline Si Thin Films; Ralf B. Bergmann (Ed.) (Research Signpost, Kerala) 2002 p. 79–100.

[54] S. Reber, T. Kieliba, S. Bau, “Crystalline Silicon Thin Film Solar Cells on Foreign.

[55] A. Takami, S. Arimoto,H. Naomoto, S. Hamamoto,T. Ishihara,H. Kumabe,T. Murotani, In: Proc. 1st World Conference on Photovoltaic Energy Conversion (1994) 1394.

[56] G. Stollwerck, S. Reber, C. Häßler, Adv. Mater. 13 (2001) 1820.

[57] R. Lüdemann, S. Schaefer, C. Schüle, C. Hebling, In : Proc. 26th IEEE Photovoltaic.

[58] R. Auer, J. Zettner, J. Krinke, G. Polliski, T. Hierl, R. Hezel, M. Schulz, H.-P. Strunk, F.

[59] John C. Evans, Jr., Electron Beam Crystallization of Silicon, Germanium and Cadmium Sulfide, Lewis Research Center Cleveland, Ohio.

[60] S.R. Herd, P. Chaudhari, M.H. Brodsky, J. Non-Cryst. Solids 7 (1972) 309-327.

[61] Porter, D.A. & Easterling, K.E. (1981). Phase Transformations in Metals and Alloys, Chapman & Hall, ISBN: 0412450305, London, Weinheim, New York, Tokyo, Melbourne, Madras.

[62] A. Hiraki, J. Electrochem. Soc. 127 (1980) 2662-2665.

[63] D. Van Gestel, I. Gordon, J. Poortmans, Solar Energy Mat. Solar Cells, 119 (2013) 261-270.

[64] W. Knaepen, C. Detavernier, R.L. Van Meirhaeghe, J. Jordan Sweet, C. Lavoie, Thin Solid Films, 516 (2008) 4946.

[65] O. Nast, S. Brehme, D.H. Neuhaus, S. R. Wenham, IEEE Transactions on Electron Devices 46 (1999) 2062.

[66] M. J. Thompson, R. J. Nemanich, C. C. Tsai, Surf. Sci. 132 (1983) 250.

[67] A. Hiraki, A. Shimizu, M. Iwami, T. Narusawa, S. Komiya, Appl. Phys. Lett. 26 (1975) 57.

[68] A. Hiraki, Semiconductor Technologies, Tokyo, (1982), p.36.

[69] M. Seibt, S. Buschbaum, U. Gnauert, Phys. Rev. Lett. 80 (1998) 774.

[70] A. K. Green and E. Bauer, J. Appl. Phys. 47 (1976) 1284.

[71] L. Hultman, A. Robertsson, H. T. G. Hentzell, I. Engström, P. A. Psaras, Crystallization of amorphous silicon during thin-film gold reaction, J. Appl. Phys. 62 (1987) 3647.

[72] Ö. Tüzün, A. Slaoui, C. Maurice, S. Vallon, Appl. Phys. A 99 (2009) 53–61.

[73] T.L. Alford, P.K. Shetty, N.D. Theodore, N. Tile, D. Adams, J.W. Mayer, Thin Solid Films, 516 (2008) 3940.

[74] Z.X. Zhao, R.Q. Cui, F.Y. Meng, B.C. Zhao, H.C. Yu, Z.B. Zhou, Mater. Lett. 58 (2004) 3963.

[75] J.K. Kim, S.J. Yun, J.W. Lim, S.H. Lee, J. Electrochem. Soc. 158 (2011) 430–434.

[76] O. Nast, T. Puzzer, L. M. Koschier, A.B. Sproul, S.R. Wenham, Appl. Phys. Lett. 73 (1998) 3214.

[77] A. Slaoui, E. Pihan, M. Rusu, Proc. 17th European Photovoltaic Solar Energy Conf. (2001) 1462.

[78] G. Beaucarne, A. Slaoui, "Thin Film Polycrystalline Silicon Solar Cells", In: Thin Film Solar Cells, John Wiley and Sons (2006).

[79] O. Nast, S. Wenham, J. Appl. Phys. 88 (2000) 124.

[80] G. Majni, G. Ottaviani, Appl. Phys. Lett. 31 125 (1977).

[81] G. Ottaviani, G. Majni, J. Appl. Phys. 50 (1979) 6865.

[82] B.Y. Tsaur, G.W. Turner, J.C.C. Fan, Appl. Phys. Lett. 39 (1981) 749.

[83] O. Nast, The aluminium-induced layer exchange forming polycrystalline silicon on glass for thin-film solar cells, Ph.D. Thesis, Philipps-Universität, Marlburg, 2000.

[84] U. Köster, Phys. Stat. Sol. A, 48 (1978) 313.

[85] T. Noma, T. Yonehara, H. Kumomi, Appl. Phys. Lett. 59 (1991) 653.

[86] S. Gall, M. Muske, I. Sieber, O. Nast, W. Fuhs, J. Noncryst. Solids, 741 (2002) 299–302.

[87] K. N. Tu, Appl. Phys. Lett. 27 (1975) 221.

[88] A. Hiraki, Surf. Sci. 168 (1986) 74.

[89] G. Radnoczi, A. Robertsson, H. T. G. Hentzell, S. F. Gong, M. A. Hasan, J. Appl. Phys. 69 (1991) 6394.

[90] J. O. McCaldin, J. Vac. Sci. Technol. 11 (1974) 990.

[91] T. B. Massalski, Binary Alloy Phase Diagrams, 2nd ed. (ASM International, Materials Park, Ohio, 1990).

[92] J.R. Davis, ASM Specialty Handbook: Aluminium and Aluminium Alloys, ASM International, Ohio (1993).

[93] A. D. Pelton, “Thermodynamics and Phase Diagrams of Materials” in Phase Transformations in Materials, edited by P. Haasen(VCH, Weinheim, 1991), Vol. 5.

[94] E. P. Donovan, F. Spaepen, D. Turnbull, J. M. Poate, D. C. Jacobson, Appl. Phys. Lett. 42 (1983) 698.

[95] F. Spaepen, Philos. Mag. 30 (1974).

[96] P. W. Atkins, Physical Chemistry, Oxford University Press, Oxford (1998).

[97] Ö. Tüzün, A. Slaoui, C. Maurice, S. Vallon, Appl. Phys. A, 99 (2010) 53-61.

[98] T. Sontheimer, C. Becker, U. Bloeck, S. Gall, B. Rech, Appl. Phys. Lett. 95 (2009) 101902-101905.

[99] S. H. Sedani, Fabrication and doping of thin crystalline Si films prepared by e-beam evaporation on glass substrate, Msc. Thesis, Middle east Technical University, Ankara (2013).

[100] Refractive index database, Web: www.refractiveindex.info/?shelf=main&book=Si3N4&page=Philipp.

[101] P. Joubert, B. Loisel, Y. Chouan, L. Haji, J. Electrochem. Soc. 134 (1987) 2541-2545.

[102] S. Bourdais, R. Monna, D. Angermeier, A. Slaoui, N. Rauf, A. Laugier, F. Mazel, Y. Jorand, G. Fantozzi, Proc. 2nd World Conference on Photovoltaic Energy Conversion, (1998) 1774.

[103] N. Shakti, P.S. Gupta, Appl. Phys. Res. 2 (2010) 19-28.

[104] Z.X. Zhao, R.Q. Cui, F.Y. Meng, B.C. Zhao, H.C. Yu, Z.B. Zhou, Mater. Lett. 58 (2004) 3963-3966.

[105] Y. Q. Wang, Y. G. Wang, L. Cao, and Z. X. Cao, Appl. Phys. Lett. 83 (2003) 3474-3476.

[106] E. Ibok, M. Santana, S. Garg, Deposition and Optical Properties of UV-Transmissive PECVD Silicon Nitride Films, Proc. Third Symphosium on Silicon Nitride and Silicon Dioxide Thin Insulating Films, 385-394 (1994).

[107] I. Gordon, L. Carnel, D. Van Gestel, G. Beaucarne, J. Poortmans, Prog. Photovolt. Res. Appl. 15 (2007) 575-586.

[108] F.M. Smits, Bell Syst. Tech. J. 37 (1958) 711-718.

[109] L. Börnstein, Numerical Data and Functional Relationships in Science and Technology, Springer, Berlin (1989).

[110] K. Nakajima, N. Usami, Crystal growth of Si for solar cells, Springer Press, Berlin (2009) 193.

[111] J. Klein, J. Schneider, M. Muske, S. Gall, W. Fuhs, Thin Solid Films, 451 (2004) 481–484.

[112] J. Schneider et al. J. Non-Cryst. Solids 338 (2004) 127–130.

[113] M. Stöger-Pollach et al., Thin Solid Films, 515 (2007) 3740 –3744.

[114] O. Nast, A. J. Hartman, J.Appl.Phys. 88 (2000) 716.

[115] J. Schneider et al. J. Non-Cryst. Solids, 352 (2006) 972.

[116] M. Avrami, J. Chem. Phys. 8 (1940) 212.

[117] J. Schneider, A. Sarikov, J. Klein, M. Muske, I. Sieber, T. Quinn, H. S. Reehal, S. Gall, W. Fuhs, J. Cryst. Growth, 287 (2006) 423.

[118] A. Abbadie, J.M. Hartmann, F. Brunier, A review of different and promising defect etching techniques : from Si to Ge, ECS Transactions, 10 (2007) 3-19.

[119] E. Sirtland Adler, Z. Metallk. 52 (1961) 529.

[120] R.W. Maatmanand, A. Kramer, J. Phys. Chem. 72 (1968) 104.

[121] D. G. Schimmel, J. Electrochem. Soc. 126 (1979) 479-483.

[122] E. Stinzianni, K. Dunn, Z. Zhao, M. Rane-Fondacaro, H. Efstathiadis, P. Haldar, Proc. 34th IEEE Photovolatic Specialists Coference, Philadelphia, USA, 001643 (2009).

[123] S. Gall, M. Muske, I. Sieber, J. Schneider, O. Nast, W. Fuhs, in: 29th IEEE Photovoltaic Specialists Conference, New Orleans, USA, 1202 (2002).

[124] J. Y. Wang, Z. M. Wang, E. J. Mittemeijer, J. Appl. Phys. 102 (2007) 113523.

[125] D. Depla, S. Mahieu, Reactive Sputter Deposition, Springer Press, Berlin (2008).

[126] H. Kim, D. Kim, G. Lee, D. Kim, S. H. Lee, Sol. Energy Mater. Sol. Cells 74 (2002) 323.

[127] A. Sarikov, J. Schneider, J. Berghold, M. Muske, I. Sieber, S. Gall, W. Fuhs, J. Appl. Phys. 107 (2010) 114318.

[128] X. Zhai, R. Tan, W. Wang, J. Huang, F. Zhuang, S. Dai, W. Song, J. Cryst. Growth, 402 (2014) 99.

[129] S. Muramatsu, R. Suzuki, L. Wei, S. Tanigawa, Sol. Energy Mat. Sol. Cells 34 (1994) 525.

[130] A. V. Shah, Thin-Film Silicon Solar Cells, EPFL Press, Lausanne (2010).

[131] G. Morell, R. S. Katiyar, S. Z. Weisz, and I. Balberg, J. Non-Cryst. Solids 194 (1996) 78.

[132] G. Morell, R. S. Katiyar, S. Z. Weisz, H. Jia, J. Shinar, I. Balberg, J. Appl. Phys. 78, (1995) 5120.

[133] BINE Information Service, Processing Solar Cells with Laser (2015) http://www.bine.info/fileadmin/content/Publikationen/Projekt-Infos/2015/Projekt_08-2015/ProjektInfo_0815_engl_internetx.pdf.

[134] H. Booth, J. Laser Micro Nanoen. 5 (2010) 3.

[135] M. Weizman, H. Rhein, K. Bhatti, R. Duman, C. Schultz, M. Schle, O. Gabriel, S. Ring, S. Kirner, C. Klimm, M. Nittel, S. Gall, B. Rau, B. Stannowski, R. Schlatmann, F. Fink, Sol. Energy Mater. Sol. Cells, 137 (2015) 280.

[136] G. Poulain, D. Blanc, A. Focsa, B. Bazer-Bachi, M. Gauthier, B. Semmache, Y. Pellegrin, N. Le Quang, M. Lemiti, Int. J. Photoenergy, 2012 (2012) 1-5.

[137] K. Hirata, T. Saitoh, A. Ogane, E. Sugimura,T. Fuyuki, Appl. Phys. Express, 5 (2012) 016501.

[138] J. M. Fairfield, G. H. Schwuttke, Solid-State Electron. 11 (1968)1175.

[139] T. Sameshima, S. Usuzi, M. Sekiya, J. Appl. Phys. 62 (1987) 711.

[140] E. Fogarassy, R. Stuck, J. J. Grob, P. Siffert, J. Appl. Phys. 52 (1981) 1076.

[141] G. Turner et al., Appl. Phys. Lett. 39 (1981) 967 - 969.

[142] D. Kray, A. Fell, S. Hopman, K. Mayer, G. P. Willeke, S. W. Glunz, Appl. Phys. A, 93 (2008) 99 - 105.

[143] U. Besi-Vetrella et al., "Large Area Screen Printed Silicon Solar Cells with Selective Emitter Made by Laser Overdoping and RTA Spin-on Glasses", Twentysixth IEEE PVSC Conf. (1997) 135 - 138.

[144] B.S. Tjahjono, et al., "High Efficiency Solar Cell Structures Through the Use of Laser Doping", Twentysecond EUPVSEC Conf. (2007) 966 - 969.

[145] F. Colville, "Laser-assisted Selective Emitters and the Role of Laser Doping", Technical papers on Cell Processing in the fifth ed. of Photovoltaic International Magazine, (2010) 1-6.

[146] E. Franklin, K. Fong, K. McIntosh, A. Fell, A. Blakers, T. Kho, D. Walter, D. Wang, N. Zin, M. Stocks, E.-C. Wang, N. Grant, Y. Wan, Y. Yang, X. Zhang, Z. Feng and P. J. Verlinden, Prog. Photovolt. Res. Appl. 2016 (2014) 411-427.

[147] S. J. Eisele, T. C. Rder, J. R. Khler and J. H. Werner, Appl. Phys. Lett. 95 (2009) 133501.

[148] H. Plagwitz, M. Nerding, N. Ott, H. P. Strunk. R. Brendel, Prog. Photovolt. Res. Appl. 12 (2004) 47-54.

CURRICULUM VITAE

Mehmet Karaman

Academic Affiliation:	Department of Micro and Nanotechnology Center for Solar Energy Research and Applications (GÜNAM), Middle East Technical University
Date/Place of Birth:	10.09.1984 / Datça-Turkey
Postal Address:	ODTÜ, Fizik Bölümü, B-21, 06800, Ankara-Turkey
Phone:	+90-312-210-5095
E-mail:	mkaramanm@gmail.com

EDUCATION

University	**Subject of Study**	**Degree**	**Country**	**Dates**
Middle East Technical University	Micro and Nanotechnology	Ph.D.	Turkey	2011-2016
Middle East Technical University	Micro and Nanotechnology	M.S.	Turkey	2008-2011
Izmir Institute of Technology	Physics	B.S.	Turkey	2003-2008

WORK EXPERIENCE

Institution	Title	Subject	Dates
The Scientific and Technological Research Council of Turkey, 1003 Project	Project Engineer	Highly Efficient Thin Film Si Solar Cells Produced by Laser Crystallization	18/03/2016-
Helmholtz Zentrum Berlin	Guest Researcher	Laser Crystallized and Laser Doped Silicon Thin Film Solar Cells	01/08/2015-01/12/2015
The Scientific and Technological Research Council of Turkey, 1001 Project	Project Assistant	Aluminium Induced Crystallization of Silicon based solar cells	31/12/2012-31/12/2015
Atılım University, Physics Group	Research Assistant	Lecturer of physics 101 and 102 lab. courses	30/09/2010-31/12/2012
Ministry of Science, Industry and Technology, Thin Film Silicon Solar Cell Project (SAN-TEZ)	Project Assistant	Silicon thin film solar cells	01/03/2008-01/09/2010

AREAS OF EXPERTISE

Nanoscience; Material processing and characterization at micro and nanoscale; Solid state electronic devices; Solar cells; Thin film silicon solar cells; Amorphous silicon deposition and crystallization; Laser Induced Crystallization (LIC); Laser Doping (LD) of silicon thin films; Poly-Si/a-Si Heterojunction Solar Cells on glass; Thin Film Ploy-Si Solar Cells on glass; Solid Phase Crystallization (SPC); Aluminium Induced Crystallization (AIC); Vacuum technology;

RESEARCH EXPERIENCE

Experience in thin-film deposition systems:

Physical vapor deposition (PVD); Electron beam (e-beam) evaporation; Sputtering; Plasma Enhanced Chemical Vapor Deposition (PECVD)

Experience in material characterization techniques:

Conductivity measurements, X-ray diffraction spectroscopy (XRD); Raman spectroscopy, ultraviolet-visible spectroscopy (UV-Vis); Profilometry; Electrical characterization of solar cells, Hall Effect, Current-Voltage analysis; Quantum Efficiency measurement; Solar Simulator.

PUBLICATIONS IN JOURNALS

1. M. Gökçen, Ş. Altındal, **M. Karaman**, U.Aydemir, "Forward and reverse bias current–voltage characteristics of Au/n-Si Schottky barrier diodes with and without SnO2 insulator layer", *Physica B: Condensed Matter*, **406**(21), 4119-4123, (2011).
2. **M. Karaman**, M. Aydın, S. H. Sedani, K. Ertürk, R. Turan, **"**Low temperature crystallization of amorphous silicon by gold nanoparticle" Microelectronic Engineering, **108**: 112-115 (2013)
3. Ö. Tüzün Özmen, **M. Karaman**, R. Turan, "Polysilicon thin films fabricated by solid phase crystallization using reformed crystallization annealing technique", Thin Solid Films, 551: 181-187 (2014)
4. A. Tankut, **M. Karaman**, E. Ozkol, S. Canli and R. Turan, "Structural properties of a-Si films and their effect on aluminum induced crystallization", AIP Advances, **5**, 107114, (2015).
5. A. Tankut, **M. Karaman**, I Yıldız, S. Canlı, R. Turan, "Effect of Al vacuum annealing prior to a-Si deposition on aluminum induced crystallization", Phys. Status Solidi A, **212**, 2702 (2015).

6. **M. Karaman**, Ö. T. Özmen, S. H. Sedani, E. Özkol, R. Turan, Poly-Si thin films formed on glass substrate coated by different buffer layer content, DOI: 10.1002/pssa.201600197

REFEERED CONFERENCE PAPERS

1. Ö. Tüzün, **M. Karaman**, R. Turan, A. Slaoui, Ş. Oktik, “Polysilicon Thin Films Formed by SPC Technique with a Novel Crystallization Process”, 25th European PV Solar Energy Conference and Exhibition (EU PVSEC 2010), September 2010, Valencia
2. **M. Karaman** , Ö. Tüzün, R. Turan, “Structural Analysis and Solar Cells of Polysilicon Films Formed by Solid Phase Crystallization Using Novel Crystallization Annealing” 26th European PV Solar Energy Conference and Exhibition (EU PVSEC 2011) September 2011, Hamburg
3. **M. Karaman**, M. Aydın, K. Ertürk, R. Turan, “Low Temerature Crystallization of Amorphous Silicon by Gold Nanoparticle”, 7th International Conference on Surfaces, Coatings and Nanostructured Materials (NANOSMAT), September 2012, Prague
4. **M. Karaman** , Salar H. Sedani, Ö. Tüzün Özmen, R. Turan, “Aluminium Induced Crystallization of Electron Beam Evaporated Amorphous Silicon for Solar Cell Applications”, International Conference on Nanotechnology, Nanomaterials and Thin Films for Energy Applications (NANOENERGY), February 2014, London (Oral presentation)

5. **M. Karaman** , Ö. Tüzün Özmen, Salar H. Sedani, , R. Turan, “Poly-Si thin films formed on glass substrate coated by different buffer layer” Nanoscience and Nanotechnology conference of Turkey (NanoTr10), June 2014, İstanbul (Oral presentation)

6. **M. Karaman** , Ö. Tüzün Özmen, Salar H. Sedani, , R. Turan, “Formation of n-type and p-type polycrystalline silicon thin films by solid phase epitaxy” Nanoscience and Nanotechnology conference of Turkey (NanoTr10), June 2014, İstanbul (Oral presentation)

7. **M. Karaman**, Ö. Tüzün Özmen, S. Habibpur, R. Turan,“ P-type and N-type Polycrystalline Silicon Thin Films Formed by Aluminium Induced Crystallization and Solid Phase Epitaxy”, International Conference on Computational and Experimental Science and Engineering (ICCESEN 2014), October, Antalya, Turkey, p. 454 (2014)

8. Salar H. Sedani**, M. Karaman** , Ö. Tüzün Özmen, R. Turan, “Effective Parameters in Solid Phase Crystallization Quality & Quantity for a-Si Films Deposited by e-Beam Evaporator”, International Conference on Computational and Experimental Science and Engineering (ICCESEN 2014), October, Antalya, Turkey, p. 559 (2014)
9. Salar H. Sedani**, M. Karaman** , Ö. Tüzün Özmen, R. Turan, “Boron Dopant Effect in Solid Phase Crystallization of a-Si Films Deposited by Effusion Cell Equipped e-Beam Evaporator” International Conference on Computational and Experimental Science and Engineering (ICCESEN 2014), October, Antalya, Turkey, p. 560 (2014)
10. Salar H. Sedani**, M. Karaman** , Ö. Tüzün Özmen, R. Turan, “Thin Film p-type Si Fabrication by e-Beam Evaporation with in-situ Doping on Glass Substrate for Solar Cell Application” Turkish – German Conference on Energy Technologies, 13-15 October, Ankara, Turkey, p. 118 (2014)
11. Salar H. Sedani, M. Kaplan, İ. Yıldız, **M. Karaman,** Ö. Tüzün Özmen, R. Turan, “Accurate Determination of Impurity Contents in Si Thin Films by ToF-SIMS” SIMS Europe 2014, 7-9 September, Münster, Germany, p. 29 (2014)
12. Salar H. Sedani**, M. Karaman** , Ö. Tüzün Özmen, K. Gökşen, R. Turan, “Fabrication & Doping of P-type Si Thin Films Fabricated by E-Beam Evaporation on Glass Substrate” Nanoscience and Nanotechnology conference of Turkey (NanoTr10), June 2014, İstanbul
13. **M. Karaman**, Ö. Tüzün Özmen, S. Habibpur, R. Turan, “P-type and n-type polycrystalline silicon thin films formed by aluminium induced crystallization and solid phase epitaxy” Europian Materials Research Society (EMRS), May 2015 Lille

14. **M. Karaman**, A. Tankut, Ö. Tüzün Özmen, S. Habibpur, R. Turan “A Study of P-type Solid Phase Epitaxial Growth on AIC Poly-Si Seed Layer by e-Beam Evaporation” Europian Materials Research Society (EMRS), May 2015 Lille